

# The synergy between CMB spectral distortions and anisotropies

**Matteo Lucca,<sup>1,2</sup> Nils Schöneberg,<sup>1</sup> Deanna C. Hooper,<sup>1,2</sup> Julien Lesgourgues,<sup>1</sup> Jens Chluba<sup>3</sup>**

<sup>1</sup>Institute for Theoretical Particle Physics and Cosmology (TTK),  
RWTH Aachen University, D-52056 Aachen, Germany.

<sup>2</sup>Service de Physique Théorique,  
Université Libre de Bruxelles, C.P. 225, B-1050 Brussels, Belgium

<sup>3</sup>Jodrell Bank Centre for Astrophysics,  
University of Manchester, Manchester M13 9PL, UK.

E-mail: [matteo.lucca@ulb.be](mailto:matteo.lucca@ulb.be), [schoeneberg@physik.rwth-aachen.de](mailto:schoeneberg@physik.rwth-aachen.de),  
[hooper@physik.rwth-aachen.de](mailto:hooper@physik.rwth-aachen.de)

**Abstract.** Spectral distortions and anisotropies of the CMB provide independent and complementary probes to study energy injection processes in the early universe. Here we discuss the synergy between these observables, and show the promising future of spectral distortion missions to constrain both exotic and non-exotic energy injections. We show that conventional probes such as Big Bang Nucleosynthesis and CMB anisotropies can benefit from and even be surpassed by future spectral distortion experiments. For this, we have implemented a unified framework within the Boltzmann code CLASS to consistently treat the thermal evolution of photons and baryons. Furthermore, we give an extensive and pedagogical introduction into the topic of spectral distortions and energy injections throughout the thermal history of the universe, highlighting some of their unique features and potential as a novel probe for cosmology and particle physics.

---

## Contents

<b>1</b>	<b>Introduction</b>	<b>2</b>
<b>2</b>	<b>Theory</b>	<b>4</b>
2.1	Photon Boltzmann equation	4
2.2	Shapes of the distortions	6
2.3	Amplitudes of the distortions	10
2.4	Causes of the distortions	13
2.4.1	Injection and deposition	13
2.4.2	Energy deposition into heat	14
2.4.3	Heating mechanisms in $\Lambda$ CDM	15
2.4.4	Heating mechanisms in exotic scenarios	23
<b>3</b>	<b>Numerical implementation</b>	<b>26</b>
3.1	Thermal history with energy injection	27
3.2	Spectral distortions from the Green's function approximation	29
3.2.1	General Green's function approach	29
3.2.2	Branching ratios from discretized Green's function	29
3.2.3	The PCA of the residual distortion	30
3.3	Experimental settings and likelihoods	32
<b>4</b>	<b>Results</b>	<b>34</b>
4.1	Running spectral index	35
4.2	Dark matter annihilation	37
4.3	Dark matter decay	37
4.4	Primordial Black Hole evaporation	39
<b>5</b>	<b>Conclusions</b>	<b>41</b>
<b>A</b>	<b>Further details on the photon Boltzmann equation</b>	<b>43</b>
<b>B</b>	<b>Further details on the spectral distortions</b>	<b>44</b>
<b>C</b>	<b>Further details on the heating mechanisms</b>	<b>47</b>
<b>D</b>	<b>Further details on the Green's function approximation</b>	<b>50</b>
<b>E</b>	<b>Further details on the likelihood</b>	<b>51</b>

---

## 1 Introduction

With the recent results of the Planck collaboration [1], the wealth of information gained from cosmic microwave background (CMB) temperature and polarization anisotropies has increased dramatically. Upcoming observations, like for instance the ground-based Simons Observatory [2] and CMB-S4 [3–5] or the space mission LiteBIRD [6, 7], will reach an unprecedented degree of precision.

However, despite their incredible precision, these observations still face limitations. These include cosmic variance on large scales, the diffusion damping for scales  $k \gg 1 \text{ Mpc}^{-1}$ , and the difficulty of accurate astrophysical foreground subtraction [8]. As a consequence, some parameter degeneracies remain, such as between the reionization optical depth  $\tau_{\text{reio}}$  and the amplitude of the primordial power spectrum  $A_s$ . Nonetheless, there is still some information in the CMB that has not yet been exploited to its full potential, and which could help overcome some of the aforementioned limitations. Important examples are the observation of primordial polarization B-modes (e.g., [9–11]), the Bispectrum (e.g., [12, 13]) and higher N-point correlators (e.g., [14]), or observations of CMB secondary anisotropies (e.g., [15]) and lensing effects (e.g., [16–18])

One particularly interesting opportunity to extract more information is given by CMB spectral distortions (SDs) [19–26]. These distortions are created whenever the energy or number density of the CMB photons is modified. Many physical effects that cause deviations from a perfect blackbody (BB) are predicted even within the standard  $\Lambda\text{CDM}$  model, and are linked to a variety of processes spanning from cosmological effects, such as the adiabatic cooling of electrons and baryons, to more particle physics based reactions, as in the case of photon emission and absorption during recombination [26–31]. Even astrophysical models for galaxy and star formation can produce detectable SDs [32] through the Sunyaev-Zeldovich (SZ) effect [33–36].

Furthermore, several non-minimal cosmological models intrinsically predict some level of energy injection. For instance, this is the case in models with dark matter (DM) annihilating or decaying into standard model particles [25, 37–39], DM interacting with baryons or photons [40, 41], Primordial Black Hole (PBH) evaporation [42–46], and different inflationary scenarios [47–52]. All these models can be constrained with future observations of SDs. Additionally, it has been shown that SDs can help us distinguish between different proposed solutions to the so-called *small scale crisis* of cosmology [53, 54].

Moreover, SDs are expected to be anisotropic – analogously to the CMB blackbody temperature and polarization spectra. This has already been measured in the case of Sunyaev-Zeldovich distortions induced by clusters of galaxies [55]. For other sources of SDs, anisotropies are expected to be very difficult to detect. However, a measurement of the power spectrum of SD anisotropies would offer a unique way of investigating the reionization epoch [56–58] as well as the thermal history prior to recombination [59], although the latter signal is even lower.

As such, the amount of information that could be gained from SDs is very rich and would cover times and scales yet unexplored by any other experiment. For a recent review, we refer the reader to [60] and references therein.

Since the pioneering works of the early '70s [19–22, 61], the theoretical framework surrounding SDs has been developed considerably, with significant progress over the last decade. In particular, with the development of COSMOThERM [26] it became possible to precisely compute SD shapes for several physical mechanisms by directly following the full time dependence of the processes involved, which had been approximated in previous numerical studies (e.g., [24, 25]). It then became possible to build approximate solutions based on the Green's function method, which greatly speeds up calculations [26, 62, 63]. A few years later, several efficient schemes have been developed to precisely compute other contributions to SDs like those from non-thermal photon-injection processes [64], the cosmological recombination radiation (CRR) [65, 66], and late-time contributions from reionization and structure formation [67, 68].

Thus, today SD theory relies on a remarkably solid analytical and numerical base. However, the experimental counterpart has unfortunately stayed behind. In fact, the only observation of the energy power spectrum of CMB photons was conducted in the '90s by the COBE/FIRAS satellite at a level of precision such that no SDs were observed [69, 70]. Nevertheless, two important results emerged. First, COBE/FIRAS accurately determined the average CMB temperature [69–71], which fixes the energy scale for understanding the evolution of the pre-recombination, radiation-dominated universe. Second, it set upper bounds on the  $y$  and  $\mu$  parameters describing the final shape of the SDs at approximately  $|y| < 1.5 \times 10^{-5}$  and  $|\mu| < 9 \times 10^{-5}$  (95% confidence level (CL)), which constrains cosmological models with exotic energy release at the level  $\Delta\rho_\gamma/\rho_\gamma < 6 \times 10^{-5}$  (95% CL). Despite their wide-ranging implications, these values are still too loose to touch on the SDs predicted by the  $\Lambda$ CDM model (e.g., [31]). With current technology, significant improvements over the long-standing COBE/FIRAS bounds could be expected, and even the detection of SDs from  $\Lambda$ CDM should be possible [72–74].

In this work we investigate the synergy between CMB anisotropies and SDs, and show the surprising wealth of information to be gained from futuristic experimental setups, covering large ranges of parameter space otherwise unconstrained. To achieve this goal, we first present the implementation of SDs in the Boltzmann code CLASS [75], thus incorporating the already well developed SD formalism in a general cosmological code, in a fully consistent way and without redundant steps. This generalizes and improves on similar studies carried out previously by [39, 76]. We subsequently select a few interesting cosmological scenarios and perform parameter sensitivity forecasts, to illustrate the synergy between future SD missions and other cosmological probes. Our results clearly demonstrate that CMB SDs are an independent and exciting new probe of physics.

This paper is organized as follows. In Section 2 we review the formalism used to describe SDs, paying special attention to the parameter dependency of the SD shape and amplitude, before discussing in Section 2.4 several different mechanisms that can generate SDs. In Sections 3.1 and 3.2 we present the ingredients used for our numerical implementation of SDs in CLASS, while in Section 3.3 we describe the mock likelihoods that we build to account for future experiments. In Section 4 we show how this framework can be used to forecast the sensitivity of parameter reconstruction for different cosmological models, and we illustrate the advantage of combining SDs with other cosmological observables. Our conclusions are presented in Section 5, while the Appendices provide more in-depth details on the SDs formalism.

*Remarks on notation:* Throughout this paper we use Greek indices for four-dimensional quantities (e.g.,  $q^\mu$ ) and adopt the Einstein convention for the summation over repeated indices. The spacetime coordinates and 4-momentum of a particle are denoted by  $q^\mu$  and  $p^\mu$  respectively. Three-dimensional forms will be written in bold. We define the proper momentum measured by comoving observers<sup>1</sup> as  $p = a|\mathbf{p}|$ , which for massless particles in a flat homogeneous FLRW metric implies  $p = p^0 = E$ , where  $E$  is the particle energy measured by the same comoving observers. Furthermore, we use an overdot to indicate derivatives with respect to *physical* time, and – unless stated otherwise – we work in natural units with  $\hbar = c = k_B = 1$ . All these quantities are defined in the context of the homogeneous flat FLRW metric

$$ds^2 = -dt^2 + a^2(t)[dr^2 + r^2d\theta^2 + r^2\sin^2\theta d\phi^2]. \quad (1.1)$$

Moreover, a small  $n$  will correspond to number density, and  $\rho$  to energy density. The symbols  $e, \gamma, b, \nu, \text{cdm}, \text{H}$ , and  $\text{He}$  denote respectively electrons, photons, baryons, neutrinos, cold dark matter, Hydrogen, and Helium. Additionally, we will refer to  $x_e = n_e/n_H$  as the fraction of free electrons.

## 2 Theory

Here we aim to unify and streamline the theory of SDs, building on the theory reviews and lecture notes of [77–79]. In Section 2.1 we introduce the photon Boltzmann equation governing the evolution of the photon phase-space distribution (PPSD). In Section 2.2 we infer what kind of distortions of the BB spectrum of the CMB are allowed. In Section 2.3 we show how the amplitude of the SDs can be calculated for a given thermal history of the universe. Finally, in Section 2.4 we list the most significant heating processes within the standard cosmological model and review several exotic heating mechanisms as well.

### 2.1 Photon Boltzmann equation

The goal of this section is to describe the Boltzmann equation of the PPSD in the presence of Compton scattering (CS), double Compton scattering (DC), and Bremsstrahlung (BR). The study of the evolution of PPSD directly provides a description of SDs, as the observable intensity spectrum is just given by the PPSD multiplied by a factor of  $2h\nu^3/c^2$ .

In the homogeneous FLRW metric we have

$$p^0 \frac{\partial p^\mu}{\partial t} + \Gamma_{\alpha\beta}^\mu p^\alpha p^\beta = 0 \quad \Rightarrow \quad \frac{dp}{dt} = -Hp \quad \Rightarrow \quad p \propto a^{-1}, \quad (2.1)$$

where  $\Gamma_{\alpha\beta}^\mu$  are the Christoffel symbols. For convenience, we define the time-invariant and dimensionless frequency  $x = x(t, p)$ ,

$$x \equiv \frac{p}{T_z} \propto a \cdot p \quad \Rightarrow \quad \frac{dx}{dt} = 0, \quad (2.2)$$

where  $T_0$  is a reference temperature, and  $T_z \equiv T_0(1+z)$  scales exactly as if photons were a decoupled species<sup>2</sup>. The dimensionless frequency is related to the current observed frequency

---

<sup>1</sup>This definition of the proper momentum can be extended in presence of metric fluctuations, but we will only be concerned with homogeneous cosmology within this work.

<sup>2</sup>This quantity should not be confused with the actual photon temperature  $T_\gamma$ , which may have a more complicated evolution. The precise normalization of  $T_z$  is arbitrary, but  $T_0 \equiv T_z(0)$  will be chosen close to the actual temperature today,  $T_\gamma(0) = (2.7255 \pm 0.0005)\text{K}$  [70, 71], in order to have  $T_\gamma \simeq T_z$  at least in the late universe.

$\nu$  through  $x = h\nu/T_0$ . This definition of  $x$  absorbs the momentum redshifting and simplifies the frequency dependence of the BB spectrum, as can be seen in Equations (2.3) and (2.8), respectively.

Furthermore, we are going to assume a homogeneous background-distribution for the PPSD  $f(q^\alpha, p^\alpha)$  such that  $\partial f/\partial \mathbf{q} = 0$  and  $\partial f/\partial \mathbf{n} = 0$  with  $\mathbf{p} = p \mathbf{n}$ . Substituting then  $p(t) \rightarrow x(t, p)$ , we obtain that  $f(q^\alpha, p^\alpha) = f(t, x)$ . Thus, the PPSD obeys the general homogeneous Boltzmann equation

$$C[f] = \frac{df(t, x)}{dt} = \left( \frac{\partial f}{\partial t} \right)_x + \frac{dx}{dt} \left( \frac{\partial f}{\partial x} \right)_t = \left( \frac{\partial f}{\partial t} \right)_x , \quad (2.3)$$

denoting the indices of the brackets as the variables we hold constant when evaluating the derivatives (see Appendix A.1 for more details on our treatment of partial derivatives and a more general discussion regarding Equation (2.3)). This result clearly shows that in absence of collisions, i.e., setting  $C[f] = 0$ , the homogeneous PPSD<sup>3</sup> is constant in time. In other words, only the collision term  $C[f]$  can change the PPSD, as it adds or removes photons or changes the momenta of existing photons.

The main effect capable of modifying the momentum distribution of the photon bath is CS. The solution of the collision term for this process has been found by [80] assuming a Maxwellian electron phase-space distribution. The result is the famous Kompaneets equation

$$C[f]|_{\text{CS}} = \dot{\tau} \frac{T_e}{m_e} \frac{1}{x^2} \frac{\partial}{\partial x} \left( x^4 \left[ \frac{\partial f}{\partial x} + \frac{T_z}{T_e} f(1 + f) \right] \right) , \quad (2.4)$$

where  $\sigma_T$  is the Thomson cross section and  $\dot{\tau} = n_e \sigma_T$ . If CS is very efficient, the system will tend towards an equilibrium solution where  $C[f]|_{\text{CS}}$  is *functionally* identical to zero. This can be fulfilled as long as  $f$  is a solution to the differential equation

$$0 = \left[ \frac{\partial f}{\partial x} + \frac{T_z}{T_e} f(1 + f) \right] , \quad (2.5)$$

which has a physically relevant solution

$$f(x) = \frac{1}{\exp(\tilde{x} + C) - 1} , \quad (2.6)$$

where  $\tilde{x} = x T_z/T_e = p/T_e$  and  $C$  is an integration constant. As expected, this solution coincides with the Bose-Einstein distribution for photons in kinetic equilibrium with electrons with a chemical potential  $\mu = C$ .

CS conserves the number of photons and is compatible with a non-zero chemical potential, but this is not the case for additional processes like DC scattering and BR emission. When those processes are also in equilibrium, the chemical potential must vanish, since reactions like  $n\gamma \longleftrightarrow m\gamma$  with  $n \neq m$  are permitted and efficient (more details are provided in Appendix A.2). As such, the efficiency of the DC and BR processes is crucial to minimize the effective chemical potential of the photon bath, and their inefficiency will subsequently cause a distortion.

---

<sup>3</sup>Note that with perturbations in the PPSD this is not true anymore as shown in e.g., [47–51].

When including these additional processes to the collision term expressed in Equation (2.6), one finds the complete evolution equation for the PPSD, including the most important processes (with  $d\tau = \sigma_T n_e dt$ ):

$$\frac{\partial f}{\partial \tau} = \frac{T_e}{m_e} \frac{1}{x^2} \frac{\partial}{\partial x} \left( x^4 \left[ \frac{\partial f}{\partial x} + \frac{T_z}{T_e} f(1+f) \right] \right) + \frac{K_{\text{BR}} e^{-\tilde{x}}}{\tilde{x}^3} \mathcal{F} + \frac{K_{\text{DC}} e^{-2x}}{x^3} \mathcal{F}, \quad (2.7)$$

with  $\mathcal{F}(x) = 1 - f(x) \cdot (e^{-\tilde{x}} - 1)$ . Here  $K_{\text{BR}}$  and  $K_{\text{DC}}$  are both temperature and frequency dependent factors describing the efficiency of BR and DC, respectively. Note that there are several conventions for the definition of these factors. In particular, the differences between  $\tilde{x}$  and  $x$  can be included in the definitions of  $K_{\text{BR}}$  and  $K_{\text{DC}}$  or not. Here we follow [77], where, together with [26, 81, 82], the interested reader can find the full derivations for these factors and more in-depth discussions.

## 2.2 Shapes of the distortions

The thermalization of the CMB takes place through various processes, the most prominent of which are CS, DC, and BR. As long as all of these processes are efficient, the CMB spectrum will locally remain a BB. Their gradual inefficiency causes the SDs of the BB spectrum to be generated. To model the PPSD  $f(t, x)$  we will thus always decompose it as

$$f(t, x) = B(x) + \Delta f(t, x), \quad (2.8)$$

where  $B(x) \equiv 1/(e^x - 1)$  is the phase-space distribution of a BB at the temperature  $T_z$ . We will treat any contribution to  $\Delta f(t, x)$  as a distortion of the spectrum.

Note that this also includes a deviation of the radiation temperature  $T_\gamma$  from the simple  $T_z \propto (1+z)$  law. In this case, there are no actual distortions with respect to a blackbody spectrum, but only a departure from the arbitrarily chosen reference one. For this reason, we will refer to such deviations as temperature shifts instead of distortions. As argued in the following sections, temperature shifts are very difficult to observe<sup>4</sup>. Consequently, keeping them cleanly separated from the other true distortions will be crucial. As a possible distinguishing criterion to isolate the components of the other distortions, which should not be confused with a shift in temperature, one can use the shift in photon number  $\Delta N$  caused by thermalization. Indeed, this precisely separates the temperature shifts, involving DC, BR and  $\Delta N \neq 0$ , from the other distortions, involving only CS and  $\Delta N = 0$ .

When the PPSD does not follow exactly a thermal shape, several definitions of temperature can be introduced. By choosing the above criterion, we are implicitly introducing a definition of temperature based on number density:  $T_\gamma$  is the temperature of a blackbody that would share the same number density as the distorted PPSD. Other authors occasionally refer to alternative definitions, such as the energy density temperature, or the Rayleigh-Jeans temperature [26, 51]. In any case, our final results will be expressed in terms of the full observable photon energy spectrum, and will thus be independent of the temperature definition.

---

<sup>4</sup>Note that the temperature history  $T_\gamma(z)$  at different times could still be constrained through different probes, such as recombination constraints from CMB anisotropies [83–85] or entropy constraints from BBN [64, 86, 87]. This would, in principle, allow for a measurement of temperature shifts between the corresponding epochs. However, experimental uncertainties are usually much larger than predicted shifts.

All necessary equations and definitions to describe the three major types of distortions expected throughout the thermal history are now assembled. These include, in chronological order of importance, the temperature shift  $g$ , the chemical potential  $\mu$  distortion, and the Compton  $y$  distortion.

### Temperature shift $g$

The solution for the real photon temperature  $T_\gamma$  will deviate from  $T_z$  whenever energy is injected, and from the electron temperature  $T_e$  when their thermal coupling becomes inefficient. Solutions such as Equation (2.6) will then not be applicable. The temperature of the spectrum will be shifted, even if it can still be described as a BB spectrum.

According to Equation (2.8), this can be written at first order as

$$f(x) = B\left(\frac{p}{T_\gamma}\right) = B\left(\frac{x}{1 + \Delta T/T_z}\right) \approx B(x) - x \frac{\partial B(x)}{\partial x} \frac{\Delta T}{T_z} \equiv B(x) + G(x) \frac{\Delta T}{T_z}, \quad (2.9)$$

with  $\Delta T = T_\gamma - T_z \ll T_z$ . Thus, the shift of the phase space distribution reads

$$\Delta f(x) = G(x) \frac{\Delta T}{T_z}, \quad (2.10)$$

where we defined the shape of the temperature shift

$$G(x) = -x \frac{\partial B(x)}{\partial x} = \frac{x e^x}{(e^x - 1)^2}. \quad (2.11)$$

The amplitude of the temperature shift is determined by the true BB temperature today  $T_\gamma(z = 0)$  and the chosen reference temperature  $T_0 \equiv T_z(z = 0)$ . Consequently, it can only be constrained up to the experimental uncertainty on  $T_\gamma(z = 0)$ . In practice, however, it is always possible to readjust the reference temperature to coincide with the observed one.

### Chemical potential $\mu$ distortion

We have seen above that the general solution to the Kompaneets equation in full equilibrium is Equation (2.6), which involves a chemical potential. This chemical potential vanishes only as long as processes changing the number of photons are efficient. Otherwise, one finds<sup>5</sup>

$$f(x) = B(x + \mu) = \frac{1}{e^{x+\mu} - 1} \approx \frac{1}{e^x - 1} - \mu \frac{G(x)}{x} = B(x) - \mu \frac{G(x)}{x}. \quad (2.12)$$

We find that the shift in the total photon phase-space distribution reads

$$\Delta f(x) = -\mu \frac{G(x)}{x}, \quad (2.13)$$

suggesting a *possible* definition of the  $\mu$  distortion shape as

$$\widetilde{M}(x) = -\frac{G(x)}{x}. \quad (2.14)$$

---

<sup>5</sup>To be more rigorous, we should write this solution in terms of  $\tilde{x}$  instead of  $x$ . However, the difference between  $x$  and  $\tilde{x}$  is equivalent to a simple temperature shift distortion, not relevant for this section.

Note, however, that the above PPSD shift does not respect the number count changing criterion employed here to separate the distortions. In fact, the definition expressed in Equation (2.14) can be seen as a superposition of a BB temperature shift and pure  $\mu$  distortion. To correct this, we can subtract the temperature shift away and obtain

$$M(x) = -G(x) \left( \frac{1}{x} - \alpha_\mu \right) , \quad (2.15)$$

where the coefficient  $\alpha_\mu$  is found by imposing that the remaining  $\mu$  distortion conserves the photon number density<sup>6</sup>,

$$\int x^2 M(x) dx \stackrel{!}{=} 0 \quad \Rightarrow \quad \int (-x + \alpha_\mu x^2) G(x) dx = (-G_1 + \alpha_\mu G_2) \stackrel{!}{=} 0 . \quad (2.16)$$

Here we have defined the useful quantity  $G_k = \int x^k G(x) dx = (k+1)! \zeta(k+1)$ , and one subsequently obtains  $\alpha_\mu = G_1/G_2 \approx 0.4561$ . Finally, the  $\mu$  distortion reads

$$\Delta f(x) = \mu M(x) . \quad (2.17)$$

Note that one could have defined  $\mu$  distortions in such way to conserve energy rather number density [51], but the current definition leads to simpler and more consistent formulas.

### Compton $y$ distortion

The  $y$  distortion occurs when the Kompaneets equation (2.4) applies without reaching its equilibrium solution. This occurs when CS still takes place, but is not very efficient. Following any departure from equilibrium, and starting from an initial BB spectrum, the photons will be redistributed on some timescale  $\Delta\tau$  according to<sup>7</sup>

$$\frac{\Delta f}{\Delta\tau} \approx \frac{T_e}{m_e} \frac{1}{x^2} \frac{\partial}{\partial x} \left( x^4 \left[ \frac{\partial B(x)}{\partial x} + \frac{T_z}{T_e} B(x)(1+B(x)) \right] \right) = \frac{T_z - T_e}{m_e} \frac{\frac{\partial}{\partial x}(x^3 G(x))}{x^2} . \quad (2.18)$$

Therefore, the shift in the total photon phase-space distribution reads

$$\Delta f(x) \approx \Delta\tau \frac{T_e - T_z}{m_e} Y(x) , \quad (2.19)$$

which then defines the  $y$  distortion shape as  $\Delta f(x) = y Y(x)$  with

$$Y(x) \equiv -\frac{\frac{\partial}{\partial x}(x^3 G(x))}{x^2} = G(x) \left[ x \frac{e^x + 1}{e^x - 1} - 4 \right] . \quad (2.20)$$

We can immediately see that the photon number density is conserved by such a distortion, since

$$\int x^2 Y(x) dx = - \int \frac{\partial}{\partial x}(x^3 G(x)) dx = 0 , \quad (2.21)$$

and thus there is no need to subtract any additional temperature shift.

---

<sup>6</sup>We recall that the number density is given as  $n(t) = \int f(p, t) d^3 p = 4\pi T_z^3 \int f(x) x^2 dx$

<sup>7</sup>Note that  $-\partial B(x)/\partial x = B(x)(1+B(x)) = G(x)/x$ .

Note that inefficient CS is one possible example of generating a  $y$  distortion, but other processes can cause the same distortion shape of the PPSD. This implies that the general distortion amplitude  $y$  can include additional contributions on top of the historical Compton parameter  $y_C$ , which is commonly defined as

$$y_C = \int \frac{T_e - T_z}{m_e} d\tau = \int \frac{T_e - T_z}{m_e} \sigma_T n_e dt . \quad (2.22)$$

We will come back to the definition of the full amplitude  $y$  and its relation to  $y_C$  in Section 2.3.

### Normalization

For simplicity and consistency, we can normalize the shape distortion functions such that a distortion amplitude equal to one induces a relative variation of the photon energy density of one. For that purpose, we first calculate the factors  $C_x$  such that a distortion amplitude  $g = C_g$ ,  $\mu = C_\mu$  or  $y = C_y$  gives  $\Delta\rho_\gamma/\rho_\gamma = 1$ . For the temperature shift we obtain<sup>8</sup>

$$\frac{\Delta\rho_\gamma}{\rho_\gamma} = C_g \frac{\int x^3 G(x) dx}{\int x^3 B(x) dx} = C_g \frac{G_3}{1/4 G_3} = 4C_g \stackrel{!}{=} 1 \quad \Rightarrow \quad C_g = 1/4 . \quad (2.23)$$

For the  $\mu$  distortion we obtain

$$\frac{\Delta\rho_\gamma}{\rho_\gamma} = C_\mu \frac{\int x^3 M(x) dx}{\int x^3 B(x) dx} = C_\mu \frac{-G_2 + \alpha_\mu G_3}{1/4 G_3} = C_\mu \frac{\kappa_\mu}{3} \stackrel{!}{=} 1 \quad \Rightarrow \quad C_\mu = \frac{3}{\kappa_\mu} , \quad (2.24)$$

with the constants  $\kappa_\mu = 12(G_1/G_2 - G_2/G_3) \approx 2.1419$  and  $C_\mu = 3/\kappa_\mu \approx 1.401$ . Moreover, for the  $y$  distortion we obtain

$$\frac{\Delta\rho_\gamma}{\rho_\gamma} = C_y \frac{\int x^3 Y(x) dx}{\int x^3 B(x) dx} = C_y \frac{G_3}{1/4 G_3} = 4C_y \stackrel{!}{=} 1 \quad \Rightarrow \quad C_y = 1/4 . \quad (2.25)$$

We can then define the renormalized amplitudes as

$$\tilde{y} \equiv y/C_y = 4y , \quad \tilde{\mu} \equiv \mu/C_\mu \approx \mu/1.401 , \quad \tilde{g} \equiv g/C_g = 4g . \quad (2.26)$$

These three renormalized contributions to the shift in the PPSD now have the desired property that  $\tilde{g} = 1$ ,  $\tilde{\mu} = 1$ , or  $\tilde{y} = 1$  result in  $\Delta\rho_\gamma/\rho_\gamma = 1$ .

Finally, the distortions of the intensity spectrum are given by those of the PPSD multiplied by  $2h\nu^3/c^2$ . Using  $x = p/T_z = h\nu/(k_B T_0)$ , we can write this factor as  $2h\nu^3/c^2 = \mathcal{N}x^3$  with  $\mathcal{N} \equiv 2(k_B T_0)^3/(hc)^2$ . Then the intensity spectrum in presence of the three types of distortions reads

$$I(x) = \mathcal{B}(x) + \tilde{g} \mathcal{G}(x) + \tilde{\mu} \mathcal{M}(x) + \tilde{y} \mathcal{Y}(x) , \quad (2.27)$$

where we have defined the normalized shapes

$$\begin{aligned} \mathcal{B}(x) &= \mathcal{N}x^3 B(x) , \\ \mathcal{G}(x) &= C_g \mathcal{N}x^3 G(x) = 1/4 \mathcal{N}x^3 G(x) , \\ \mathcal{M}(x) &= C_\mu \mathcal{N}x^3 M(x) \approx 1.401 \mathcal{N}x^3 G(x) [-1/x + \alpha_\mu] , \\ \mathcal{Y}(x) &= C_y \mathcal{N}x^3 Y(x) = 1/4 \mathcal{N}x^3 G(x) \left[ x \frac{e^x + 1}{e^x - 1} - 4 \right] . \end{aligned} \quad (2.28)$$

---

<sup>8</sup>Remember that  $\rho(t) = \int f(p, t) E d^3 p = 4\pi T_z^4 \int f(x) x^3 dx$ , using  $E = p$  for photons.

## Other distortions

There are several ways to produce distortions that fall in none of the  $g$ ,  $\mu$ , or  $y$  categories (e.g., [26, 62–64]).

In the epochs when the redistribution of the  $y$  distortion towards a chemical potential is neither fully inefficient nor fully efficient, an intermediate (or hybrid) distortion will be obtained. Other types of distortions can also result from highly energetic exotic energy injections when the CS term is very inefficient. The Compton redistribution term is proportional to  $\Delta\tau = \sigma_T n_e \Delta t$ , which can be very small after recombination when the free electron fraction, and correspondingly  $n_e$ , drop towards zero, allowing for the injected photon spectrum to remain “frozen” at the initial injection frequencies [64] (see e.g., [88] for a recent proposal of injections in the Rayleigh-Jeans tail). Other non-thermal distortions can be created by atomic transitions in the pre-recombination era [89, 90] or non-thermal particle distributions [64, 91–95]. All of these particular distortions provide, in principle, additional opportunities for testing the standard cosmological model.

Therefore, general distortions are usually modeled as a sum of  $g$ ,  $\mu$ , and  $y$  distortions plus a residual distortion  $R(x)$ , which has to be calculated knowing the full thermal history. This can be accomplished using, for example, the Green’s function method, as described in Section 3.2. For convenience, we shall also assume the residual distortion to be normalized to  $\Delta\rho_\gamma/\rho_\gamma = 1$ .

### 2.3 Amplitudes of the distortions

According to previous definitions, the total distortion of the photon intensity spectrum is given at first order by

$$\Delta I_{\text{tot}} = \Delta I_y + \Delta I_\mu + \Delta I_T + \Delta I_R , \quad (2.29)$$

where  $\Delta I_y = \tilde{y}\mathcal{Y}(x)$  determines the contribution from  $y$  distortions,  $\Delta I_\mu = \tilde{\mu}\mathcal{M}(x)$  the contribution from  $\mu$  distortions,  $\Delta I_T = \tilde{g}\mathcal{G}(x)$  the contribution from temperature shift  $g$  distortions, and  $\Delta I_R = R(x)\epsilon$  the contribution from residuals, with  $\epsilon$  denoting the energy stored within the residual distortion. For higher precision, the temperature shift can easily be written at second order in  $\tilde{g}$ ,  $\Delta I_T = \tilde{g}(1 + \tilde{g}/4)\mathcal{G}(x) + \tilde{g}^2/8\mathcal{Y}(x)$  (see Appendix B.1 for more details). By means of the decomposition of the  $\Delta I_{\text{tot}}$  into shapes and amplitudes as in Equation (2.29), the full knowledge of the distortion is given by a set of four amplitudes ( $y$ ,  $\mu$ ,  $g$ , and  $\epsilon$ ) and one normalized shape  $R(x)$ .

Our definitions for the normalization factors match those in Ref. [78] and allow to reduce the number of parameters in several equations. In particular, they are such that the relative shift in photon density  $\Delta\rho_\gamma/\rho_\gamma$  is given at first order by the amplitudes  $\tilde{y}$ ,  $\tilde{\mu}$ ,  $\tilde{g}$ , and  $\epsilon$ ,

$$\left. \frac{\Delta\rho_\gamma}{\rho_\gamma} \right|_{\text{tot}} = \left. \frac{\Delta\rho_\gamma}{\rho_\gamma} \right|_y + \left. \frac{\Delta\rho_\gamma}{\rho_\gamma} \right|_\mu + \left. \frac{\Delta\rho_\gamma}{\rho_\gamma} \right|_g + \left. \frac{\Delta\rho_\gamma}{\rho_\gamma} \right|_R = \tilde{y} + \tilde{\mu} + \tilde{g} + \epsilon , \quad (2.30)$$

where the indices  $y$ ,  $\mu$ ,  $g$ , and  $R$  refer to the corresponding fractions of the total injected energy that generate the given distortion.

To calculate each of these amplitudes, we need to know how the PPSD changes throughout the thermal history. The collision operator  $C[f] = C[f(t, x)]$  that appears in the photon

Boltzmann equation of Appendix A.1 accounts precisely for this. To calculate the final spectrum of photons after all injections, one would in principle need to know the full spectral dependence of the injection/collision term [64]. Then the Boltzmann equation would tell us how photon momenta get redistributed or new photons are added, and how the PPSD evolves as a function of the injected spectrum  $C[f]$ .

However, in many interesting cases, the redistribution of photons is quick and efficient enough to erase any dependency of the PPSD on the spectral shape of the injected energy spectrum  $C[f]$ . In this case, what matters is just how much energy is injected in total, and when it is injected [64]. This applies to any injection occurring at dimensionless frequencies  $x < 10^{-4}$ , because the BR and DC processes introduced in Section 2 are very efficient at such frequencies at any point in the history of the universe. The same is true also at high redshifts ( $z > 10^3$ ) and high frequencies ( $x > 10^{-1}$ ), where the redistribution processes of Section 2 are efficient enough to impose a precise shape for the spectrum  $f(t, x)$ , known up to a normalization factor. At each redshift, this precise shape is a combination of the three basic shapes introduced in Section 2.2. We show it for different redshifts on the right panel of Figure 1. Details on this calculations can be found in [64]. In this regime, all that is required to calculate the normalisation factor and infer the PPSD is the frequency-integrated heating rate  $\dot{Q}(z)$ . It is defined as the energy-weighted integral over the collision operator

$$\dot{Q} \equiv \int C[f] E \, d^3 p . \quad (2.31)$$

One can then show (Appendix B.2) that the total energy density injected into photons is related to the heating rate through

$$\frac{\Delta \rho_\gamma}{\rho_\gamma} \Big|_{\text{tot}} = \int_z^\infty \frac{\dot{Q}}{(1+z)H\rho_\gamma} dz . \quad (2.32)$$

The exact approach based on the knowledge of the full photon injection spectra  $C[f]$  could give results slightly different from the simplified approach based on  $\dot{Q}(z)$  at intermediate frequencies and after recombination, because in this regime CS can re-scatter a fraction of the total PPSD (see Equation (30) of [64]). However, the actual frequency dependence of the energy injection term (that should account for the full spectrum of primary and secondary particles which inject energy into the thermal plasma) is currently not well understood, except in a few particular cases. For instance, the case of injections in the Rayleigh-Jeans tail of the CMB spectrum has been investigated in [88].

Luckily, the injection models considered in this work involve frequencies much higher than that of typical CMB photons,  $x \gg 1$ . Thus, energy gets efficiently redistributed at early times. At late times, the effects of reionization are anyway much more significant, and happen in hot clusters where Comptonization is once again efficient. This is why, in this paper as well as in most of the literature, one uses the simplified approach involving only the frequency-integrated heating rate  $\dot{Q}(z)$ . For alternative approaches including the full frequency dependence see [64]. A more exhaustive study including the evolution of the full photon energy spectrum for given injection spectra is left for future work.

Additionally, the assumption of  $\Delta \rho_\gamma / \rho_\gamma \ll 1$  implies that the problem can be linearized [63], and treated with a Green's function approach (see Appendix D.1 for further details).

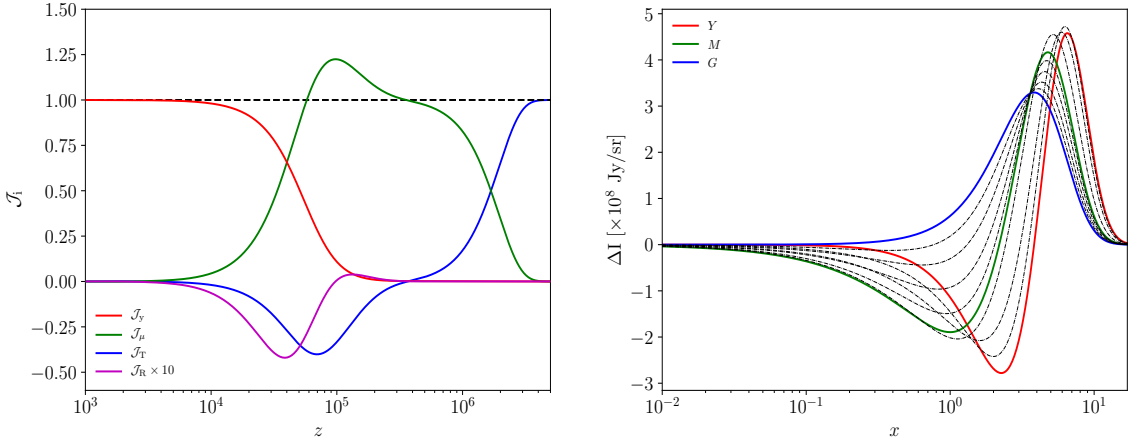


**Figure 1. Left panel:** Branching ratios of the different SD types calculated according to Section 3.2 and defined in Equation (2.33). The red, green, and blue lines correspond respectively to a pure  $y$  distortion,  $\mu$  distortion, and temperature shift. The magenta line refers to the contribution from the residuals. **Right panel:** The corresponding changes in intensity of the photon spectrum given a single *instantaneous* energy injection, plotted for different times of injection. Since the injection is modelled by a  $\delta$ -function in redshift, the Green's functions of Section 3.2 correspond to the total SD. The dashed black lines represent the shapes obtained at redshifts where a mixture of two types of distortions are present. The time of injection is progressing from the blue curve (temperature shift) to the red curve ( $y$  distortion).

During different eras of the thermal evolution of the universe any energy injection will be differently redistributed depending on the availability of number count changing processes and the efficiency of CS. To quantify which part of the injected energy generates each of the distortions, we define for each distortion type  $a$  the branching ratio of deposited energy into the distortion, such that

$$a = \frac{\Delta\rho_\gamma}{\rho_\gamma} \Big|_a \equiv \int \frac{dQ/dz}{\rho_\gamma} \cdot \mathcal{J}_a(z) dz , \quad (2.33)$$

where the branching ratio  $\mathcal{J}_a(z)$  determines the fractional energy release into a given distortion  $a$  as a function of redshift. Here we have used the relation (see Appendix B.2 for additional clarification)

$$\frac{\dot{Q}}{(1+z)H\rho_\gamma} = -\frac{dQ/dz}{\rho_\gamma} \quad (2.34)$$

to recover an expression for the heating rate similar to the one employed in Equation (2.32).

In this way, we have effectively split the problem into the model-dependent heating function  $dQ/dz$  and the model independent branching ratios  $\mathcal{J}_a(z)$ . To find the precise values of the branching ratios, multiple approaches can be taken. Appendix B.3 deals with different common approximations to the branching ratios, and the left panel of Figure 1 displays the results of a quasi-exact calculation based on the Green's function method (see Section 3.2).

The three main eras visible in the left panel of Figure 1 are the  $y$ ,  $\mu$ , and  $g$  eras. For redshifts higher than

$$z_{\text{th}} \equiv 1.98 \times 10^6 \left( \frac{1 - Y_{\text{He}}/2}{0.8767} \right)^{-2/5} \left( \frac{\Omega_b h^2}{0.02225} \right)^{-2/5} \left( \frac{T_0}{2.726 \text{ K}} \right)^{1/5} \approx 2 \cdot 10^6 , \quad (2.35)$$

most of the injected energy tends to fully thermalize as the number count changing processes of DC and BR are very efficient [24, 96]. Hence, mostly temperature shifts will be caused, and the era is named the  $g$  or thermal era. For redshifts between  $z = z_{\mu y} \approx 5 \times 10^4$  and  $z = z_{\text{th}}$ , the number count changing processes become inefficient, while CS is still efficient. This is the so-called  $\mu$  era, during which the dominant contribution will be a  $\mu$  distortion. The final era is the  $y$  era, where CS is inefficient and the injected energy is only partially redistributed, so that a  $y$  distortion is created. This era lasts between  $z = z_{\mu y}$  and today. Finally, the residual distortions  $R(x)$  account for deviations from this simplified picture. The corresponding shapes of the distortions at different times can be seen in the right panel of Figure 1.

## 2.4 Causes of the distortions

As shown in the previous section, the magnitude of the final observed SDs has a complete and unique dependence on the heating history of the universe, which can be parameterized using the heating rate  $\dot{Q}$ . To better understand how to calculate this heating rate, we start with a general discussion regarding the difference between injected and deposited energy in Section 2.4.1, and then focus on energy deposition into heating in Section 2.4.2. Furthermore, in Section 2.4.3 we discuss the different injection mechanisms predicted by the standard  $\Lambda$ CDM model. This catalogue relies on the work of many recent publications like [26, 31, 39]. Finally, in Section 2.4.4 we additionally discuss a few of the most common non-standard injection mechanisms.

### 2.4.1 Injection and deposition

The energy injection into the intergalactic medium (IGM) through various processes does not necessarily immediately heat the IGM and the photon bath. As such, we differentiate energy injection, energy deposition, and various deposition channels. The injected energy is the energy released by a given process. The deposited energy is the fraction of this energy that eventually affects the medium after the radiative transfer and electron cooling. The deposition channels (labelled by an index  $c$ ) describe the final impacts on the IGM.

The deposition *function*  $f_c(z)$  represents the fraction of injected energy that is deposited in channel  $c$  at redshift  $z$ . It can be decomposed into an injection efficiency function  $f_{\text{eff}}(z)$  and a deposition *fraction*  $\chi_c(z)$ , with all deposition fractions across all channels summing up to one,  $\sum_c \chi_c(z) = 1$ . The deposition fraction usually depends only on the free electron fraction  $x_e$  at a given redshift, and can thus be written as  $\chi_c(x_e(z))$ . In summary, the injection and deposition rates are related through

$$\frac{dE}{dtdV} \Big|_{\text{dep},c} = \frac{dE}{dtdV} \Big|_{\text{inj}} f_c = \frac{dE}{dtdV} \Big|_{\text{inj}} f_{\text{eff}} \chi_c \equiv \dot{Q} \chi_c , \quad (2.36)$$

where we have defined the effective rate of energy injection  $\dot{Q}$  as a useful shorthand. It should not be confused with  $\dot{Q}$ , which is the effective heating term (see also Equation (2.37)).

The so-called injection efficiency  $f_{\text{eff}}$  determines how much of the heating is deposited at all, regardless of the form. In general, this function depends on the emitting process and on the characteristics of the universe, such as transparency and energy densities at the time of emission (see for example [97, 98] for recent overviews). For instance, a given process may emit not only particles interacting electromagnetically with the medium, but also neutrinos that do not affect the surrounding environment at all.

Furthermore, the injection efficiency  $f_{\text{eff}}$  does not necessarily coincide with the full fraction of electromagnetically released energy  $f_{\text{em}}$ , as particles emitted at one moment in the history of the universe might lose energy through redshifting or secondary interactions before effectively depositing their energy into the medium. For this reason, we define the fraction of electromagnetic energy lost before the deposition,  $f_{\text{loss}}$ , such that  $f_{\text{eff}} = f_{\text{em}}(1 - f_{\text{loss}})$ . Both  $f_{\text{em}}$  and  $f_{\text{loss}}$  vary in the range from 0 to 1. Note that, although  $f_{\text{loss}}$  might be relevant in the so-called dark ages when the particle density is very low, it is not relevant in high density environments, such as in the pre-recombination plasma, when scatterings are so frequent that particles do not have enough time to lose a significant amount of energy between injection and deposition. Therefore, a common approximation, called *on-the-spot*, assumes the deposition to be instantaneous, and thus sets  $f_{\text{loss}} = 0$ . A detailed calculation of these quantities can be performed with tools like DARKAGES [99] or DARKHISTORY [100].

Next, the deposition fraction  $\chi_c$  partitions the deposited energy into different channels  $c$  depending on their main impact on the thermal bath. For the calculation of SDs we are only interested in the channel corresponding to the heating of the photon bath and intergalactic medium, but for other purposes, like the study of recombination, many other channels play a role. In general, the deposited energy may also ionize hydrogen and helium atoms, or play a role for the excitation of the different transitions of hydrogen (the one with the biggest impact being the Lyman- $\alpha$  transition). Furthermore, some energy could even be lost into photons with too low energies to initiate atomic reactions. Several models with different levels of approximations have been proposed during the last few decades to define how much of the injected energy affects each scenario, and more details on the representative cases [101–103] are given in Appendix C.1. In this paper in all the curves of Section 2.4 and all the analyses of Section 4, we always use the  $\chi_c$  from Table V of [103] (from now on labeled GSVI2013) described further in Appendix C.1.

#### 2.4.2 Energy deposition into heat

When investigating the impact of an energy injection on SDs, the fraction of energy deposited in the form of heat plays a particularly important role. In fact, as already shown in Section 2.3, this quantity is intrinsically linked with the amplitude of the final distortion. In the next few paragraphs we will underline some particular aspects that are important for later discussions.

First of all, it is useful to differentiate between two kinds of heating: the heating of the baryons and the heating of the photons. In both cases, the most general approach to account for the presence of energy injections would be to evaluate their effects on the evolution of the photon/matter temperature  $T_{\gamma/m}$ .

For photons, one can treat any deviation from a BB spectrum with a temperature scaling like the reference temperature  $T_z$  as a distortion. These distortions always remain small, since the injected energy is always much smaller than the total energy of the photon

bath, i.e.  $\Delta\rho_\gamma/\rho_\gamma \ll 1$ . Even when no energy is injected into the IGM and photon bath, distortions can be generated by an internal redistribution among photon momenta, or by energy and momentum exchange between photons and baryons. Examples are provided by the adiabatic cooling of electrons and baryons, and by the dissipation of acoustic waves (see Section 2.4.3 for more details). In that case, equation (2.32) features a contribution to the rate  $\dot{Q}$  despite the fact that there is no actual energy injection: we will call it the non-injected heating rate  $\dot{Q}_{\text{non-inj}}$ . Summing up this contribution with the actual energy injection rate in the form of heat defined in Section 2.3, we can express the effective deposition rate in the form of heat as

$$\dot{Q} = \frac{dE}{dt dV} \Big|_{\text{dep},h} + \dot{Q}_{\text{non-inj}} = \dot{\mathcal{Q}} \chi_h + \dot{Q}_{\text{non-inj}} . \quad (2.37)$$

Note that at early times the *on-the-spot* approximation is valid and the entire injected energy is deposited in the form of heat, as clear from Appendix C.1 and particularly Equation (C.1). For this reason, and since we are primarily interested in the pre-recombination generation of SDs, in the following discussions it will often be possible at early times to employ the approximation  $\dot{Q} \approx \dot{\mathcal{Q}} + \dot{Q}_{\text{non-inj}}$ .

For the baryons, on the other hand, the full temperature evolution is calculated assuming a Maxwellian phase space distribution (see Section 3.1). Due to the very strong and poorly constrained galactic influences, however, the calculation is still very uncertain. Explicitly, we do not even attempt to define or calculate the SDs of the baryon phase space distribution. An improved treatment of the baryon thermal evolution is left for future work.

### 2.4.3 Heating mechanisms in $\Lambda$ CDM

#### Adiabatic cooling of electrons and baryons

If the interaction with the CMB photons can be neglected, the temperature of non-relativistic matter<sup>9</sup> scales as  $T_m \propto (1+z)^2$ , while the photon temperature scales roughly as  $T_\gamma \propto (1+z)$ . At very low redshifts ( $z < 200$ ), when CS becomes inefficient, this difference in the adiabatic index of baryonic matter and radiation leads to a significant difference in the CMB and matter temperatures, with  $T_m < T_\gamma$  [19]. However, at higher redshifts the CMB photons are tightly coupled to baryons. This implies that the baryonic matter in the Universe must continuously extract energy from the CMB in order to establish  $T_m \approx T_\gamma$ . As a consequence of this energy extraction, photons shift towards lower energies [26, 82].

In the steady state approximation [105] the cooling rate associated to this process can be determined as

$$\dot{Q}_{\text{non-inj}} = -H\alpha_h T_\gamma , \quad (2.38)$$

where we define the heat capacity of the intergalactic medium [26, 82, 106] as

$$\alpha_h = \frac{3}{2}n_{\text{bar}} = \frac{3}{2}(n_{\text{H}} + n_e + n_{\text{He}}) = \frac{3}{2}n_{\text{H}}(1 + x_e + f_{\text{He}}) , \quad (2.39)$$

where  $n_{\text{bar}}$  is the number density of all baryonic constituents of the IGM and  $f_{\text{He}} = n_{\text{He}}/n_{\text{H}}$  is the relative abundance of He to H.

<sup>9</sup>Comoving number density conservation gives  $d(a^3 n) = 0$ , and from the first law of thermodynamics one derives  $d(\rho a^3) = -pdV$ . Inserting the expression of  $\rho$  and  $p$  for a non-relativistic species at first order in  $T/m$  gives  $d(na^3 \cdot (m + 3/2T)) = -nTd(a^3)$ . We then find  $na^3 \cdot 3/2dT = -3na^3 T da/a$ , and thus  $dT/T = -1/2 da/a$ , and finally  $T \propto a^{-2} \propto (1+z)^2$  [104].

The evolution of the heating rate expressed in Equation (2.38) can be seen in the left panel of Figure 2 as a blue line. Note that the process described here *extracts* energy from the system, so that the net heating is negative, while in Figure 2 the absolute value is plotted. The same is true for the SDs parameters  $y$  and  $\mu$  resulting from this process<sup>10</sup>, which take the approximate values of  $-5 \times 10^{-10}$  and  $-3 \times 10^{-9}$ . The shape of the corresponding SDs is displayed in the right panel of Figure 2. In fact, as opposed to the case of positive contributions, for adiabatic cooling the low frequency peak is the positive one, whereas the high frequency peak is negative.

### Dissipation of acoustic waves

In the early universe, the presence of primordial density fluctuations causes some regions of space to be hotter and denser than others. At the approach of decoupling, the photon mean free path increases, such that photons diffuse from overdense to underdense regions and vice-versa. This random process leads to an isotropization of the PPSD, and thus to an erasure of density perturbations that is called diffusion damping or Silk damping [107]. This diffusion leads to a superposition of BB spectra with slightly different temperatures which causes SDs [47–49].

The first comprehensive calculation of the consequent heating rate was performed in [51], where the photon Boltzmann equation was calculated at second order in cosmological perturbation theory and second order in the energy transfer by CS. The results in a flat FLRW universe can be summarized in the following heating rate [51, 108]

$$\dot{Q}_{\text{non-inj}} = 4\dot{\tau}\rho_\gamma \int \frac{dkk^2}{2\pi^2} P_{\mathcal{R}}(k) \left[ \frac{(v_\gamma - v_b)^2}{3} + \frac{9}{2}\Theta_2^2 - \frac{1}{2}\Theta_2(\Theta_0^P + \Theta_2^P) + \sum_{\ell \geq 3} (2\ell + 1)\Theta_\ell^2 \right]. \quad (2.40)$$

Here  $P_{\mathcal{R}}(k)$  refers to the primordial power spectrum,  $v_\gamma$  and  $v_b$  are respectively the electron and photon longitudinal velocity.  $\Theta_\ell(k, z)$  is the transfer functions of the  $\ell^{\text{th}}$  photon temperature Legendre multipole moment, related to the Fourier-expanded temperature anisotropy  $\Theta(\mathbf{k}, \hat{n})$  through

$$\Theta(\mathbf{k}, \hat{n}) = \sum_{\ell=0} (-i)^\ell (2\ell + 1) \Theta_\ell(k) P_\ell(\hat{k} \cdot \hat{n}). \quad (2.41)$$

$\Theta_\ell^P(k, z)$  is the transfer functions of the polarization multipole moments, related to the Stokes parameter  $Q(\mathbf{k}, \hat{n})$  in the same way. These transfer functions relate to those of Ma & Bertschinger [109] through  $\Theta_\ell = F_\ell/4$  and  $\Theta_\ell^P = G_\ell/4$ . Additional polarization corrections were originally introduced in [110] and later generalized in [111], but will be omitted here.

To simplify Equation (2.40), as done in [112], we can employ the tight-coupling approximation, i.e.  $v_b \approx v_\gamma$ ,  $\Theta_{\ell \geq 2} \approx 0$ ,  $\Theta_{\ell \geq 0}^P \approx 0$ , and on subhorizon scales  $\Theta_1$  can be inferred from the the approximate WKB solution

$$v_\gamma/3 = \Theta_1 \approx A \frac{c_s^2}{(1+R)^{1/4}} \sin(kr_s) e^{-(k/k_D)^2}. \quad (2.42)$$

---

<sup>10</sup>Although  $\tilde{\mu}$  and  $\tilde{y}$  are used within this work to simplify the equations, for a more direct comparison to previous literature, we quote here the  $\mu$  and  $y$  values.

The normalization of the transfer function  $v_\gamma$  to adiabatic initial conditions with  $\mathcal{R} = 1$  gives

$$A \approx \left(1 + \frac{4}{15} f_\nu\right)^{-1}, \quad (2.43)$$

where  $f_\nu = \rho_\nu/\rho_r$  is the ratio between the energy density of neutrinos and of the total relativistic species (see [54] for a more detailed discussion),  $R = 4\rho_\gamma/(3\rho_b)$  is the ratio between baryon and photon energy density (equal to zero when neglecting baryon loading),  $c_s$  is the sound speed of the fluid,  $r_s(z)$  is the comoving sound horizon, and  $k_D(z)$  is the comoving damping scale. As a result, we can reduce Equation (2.40) to

$$\dot{Q}_{\text{non-inj}} = 8A^2 \rho_\gamma \int \frac{dk k^2}{2\pi^2} P_{\mathcal{R}}(k) \sin^2(kr_s) k^2 (\partial_t k_D^{-2}) e^{-2(k/k_D)^2}. \quad (2.44)$$

For a definition for the damping scale we follow [113], i.e.

$$k_D = \frac{2\pi}{r_D} = 2\pi \left[ \int dz \frac{c_s^2}{2\dot{\tau}H} \left( \frac{R^2}{1+R} + \frac{16}{15} \right) \right]^{-1/2}. \quad (2.45)$$

Note that since the shape of the primordial power spectrum is assumed to be very smooth, one can make use of the average of the quickly oscillating sine over many periods  $\langle \sin^2(kr_s) \rangle = 1/2$ , and hence

$$\dot{Q}_{\text{non-inj}} = 4A^2 \rho_\gamma \int \frac{dk k^2}{2\pi^2} P_{\mathcal{R}}(k) k^2 (\partial_t k_D^{-2}) e^{-2(k/k_D)^2}. \quad (2.46)$$

The evolution of this heating rate is displayed in the left panel of Figure 2 as a red line.

By inserting Equation (2.46) in the definition (2.33), it is possible to show that the  $y$  and  $\mu$  parameters have a value of approximately  $4 \times 10^{-9}$  and  $2 \times 10^{-8}$ , respectively. The corresponding SDs calculated with Equation (2.29) are shown in the right panel of Figure 2 as a red line. We also show there as a horizontal line the expected PIXIE sensitivity, to stress the fact that with the current technological status it would in principle already be possible to observe SDs generated before recombination.

The dependence on the primordial power spectrum allows us to use SDs caused by the dissipation of acoustic waves to constrain the running of the spectral index  $n_{\text{run}}$ , as schematically shown in Figure 2 (dashed red line). Additionally, the dependence of the amplitude  $A$  on the neutrino energy density fraction  $f_\nu$  allows a weak constraint on  $N_{\text{eff}}$  as well, since we can write

$$f_\nu = \frac{\rho_\nu}{\rho_r} = \left(1 + \frac{1}{\alpha(N_{\text{eff}})}\right)^{-1}, \quad (2.47)$$

where  $\alpha(N_{\text{eff}}) = \rho_\nu/\rho_\gamma = (7/8)(4/11)^{1/3} N_{\text{eff}}$ . However, changing  $N_{\text{eff}}$  simply results in an overall change of the heating and SD amplitude, which is degenerate with the amplitude  $A_s$  of the primordial power spectrum  $P_{\mathcal{R}}(k)$ .

By combining with CMB anisotropy constraints, this degeneracy can in principle be broken. However, even with very futuristic SDs measurements, it would be difficult to supersede current  $N_{\text{eff}}$  constraints from Planck [1] or future CMB anisotropy surveys.

Primordial scalar perturbations are not the only source of SDs through dissipation of acoustic waves. Since the effect is at second order in perturbation theory, tensor modes can

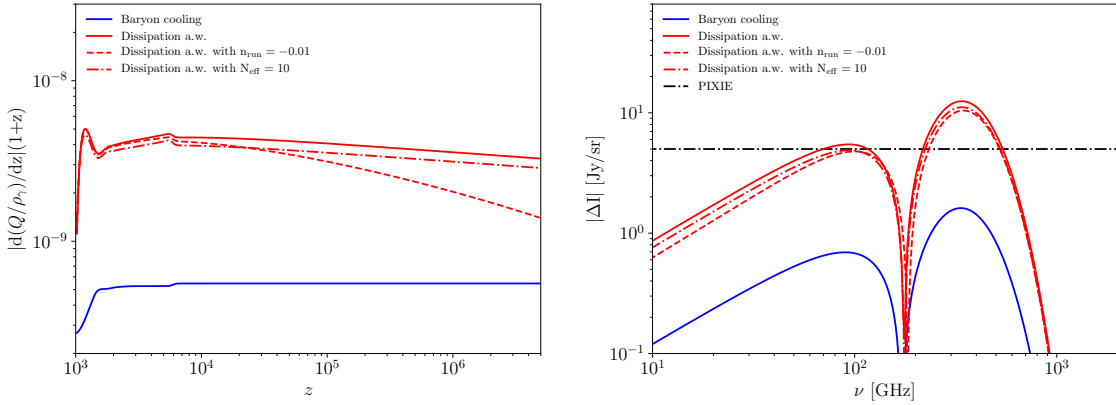


**Figure 2.** Heating rate (left panel) and SDs (right panel) caused by the adiabatic cooling of electrons and baryons (blue line) and by the dissipation of acoustic waves (red line). The difference between the shape of the solid and dashed red lines reflects the influence of the primordial power spectrum on the heating rate. We changed the value of  $n_{\text{run}}$  from 0 to  $-0.01$  as a representative example. Similarly, the difference between the shape of the solid and dashed-dotted red lines reflects the impact of  $N_{\text{eff}}$  on the heating rate, where we increased the value of  $N_{\text{eff}}$  from 3.046 to the extreme value 10. In the right panel, the black dot-dashed line represents the predicted PIXIE sensitivity. Note that the absolute values of each quantity are plotted so that the curve describing the baryon cooling also appears positive, even though the actual contribution is negative.

additionally source it [110, 114]. However, due to the tight constraint of the tensor-to-scalar ratio  $r_{0.002} \lesssim 0.1$  [1, 115], we expect such a contribution to be subdominant, unless the tensor fluctuations are significantly enhanced on scales  $k \ll 0.002 \text{ hMpc}^{-1}$  and do not follow a simple nearly scale-invariant power spectrum. In principle, SDs could be sensitive to tensor fluctuations with wavenumber as large as  $k \simeq 10^7 - 10^8 \text{ Mpc}^{-1}$  [110]. We thus leave a more detailed analysis for future work.

### Cosmological recombination radiation

Another source of SDs is given by the so-called cosmological recombination radiation (CRR) [19, 116, 117] (see [27, 118] for pedagogical reviews, and [66] for the most recent calculations). As the name suggests, this effect is driven by the emission and absorption of photons due to the recombination of H and He, relevant in the redshift intervals  $500 < z < 2000$  for HII→HI,  $1600 < z < 3500$  for the transition HeII→HeI, and  $5000 < z < 8000$  for the transition HeIII→HeII. These processes occur when CS is gradually becoming inefficient, thus resulting in residual distortions on top of  $y$  distortions. These residual distortions are dubbed CRR peaks (see e.g., Figure 1 of [119] for a representative example).

It is interesting to note that, although He makes up only a small fraction of the total matter content, its contribution cannot be overlooked (see e.g., Figure 1 of [120] for a quantitative example). Indeed the role of He is enhanced compared to naive expectations for three reasons. Firstly, there are two epochs of helium recombination. Secondly, HeII recombination occurred when the photon-baryon plasma was still in thermal equilibrium, so that the recombination process followed the Saha solution more closely. Thirdly, the number of photons related to helium atoms is enhanced by detailed radiative transfer effects and feedback processes [121, 122], overall resulting in several emitted photons per helium nucleus from

recombination [121]. As a consequence, the emission lines are more sharply peaked and can thus reach higher amplitudes and change the shape of the broader H lines considerably.

Of course the emission processes strongly depend on the characteristics of the plasma they are taking place in, such as the photon temperature and baryon fraction. Therefore, as discussed for instance in [123], the eventual observation of the CRR peaks would provide an additional and independent test of the parameters describing the standard cosmological model. Furthermore, [90] argues that the influence of possible exotic energy injections might be analyzed through the shape of the CRR spectrum (see, e.g., Figure 5 therein). In contrast to the standard  $y$  distortions, CRR-induced distortions have the additional advantage that their characteristic shape remains unchanged between the end of Hydrogen recombination and today, simplifying thus the extraction of information from an eventual observation [90].

Today it is possible to predict the amplitude of the SDs caused by the CRR extremely precisely, using tools such as COSMOREC [124] and COSMOSPEC [66]. The total contribution to the final distortion is then calculated to be roughly  $\Delta I_{\text{tot}} \approx 0.01 - 1 \text{ Jy/sr}$ . Although CRR is the smallest of the  $\Lambda$ CDM contributions to the  $\Delta I_{\text{tot}}$ , the precision required to observe it might be within reach with futuristic detectors [125, 126].

As a final remark, note that, among all the effects mentioned in Sections 2.4.3 and 2.4.4, this is the only guaranteed contribution to the final distortion shape that is not currently implemented in our code and left as future work.

### CMB multipoles

It is well known [127–129] that the sum of BBs of different temperature is not in itself a BB. One particularly important example of varying temperature is given by the CMB multipoles. For instance, COBE/FIRAS measured a difference of  $3.381 \pm 0.007 \text{ mK}$  between the all-sky average and the dipole temperature. For the dipole, this temperature difference arises from the earth’s movement relative to the CMB rest frame. Under different angles, through the relativistic Doppler effect one observes CMB photons blueshifted (in the direction of motion) or redshifted (opposite to the direction of motion), and thus with different temperatures. Furthermore, even the definition of the all-sky averaged temperature  $T_{\text{ref}}$  will no longer directly correspond to the intrinsic temperature  $T_{\gamma}(z = 0) \approx T_0$ , and induce a temperature shift at second order in  $\Delta T/T_0$  [128].

The angle-dependent temperature of incident photons for an observer moving through the CMB can be calculated through the relativistic Doppler effect to be

$$T(\cos \vartheta) = \frac{T_0}{\gamma[1 - \beta \cos \vartheta]} , \quad (2.48)$$

with the observer’s relativistic velocity  $\beta$ , corresponding Lorentz factor  $\gamma$ , and angle  $\vartheta$  between the Earth’s velocity vector and the line of sight direction.

The corresponding full-sky average temperature  $T_{\text{ref}}$  can be computed as [130]

$$T_{\text{ref}} = \frac{1}{4\pi} \int_0^{2\pi} d\phi \int_0^\pi d\vartheta \sin \vartheta T(\cos \vartheta) = \frac{1}{2} \int_{-1}^1 T(\cos \vartheta) d\cos \vartheta = \frac{T_0}{2\gamma\beta} \ln \left( \frac{1 + \beta}{1 - \beta} \right) . \quad (2.49)$$

As such, for every angle  $\vartheta$  we obtain some deviation of the temperature from the reference temperature, which according to Appendix B.1, gives rise to distortions of the size

$$I(\vartheta) - I_{\text{ref}} = \epsilon(\vartheta)(1 + \epsilon(\vartheta))\mathcal{G}(x) + \epsilon(\vartheta)^2/2\mathcal{Y}(x) , \quad (2.50)$$

where the relative temperature  $\epsilon = \Delta T/T$  is simply given by

$$\epsilon(\vartheta) = \frac{T(\cos \vartheta) - T_{\text{ref}}}{T_{\text{ref}}} . \quad (2.51)$$

At any angle  $\vartheta$  we will thus find a distortion  $I(\vartheta) - I_{\text{ref}}$  due to the peculiar motion of the observer within the CMB rest frame.

However, we might also be interested in the sky-average of the distortion, which can be calculated to be

$$\langle \epsilon \rangle = \frac{1}{4\pi} \int_0^{2\pi} d\phi \int_0^\pi d\vartheta \sin \vartheta \epsilon d\cos \vartheta = 0 , \quad (2.52)$$

$$\langle \epsilon^2 \rangle = \frac{1}{4\pi} \int_0^{2\pi} d\phi \int_0^\pi d\vartheta \sin \vartheta \epsilon^2 d\cos \vartheta = 4\beta^2 \frac{1}{(1 - \beta^2) \ln^2 \left( \frac{1+\beta}{1-\beta} \right)} \approx \beta^2/3 + \mathcal{O}(\beta^4) , \quad (2.53)$$

and thus find that the average distortion is  $\beta^2/3$  for the temperature shift and  $\beta^2/6$  for the  $y$  distortion. Note that the presence of a relative velocity between photons and observer is mainly given by the proper motion of the Solar System with a speed  $\beta = (1.231 \pm 0.003) \times 10^{-3}$  [131]. Therefore, we are left with the sky-averaged  $y_{\text{dipole}} \approx \beta^2/6 \approx (2.525 \pm 0.012) \times 10^{-7}$ . Higher order terms would be of the order of  $10^{-9}$  and are thus ignored for the current analysis.

In a similar way, one can also account for higher CMB multipoles as they also introduce an angle-dependence of the temperature, but detailed studies [128] have shown the effects to be negligible, as the higher multipoles are  $\sim 100$  times smaller than the CMB dipole.

### Reionization and structure formation

Note that the  $y$  parameter determining  $\Delta I_y$  in Equation (2.29) can be decomposed in an early-time and late-time component. Here we discuss the late-time component generated by reionization and structure formation. At these times, due to the inefficiency of CS, the induced distortions are mainly  $y$  distortions.

At this stage of the evolution of the universe the main contribution to SDs is given by the so-called Sunyaev-Zeldovich (SZ) effect [19]. It predicts that when CMB photons travel through a galaxy cluster – or any pocket of electron gas – they might interact with local free electrons. Since the electrons have gained energy due to previous galactic dynamics and gravitational collapse, they are going to be much hotter than the CMB photons. In this way, an inverse CS might occur, which transfers energy to the photons and thereby perturbs the BB distribution.

Two different contributions to the SZ effect are usually distinguished: the so-called thermal SZ (tSZ) effect arises from the interaction of photons and thermally distributed electrons; while the kinematic SZ (kSZ) effect has to be accounted for due to the proper motion of the hosting galaxy cluster in the direction of the observer, additionally boosting the velocity of the electron along the line of sight (LOS). Moreover, besides the effects originating from galaxy clusters, further contributions to the SZ effect can be found more broadly in intracluster and intergalactic media (ICM and IGM). The total SDs created during the reionization epoch can thus be parametrized as

$$\Delta I_{\text{reio}} = \Delta I_{\text{tSZ}} + \Delta I_{\text{kSZ}} . \quad (2.54)$$

Assuming that the electron temperature in the considered clusters does not exceed a few keV, we can expand the tSZ signal in powers of the dimensionless electron temperature  $\theta_e \equiv T_e/m_e$  [132–134]. Since the first order term is a pure  $y$  distortion, and higher order terms account for relativistic corrections, the tSZ signal can be decomposed as

$$\Delta I_{\text{tSZ}} = \tilde{y}\mathcal{Y} + \Delta Y_{\text{rel}} . \quad (2.55)$$

The amplitude of the term linear in  $\theta_e$  is given by  $\tilde{y} \approx 4\Delta\tau\theta_e$ , where  $\Delta\tau$  is the scattering optical depth along the line of sight in the cluster frame. The relativistic correction  $\Delta Y_{\text{rel}}$  becomes relevant for  $\theta_e \gtrsim 10^{-2}$  and induces distortions with a more complicated shape. A possible formulation for  $\Delta Y_{\text{rel}}$  is given in [67] (see also [68, 132–135] for similar discussions). In our implementation we stopped at fourth order in  $\theta_e$ , thus obtaining

$$\Delta Y_{\text{rel}} = \sum_{k=1}^2 \Delta\tau\theta_e^{k+1} Y_k + \mathcal{O}(\theta_e^4) , \quad (2.56)$$

with the  $Y_k$  defined as

$$Y_k = \sum_{n=1}^{2k+2} a_n^{(k)} x^n \partial_x^n \mathcal{B}(x) . \quad (2.57)$$

The numerical coefficients  $a_n^{(k)}$  are found in Table B1 of [67]. Higher order terms can also be found in [67]. Note that this perturbative expansion of the problem in  $\theta_e \ll 1$  does not accurately describe high frequency distortions (for an explicit discussion, see e.g. [67]).

The kinematic SZ contribution depends additionally on the total peculiar velocity of the cluster  $\beta$  (in natural units) and on the angle  $\vartheta$  of its velocity with respect to the LOS. An expansion in the two small parameters  $\theta_e$  and  $\beta$  gives at lowest orders (see Equations (1) and (2a)–(2d) of [68]):

$$\begin{aligned} \Delta I_{\text{kSZ}} = & \mathcal{N} x^3 \Delta\tau \beta \left[ \sum_{k=0}^2 \theta_e^{k+1} (P_0 \beta M_k^{\text{low}} + P_1 D_k^{\text{low}} + P_2 \beta Q_k^{\text{low}}) \right. \\ & \left. + \frac{1}{3} P_0 \beta (Y + G) + P_1 G + \frac{11}{30} P_2 \beta (Y + 4G) \right] \\ & + \mathcal{O}(\theta_e^4, \beta\theta_e^3, \beta^2\theta_e^2) , \end{aligned} \quad (2.58)$$

where  $\mathcal{N} = 2(k_B T_0)^3/(hc)^2$  as before. The Legendre polynomials  $P_n$  are evaluated in  $\cos\vartheta$ , and the distortions  $M_k^{\text{low}}(x)$ ,  $D_k^{\text{low}}(x)$ ,  $Q_k^{\text{low}}(x)$  are defined as in Appendix A of [68]. As seen in Equation (2.58), the contributions from the monopole and quadrupole are suppressed by a factor  $\beta$ , so that the leading order is given by the dipole. Furthermore, as expected from a linearized Lorentz boost [33, 136, 137], the term at first order in  $\beta$  has the shape of a temperature shift  $G(x)$  multiplied by the observer's tangential velocity  $\beta P_1 = \beta \cos\vartheta$  and the optical depth  $\Delta\tau$ , with additional relativistic corrections that are of the order  $\mathcal{O}(\theta_e)$ .

Note that, as pointed out in [67], different conventions for the optical depth  $\Delta\tau$  are present in the literature. This does not affect the expression of the tSZ signal, but it changes the splitting between first order and higher order terms in the expression of the kSZ signal.

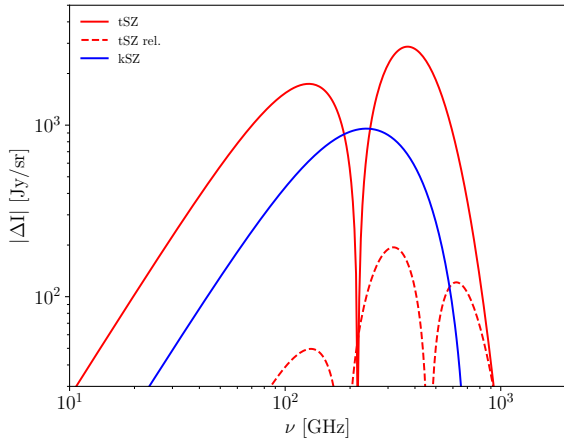


**Figure 3.** SDs caused in the reionization epoch. The solid red curve represents the contribution from the tSZ, which is the dominant one, and the dashed red line shows the relativistic corrections. The blue curve recalls the predicted SDs caused by the kSZ effect.

Thus, for the sake of completeness and generality, in our CLASS implementation we also include the conventions of [138] as an option, where the authors do not define the optical depth in the cluster rest frame.

The observable SZ effect depends on each direction in the sky. In order to compute the average SZ signal, we can use the previous results with some effective average values of the free parameters  $\Delta\tau$ ,  $T_e$ ,  $\beta$  and  $\cos\vartheta$ . For a simple estimate of the average tSZ contribution, we follow [32] and take  $T_e = 4$  keV,  $\theta_e \approx 0.01$ , and  $\Delta\tau = 2 \times 10^{-4}$ , which yields  $y = \tilde{y}/4 \approx 1.6 \times 10^{-6}$ . For the kSZ effect we further fix  $\beta = 0.01$  and  $\vartheta = 0$  as in [67]. These numbers are the default values in our numerical implementation<sup>11</sup>. The resulting SDs are displayed in Figure 3, where the solid red curve represents the leading tSZ contribution, the dashed red line shows the relativistic tSZ corrections, and the blue curve the kSZ contribution. The tSZ effect is the dominant contribution and its maximum is well above the detection threshold of PIXIE-like detectors. The mapping of the thermal and kinematic SZ effects across the sky is a very active field in observational cosmology. In the last decade, several collaborations have been able to infer the matter distribution in the galactic neighborhood from this effect [141–147].

Finally, we should mention the existence of alternative treatments of the contribution to SDs from the reionization era. The authors of [148] based themselves on known solutions of the thermal Comptonization problem in a finite medium [149–151] and studied the effect of the presence of a bounded spherical plasma cloud on the CMB spectrum.

However, accounting for the spatial structure of the medium is only significant if second order contributions in  $\Delta\tau$  are relevant, i.e., if multiple scatterings are possible. However, as

<sup>11</sup>Of course, these numbers are just rough estimates and should be taken with a grain of salt. Several works have discussed the uncertainty on these parameters [67, 68, 138]. For instance, the authors of [32] find the  $y$ -weighted temperature  $T_e = 1.3$  keV and  $\Delta\tau \approx 3.89 \times 10^{-3}$  within the standard SZ halo-model [139], which yields a value  $y = 1.77 \times 10^{-6}$  very similar to that in our baseline model. The average relativistic temperature is indeed dominated by low-mass halos  $\simeq$  few  $\times 10^{13} M_\odot$  rather than those with  $T_e \simeq 5$  keV that contribute most to the power spectrum, see e.g., [140] for a recent discussion.

shown in [152, 153], such second order corrections are negligible, so that we can safely neglect the spatial extension of the medium.

#### 2.4.4 Heating mechanisms in exotic scenarios

In addition to the the heating rates predicted within the standard cosmological model, many other effects can be found that predict different kinds of energy injection or extraction. The most famous and frequently studied ones depend on the presence of annihilating, decaying, or interacting DM, but also Primordial Black Hole (PBH) accretion or evaporation, and early dark energy scenarios that may influence the heating history of the photon bath. In the following paragraphs we are going to describe a few examples.

##### Dark matter annihilation

In the case of annihilating DM, the energy injection rate can be written as

$$\dot{Q} = \rho_{\text{cdm}}^2 f_{\text{frac}} f_{\text{eff}} \frac{\langle \sigma v \rangle}{M_\chi} \equiv \rho_{\text{cdm}}^2 p_{\text{ann}} , \quad (2.59)$$

where  $f_{\text{frac}}$  represents the fraction of annihilating DM with respect to the total DM content,  $\langle \sigma v \rangle$  is the annihilation cross section, and  $M_\chi$  refers to the mass of DM particle. Since the free parameters  $f_{\text{eff}}$ ,  $f_{\text{frac}}$ ,  $\langle \sigma v \rangle$  and  $M_\chi$  are degenerate, they are usually grouped under a single quantity  $p_{\text{ann}}$  called annihilation efficiency (e.g. [1, 103, 154, 155]). The red line in the left panel of Figure 4 shows the evolution of the heating rate  $\chi_h \dot{Q}$  for a given value of  $p_{\text{ann}}$  and assuming maximum deposition efficiency,  $f_{\text{eff}}(z) = 1$  (we recall that we use the GSVI2013 model [103] for the  $\chi_h$ ). The right panel displays the corresponding SD.

Note that Equation (2.59) is true only for the case of s-wave annihilation. If we wanted to consider an annihilating DM with p-wave annihilation cross-section  $\langle \sigma v \rangle \propto (1+z)$  we would have to introduce additional powers of  $(1+z)$  (for more in-depth discussions regarding the origin of this factor see e.g., [39, 156–158]). However, in this case, reference [39] has shown that BBN and light element abundances set much stronger bounds on the annihilation efficiency than SDs. Therefore, we will not discuss this class of models any further.

Another limitation of the model is given by the clustering of DM [155, 159]. In fact, as also argued in [38], at low redshifts the averaged squared DM density  $\langle \rho_{\text{cdm}}^2 \rangle$  is enhanced by a so-called clustering boost factor  $B(z)$ . However, this factor is negligible when investigating SDs, as in our case, and we will not take it into consideration for the following discussions. The factor is, nonetheless, implemented in the code.

Note that assuming a PIXIE detection threshold and all DM annihilating into EM particles only with maximum efficiency, i.e. assuming a constant value of  $f_{\text{eff}}(z) = 1$ , the constraint on  $p_{\text{ann}}$  from SDs would be on the order of  $5 \times 10^{-27} \text{ cm}^3/(\text{s GeV})$ , which is still about one order of magnitude worse than the current constraint given by Planck, which is  $f_{\text{eff}}(z = 600) p_{\text{ann}} < 3.2 \times 10^{-28} \text{ cm}^3/(\text{s GeV})$  at 95% CL [1].

##### Dark matter decay

Another way to transfer energy from the dark sector to photons and baryons is through the decay of unstable dark matter relics. One can assume that some fraction of the DM decays with a given lifetime  $\tau_{\text{dec}}$  and a corresponding decay width  $\Gamma_{\text{dec}} = 1/\tau_{\text{dec}}$ .

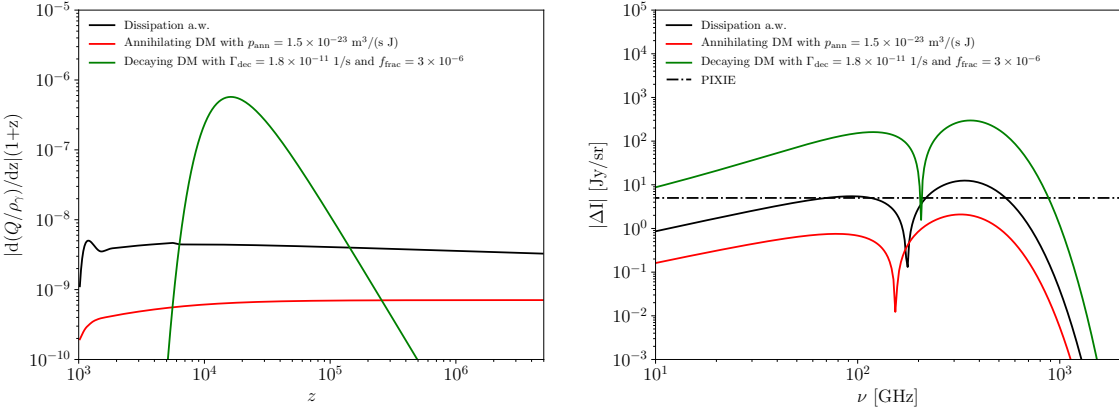


**Figure 4.** Heating rate (left panel) and SDs (right panel) caused by DM annihilation (red line) and decay (green line). The heating rate caused by the dissipation of acoustic waves (black line) is given as a reference. In the right panel the dot-dashed line represents once more the predicted PIXIE sensitivity.

Depending on the value of the lifetime, different approaches can be considered to constrain the parameters of the model. In particular, for lifetimes larger than the time of recombination,  $\tau_{\text{dec}} \geq 10^{13}$  s, CMB anisotropies are by far the most constraining observation (see e.g., [160]). Furthermore, for  $\tau_{\text{dec}}$  in the range from 0.1 s to  $\approx 10^8$  s, deviations from BBN predictions have the largest constraining power [161, 162]. However, for lifetimes in the intermediate range, SDs could be the main source of information [25, 26, 76].

One can define the energy injection rate due to DM decay as

$$\dot{Q} = \rho_{\text{cdm}} f_{\text{frac}} f_{\text{eff}} \Gamma_{\text{dec}} e^{-\Gamma_{\text{dec}} t}. \quad (2.60)$$

Note that once the age of the universe becomes much larger than the lifetime of the particle, the exponential term drives the heating to zero, ceasing to perturb the energy density of the photon bath. The green line in the left panel of Figure 4 shows the heating rate evolution for some arbitrarily chosen values of  $(f_{\text{frac}}, \Gamma_{\text{dec}})$ , assuming again maximum deposition efficiency ( $f_{\text{eff}}(z) = 1$ ). The right panel displays the corresponding SD.

### Evaporation of Primordial Black Holes

In the last few decades PBHs have attracted particular attention as a possible DM candidate (see e.g. [45, 163] for recent reviews, and [99, 160] for further interesting discussions). Furthermore, according to the formation mechanism that is commonly assumed, their mass is tightly connected to the shape of the inflationary potential (see e.g. [163] and the many references listed in Section II therein, as well as [164, 165]). In particular, their abundance is believed to be intrinsically related to a possible non-Gaussianity of the density perturbations [166, 167]. Moreover, it has been argued that a potential detection of a PBH might rule out several WIMP models [168–173].

However, many uncertainties are involved in the modeling of PBHs, especially within the extent to which one can assume mass monochromaticity, the collapsing process at formation time, the presence of Hawking radiation, and the accretion mechanism, if present at all. Many of these open questions could be answered through observing the impact of these different assumptions on the thermal history of the universe.

As a first example, we focus on the evaporation of PBHs. In this case, Hawking radiation [174] is expected to dominate the mass evolution of PBHs according to [42, 43]

$$\frac{dM}{dt} = -5.34 \times 10^{25} \frac{\text{g}}{\text{s}} \times \mathcal{F}(M) M^{-2}, \quad (2.61)$$

where  $M$  is the mass of the PBH, while the function  $\mathcal{F}(M)$  represents the effective number of species emitted by the PBH (the shape and characteristics of this function are further discussed in Appendix C.2). Note also that our current numerical implementation assumes a single initial PBH mass, but would be easy to generalize to extended spectra. In the monochromatic case, and assuming that PBHs account for a fraction  $f_{\text{frac}}$  of DM, the energy injection rate can be calculated as [99, 160]

$$\dot{Q} = \rho_{\text{cdm}} f_{\text{frac}} f_{\text{eff}} \frac{\dot{M}}{M}. \quad (2.62)$$

In the case of PBH evaporation, in contrast to the case of DM annihilation or decay, it is never possible to assume  $f_{\text{eff}} = 1$ , because the spectrum of emitted particles and thus the value of  $f_{\text{em}}$  varies greatly depending on the mass of PBHs at a given time and their related temperature. To calculate  $f_{\text{eff}}$ , we work in the on-the-spot limit  $f_{\text{eff}} = f_{\text{em}}$  (which is a very good approximation at least before recombination and thus for the calculation of SDs). We have devised a new approximation for  $f_{\text{em}}(M)$ , presented in Appendix C.2, which extends the range of validity of a previous scheme introduced in reference [99] towards much lower masses. The evolution of  $\mathcal{F}(M)$  as a function of the PBH mass is displayed in the left panel of Figure 10, while the right panel shows the corresponding  $f_{\text{em}}(M)$ .

Two examples of heating rate evolution are shown in the left panel of Figure 5, with the corresponding predictions for the SDs in the right panel. Evaporating PBHs and decaying DM produce rather similar heating rate evolutions and could be difficult to distinguish through SDs. However, the PBH heating rate is more sharply peaked. This feature would be difficult to probe at the level of  $\mu$  or  $y$  distortions, but leaves a unique signature in the residual distortions. In addition, towards the final stages of the evaporation process, the mean energy of the particles will become very large, such that non-thermal effects are expected to become important. This can be expected to modify the shape of the SDs as well as the heating efficiencies, but we leave both aspects for future analyses.

Finally, we can integrate Equation (2.61) in order to obtain the PBH lifetime. In this way one finds that only PBHs initially lighter than  $10^{13} - 10^{13.5}$  g can evaporate before recombination and thus cause strong SDs, while more massive PBHs can still influence the evolution of photons and baryons through their energy release and leave a detectable signature on the CMB anisotropy spectrum [99].

### Accretion of matter into Primordial Black Holes

PBHs could also influence the thermal history of the universe by accreting matter around them. The accreting matter could heat up, ionize, and consequently radiate high-energy photons. Up to now, no complete numerical simulation of this process over cosmological time scales has been performed. However, several approximate analytical solutions have been found (see e.g., [175–177]). According to these works, one of the biggest sources of uncertainty is the shape of the infalling matter distribution surrounding the PBH.

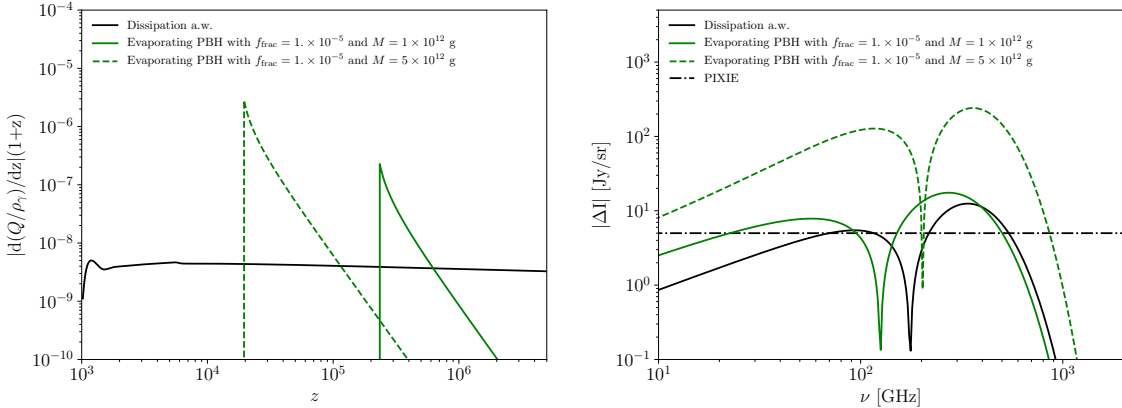


**Figure 5.** Heating rate (left panel) and SDs (right panel) caused by PBH evaporation (green line). The heating rate caused by the dissipation of acoustic waves (black line) is given as a reference. Once more, the dot-dashed line in the right panel represents the predicted PIXIE sensitivity.

Before recombination it is common to approximate the accretion as spherical, which provides a conservative estimate of the luminosity [176]. Furthermore, according to [177], disk accretion becomes a natural option after  $z \approx 10^3$ . However, this is still a source of debate. The two main scenarios, i.e. disk and spherical accretion, could in principle be discriminated through their different impact on the angular power spectra of the CMB (as shown, e.g., in Figure 3 of [177]).

However, SDs are mainly influenced by energy injection before recombination and we conservatively assume spherical accretion up to this point. As argued by [176], this type of PBH accretion does not produce an appreciable level of SDs. Therefore, we will not discuss this case further, although it is implemented within our code for completeness.

### 3 Numerical implementation

In the previous sections we outlined the general picture of how the heating history of the universe could affect the shape of SDs – on top of its signature on CMB anisotropies, well described in the previous literature, see e.g. [92, 97–100, 103, 154, 155, 160, 178], and not reviewed again here. Furthermore, we provided multiple examples of possible effective heating rates  $\dot{Q}$  and summarized their deposition properties. The corresponding numerical computation of the different heating rates, including their related injection efficiency and deposition function, as well as the calculation of the CMB anisotropies and SDs, has been performed with an expanded version of CLASS [75], which will be released as part of CLASS v3.0.

The new version of the code has several differences with respect to previous ones. We are going to discuss in Section 3.1 how we handle the impact of heating rates on the thermal history of the Universe, which is crucial for both calculations of CMB anisotropies (mainly because the ionization fraction  $x_e(z)$  affects the Thomson scattering rate and the photon visibility function) and SDs (since  $x_e(z)$  also affects other quantities described in section 2.4 like the fractions  $\chi_c$ , the diffusion scale  $k_D$  or the heat capacity  $\alpha_h$ ). Then, in Section 3.2, we are going to describe the practical method with which SDs and the corresponding residuals are calculated in our implementation.

As a general remark, it is important to underline the fact that many of the modifications discussed here rely on the work already performed by different groups and previous public codes. First, our implementation of the thermal history in presence of energy injection is based on a previous public branch of CLASS specifically designed for the precise treatment of exotic energy injections, called ExoCLASS [99], which incorporates itself some previous numerical results, in particular from [92].

However, we implemented many improvements with respect to ExoCLASS such as a more consistent implementation of the heating rates with respect to the overall structure of the program, as well as more details discussed in Section 3.1. Second, for the calculation of SDs, we adapted a few parts the public codes COSMOTHERM [26, 63] and SZPACK [67, 68] (see [26, 31, 51, 76] and [32, 138] for related discussions). Also in this case, several improvements have been implemented, regarding in particular the principal component analysis (PCA) expansion and the construction of detector settings discussed in Section 3.2.

Finally, our implementation of likelihoods, which are used to explore the constraining power of current and future SDs measurements, relies on the overall infrastructure of the MONTEPYTHON [179, 180] parameter inference code and is further described in Section 3.3.

### 3.1 Thermal history with energy injection

Before computing CMB anisotropies and/or SDs, any code must compute the evolution of background thermodynamical quantitites like the free electron fraction  $x_e$  or the baryon temperature  $T_m$ . In CLASS this is done by a separate “thermodynamics” module. The recombination equation can be approximated at various levels and can be calculated using three numerical packages: RECFAST [181], HYREC [182], or COSMOREC [124]. The changes describe below are generic and compatible with these three packages.

The presence of at least one of the many heating rates mentioned in Section 2.4 is inevitably going to influence the thermal history of universe. In particular, the fraction of free electrons will change according to

$$\dot{x}_e = I_X + I_s - R_s , \quad (3.1)$$

where  $R_s$  and  $I_s$  correspond to the standard recombination and reionization rates, respectively, and  $I_X$  refers to the contribution from non-standard sources. The presence of this additional factor can be attributed to the fact that effects injecting additional photons into the CMB bath increase the ionization probability of H and He atoms from the ground state, and produce additional Lyman- $\alpha$  photons that boost the  $n = 2$  population.

As a consequence, the rate of photoionization of these excited states by the CMB rises.  $I_X$  can thus be split in the different contributions as

$$I_X = I_{\text{ion}} + I_{X\alpha} , \quad (3.2)$$

where  $I_{\text{ion}}$  and  $I_{X\alpha}$  represent the ionization rate due to ionizing and Lyman- $\alpha$  photons, respectively. These quantities are proportional to the injected energy according to

$$I_{\text{ion}/\alpha} \propto \frac{\dot{Q}\chi_{\text{ion}/\alpha}}{n_H E_{\text{ion}/\alpha}} , \quad (3.3)$$

where  $\chi_{\text{ion}/\alpha}$  represents the deposition fraction into the ionization or Lyman- $\alpha$  channel (these are two of the “ $c$ ” channels already introduced in Section 2.4.1),  $E_{\text{ion}}$  refers to the average ionization energy per baryon, and  $E_\alpha$  is the difference in binding energy between the  $1s$  and  $2p$  energy levels of H (for the precise definitions and a more complete discussion see, e.g., [103]). Note that within the HYREC [182] and COSMOREC [124] codes, the different energy levels of the H atoms are modeled, and thus the precise form of  $I_X$  is in general more complicated than the form expressed in Equation (3.2).

One particular difference to older versions of CLASS is the handling of the recombination coefficients within RECFAST. As argued in [183, 184], these should depend on the radiation temperature rather than the matter temperature. While during most of the cosmic history, this difference is negligible, it is important when strong energy injections affect the ionization history at late times after recombination.

Another quantity that will change depending on the energy injection history is the matter temperature. Its evolution equation can be written as (see e.g., [101, 103, 155], although with different notations)

$$\dot{T}_m = -2HT_m - 2R_\gamma \frac{\mu_b}{m_e} (T_m - T_z) + \frac{\dot{Q}\chi_h}{\alpha_h} , \quad (3.4)$$

where we have used the photon interaction rate  $R_\gamma$  defined as

$$R_\gamma = R\dot{\kappa} = \frac{4}{3} \frac{\rho_\gamma}{\rho_b} n_e \sigma_T , \quad (3.5)$$

which is related to CS, and the mean baryon molecular weight  $\mu_b$  with form

$$\mu_b = \frac{\rho_{\text{bar}}}{n_{\text{bar}}} = \frac{\rho_H + \rho_{He} + \rho_e}{n_H + n_{He} + n_e} \approx m_H \frac{n_H + 4n_{He}}{n_H + n_{He} + n_e} . \quad (3.6)$$

In Equation (3.4), the first term describes the heat loss due to the adiabatic expansion of the universe, the second term refers to the coupling of baryons to photons, and the third term to the heating due to non-standard energy injections. Finally, the function  $\chi_h$  is the deposition fraction into the heating channel, and  $\alpha_h$  is the heat capacity of the IGM defined in equation (2.39).

As a technical remark, note that in the new CLASS implementation, we do not follow the evolution of the matter temperature  $T_m$ , but rather of the difference  $\Delta T_{mz}$  between  $T_m$  and  $T_z$ . The reason for this is that for most part of the evolution of the universe, the two temperatures have extremely similar values, and their difference can be below the level of numerical precision of the differential equation solver (although in our new version of CLASS we now use the advanced differential equation solver `ndf15` [75, 185] even for solving the thermal history). Without such an approach, the photon interaction term  $R_\gamma(T_m - T_z)$  would be dominated by large cancellations between the terms, and thus drastically influenced by the numerical noise. The same procedure is followed in COSMOTHERM [26].

As a final note, the realistic modeling of the matter temperature during reionization is a very challenging task. Since this is not crucial for the applications and analyses discussed in this work, we leave it for future work. Our version of CLASS relies on the same simplistic treatment of  $T_m$  around reionization as previous versions of the code.

## 3.2 Spectral distortions from the Green's function approximation

### 3.2.1 General Green's function approach

As already discussed in Section 2.3, it is possible to write the total SD as

$$\Delta I_{\text{tot}}(x) = \mathcal{G}(x)\tilde{g} + \mathcal{Y}(x)\tilde{y} + \mathcal{M}(x)\tilde{\mu} + R(x, z') , \quad (3.7)$$

excluding second order contributions in  $\tilde{g}$ . In Appendix D.1 we show that the calculation of the total SD can also be performed using a Green's function approach [63]

$$\Delta I_{\text{tot}}(x, z) = \int_z^\infty dz' G_{\text{th}}(x, z') \frac{dQ(z')/dz'}{\rho_\gamma(z')} . \quad (3.8)$$

The Green's function  $G_{\text{th}}(x, z')$  translates an energy injection/extraction at redshift  $z'$  to a distortion of frequency  $x$  observed at the current time. It decouples the cosmology-independent redistribution of photons, and the cosmology-dependent energy injection history. In this way, the knowledge of the heating history of the universe is enough to approximately determine the shape of the SDs.

The Green's function has been computed in [63], using a code that follows the full evolution of the PPSD [26], and computing the response of the plasma to  $\delta$ -like heating terms approximated as narrow Gaussian peaks. The results are contained in a data file published together with the current public version of COSMOTHERM<sup>12</sup>. The same file is employed in our new version of CLASS as well.

However, once the final shape of the Green's function is known, it is interesting to try splitting this function into terms with a straightforward physical interpretation. Using Equation (3.7) and Equation (2.33), one can expand the total Green's function as

$$G_{\text{th}}(x, z') = \mathcal{G}(x)\mathcal{J}_g(z') + \mathcal{Y}(x)\mathcal{J}_y(z') + \mathcal{M}(x)\mathcal{J}_\mu(z') + R(x, z') . \quad (3.9)$$

Several approximations have been used in the past to calculate the required branching ratios  $\mathcal{J}_a(z)$  (see Appendix B.3 for a complete discussion). Recently, [76] has suggested an exact calculation of the branching ratios from the full Green's function, also allowing for the determination of the residual function  $R(x, z)$ . Our implementation follows this method, and performs the calculation steps described below.

### 3.2.2 Branching ratios from discretized Green's function

The approach of [76] is based on least-squares fitting the  $\mathcal{G}(x)$ ,  $\mathcal{Y}(x)$ , and  $\mathcal{M}(x)$  with time-dependent coefficients to the overall  $G_{\text{th}}(x, z)$ . The coefficients are then the branching ratios, while the residuals correspond to the residual distortion. In practice, it is simpler to work directly with quantities that are discretized in frequency space. Then, the least-squares fit can be replaced by Gram-Schmidt orthogonalization. We will denote the discretized version of any quantity  $A(\nu)$  as  $\mathbf{A} = A(\nu_i)$ . We introduce an orthonormal basis of distortion shapes, ordered following the convention of [76] as  $\mathcal{Y}, \mathcal{M}, \mathcal{G}$ <sup>13</sup>.

<sup>12</sup>The full COSMOTHERM is not currently available, and instead the Green's function based approach is found in the GREENS code available at [186].

<sup>13</sup>The ordering does not affect the shape of the residual distortion, but leads to different relative sizes of the  $y$ ,  $\mu$ , and  $g$  distortions. These, however, do not affect the final constraints, as the disambiguation of  $y$  and  $\mu$  distortions is artificial anyway. Furthermore, some choices can lead to numerical problems.

The basis vectors are defined as

$$\mathbf{e}_y = \mathbf{Y}/|\mathbf{Y}|, \quad \mathbf{e}_\mu = \mathbf{M}_\perp/|\mathbf{M}_\perp|, \quad \text{and} \quad \mathbf{e}_g = \mathbf{G}_\perp/|\mathbf{G}_\perp|, \quad (3.10)$$

where the orthogonal components are

$$\mathbf{M}_\perp = \mathbf{M} - \mathcal{M}_y \mathbf{e}_y, \quad \text{and} \quad \mathbf{G}_\perp = \mathbf{G} - \mathcal{G}_y \mathbf{e}_y - \mathcal{G}_\mu \mathbf{e}_\mu, \quad (3.11)$$

with  $\mathcal{M}_y = \mathbf{M} \cdot \mathbf{e}_y$ ,  $\mathcal{G}_y = \mathbf{G} \cdot \mathbf{e}_y$ , and  $\mathcal{G}_\mu = \mathbf{G} \cdot \mathbf{e}_\mu$ . We can then find the branching ratios at any redshift  $z$  by projecting the total Green's function along each basis vector,

$$\mathcal{J}_g(z) = (\mathbf{e}_g \cdot \mathbf{G}_{\text{th}}(z))/|\mathbf{G}_\perp|, \quad (3.12)$$

$$\mathcal{J}_\mu(z) = (\mathbf{e}_\mu \cdot \mathbf{G}_{\text{th}}(z) - \mathcal{G}_\mu \mathcal{J}_g(z))/|\mathbf{M}_\perp|, \quad (3.13)$$

$$\mathcal{J}_y(z) = (\mathbf{e}_y \cdot \mathbf{G}_{\text{th}}(z) - \mathcal{M}_y \mathcal{J}_\mu(z) - \mathcal{G}_y \mathcal{J}_g(z))/|\mathbf{Y}|, \quad (3.14)$$

$$\mathcal{J}_R(z) = 1 - \mathcal{J}_g(z) - \mathcal{J}_y(z) - \mathcal{J}_\mu(z). \quad (3.15)$$

The residual  $\mathbf{R}(z)$  is just given by the difference between the full Green's function and the sum of the  $\mathbf{Y}$ ,  $\mathbf{M}$  and  $\mathbf{G}$  shapes weighted by the branching ratios, such that

$$\mathbf{G}_{\text{th}}(z') = \mathbf{G} J_g(z') + \mathbf{Y} J_y(z') + \mathbf{M} J_\mu(z') + \mathbf{R}(z'). \quad (3.16)$$

The branching ratios resulting from this approach are shown in Figure 1 for the case of the PIXIE detector.

### 3.2.3 The PCA of the residual distortion

While this approach correctly predicts the branching ratios and the residual distortion, it gives no insight on the characteristics and on the physical origin of the the latter. For that purpose, it is beneficial to use a principal component analysis to further decompose the residual distortion into shapes  $\mathbf{S}^{(k)}$  and amplitudes  $\mu^{(k)}$ . As argued in [76], this separation should be performed on the basis of the amount of information that can be extracted by a given experiment from a given shape, which can be quantified through the Fisher information matrix. This approach maximizes the signal to noise ratio of the components  $\mu^{(k)}$  of the residual distortion.

The residual distortion of the final spectrum can be expressed with discrete notations as

$$\Delta I_i^R = \sum_\alpha \hat{R}_{i\alpha} dQ_\alpha, \quad (3.17)$$

where the Latin indices refer to frequencies  $\nu_i$ , and Greek indices to redshifts  $z_\alpha$ . We have defined  $\hat{R}_{i\alpha} = \hat{R}(x_i, z_\alpha) = R(x_i, z_\alpha) \Delta \ln z_\alpha$  and  $dQ_\alpha = dQ(z_\alpha) = [(dQ/d \ln z)/\rho_\gamma]_{z_\alpha}$  to simplify the following equations.

The Fisher-information matrix defines the information content that can be gained by measurements for a given sensitivity  $\delta I_{\text{noise}}(\nu_i)$ , and its principal components define the distortion shapes that have the highest signal to noise ratio for the considered experiment. Assuming diagonal noise covariance, we can calculate it as

$$\mathcal{F}_{\alpha\beta} = \sum_i \frac{1}{\delta I_{\text{noise}}(\nu_i)^2} \frac{\partial \Delta I_i^R}{\partial dQ_\alpha} \frac{\partial \Delta I_i^R}{\partial dQ_\beta} = \sum_i \frac{\hat{R}_{i\alpha} \hat{R}_{i\beta}}{\delta I_{\text{noise}}(\nu_i)^2}. \quad (3.18)$$

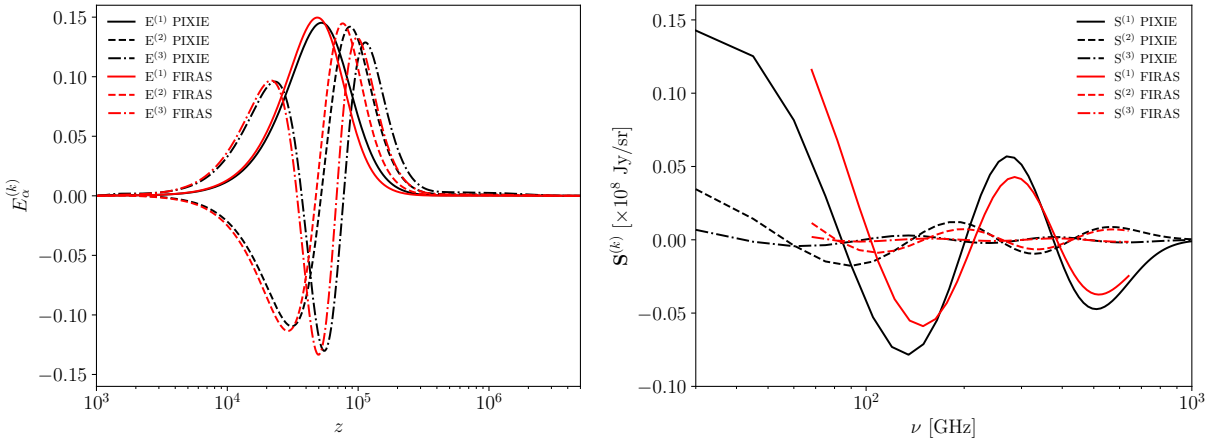


**Figure 6.** Eigenvectors  $E_\alpha^{(k)}$  of the Fisher matrix (left panel) and corresponding SD signal  $\mathbf{S}^{(k)}$  (right panel) for PIXIE (black lines) and FIRAS (red lines) detector specifics. Note that in the right panel the minimum and maximum frequencies are detector dependent, as discussed in Section 3.3.

The orthonormal eigenvectors  $E_\alpha^{(k)}$  of this symmetric matrix allow for the computation of the optimal amplitudes and shapes

$$\mu_k = \sum_\alpha E_\alpha^{(k)} dQ_\alpha , \quad \mathbf{S}^{(k)} = \sum_\alpha E_\alpha^{(k)} \hat{\mathbf{R}}_\alpha . \quad (3.19)$$

where  $\mu^{(k)}$  is the amplitude (in the sense of Equation (2.33)) and  $\mathbf{S}^{(k)}$  is the distortion signal of the  $k^{th}$  eigenmode. Consequently, this allows us to decompose the residual distortions as

$$\Delta \mathbf{I}^R \approx \sum_k \mu^{(k)} \mathbf{S}^{(k)} . \quad (3.20)$$

The result of this PCA is displayed in Figure 6 for the case of PIXIE (black line) and FIRAS (red line).

Using a similar approach, one can also obtain the residual parameter  $\epsilon$  introduced in Equation (2.30) from

$$\epsilon \approx \sum_k C_S^{(k)} \mu_k , \quad (3.21)$$

where  $C_S^{(k)} = \sum_i S^{(k)}(x_i) \Delta x_i / \sum_i \mathcal{G}(x_i) \Delta x_i$  is normalized in the same way as other contributions, see Equations (2.23)-(2.25)<sup>14</sup>.

We want to underline that our CLASS implementation automatically generates the orthogonal branching ratios and the PCA of the residual distortions. For this, it needs a binned frequency array together with a corresponding sensitivity, as in the case of FIRAS, or a minimal set of free parameters  $\{\nu_{\min}, \nu_{\max}, \Delta\nu_c, \delta I_{\text{noise}}\}$ , as in the case of PIXIE. For the latter case, the noise is assumed to be frequency independent (i.e.  $\delta I_{\text{noise}}(\nu_i) = \delta I_{\text{noise}}$ ), and the binning to be of equal width  $\Delta\nu_c$  between  $[\nu_{\min}, \nu_{\max}]$ .

<sup>14</sup>Note that the ratio simplifies to  $\sum_i S^{(k)}(x_i) / \sum_i \mathcal{G}(x_i)$  as in [76] only if the grid is equally spaced.

### 3.3 Experimental settings and likelihoods

In the previous sections we described how, for a chosen cosmological model, we can accurately predict the total SDs parameterized as in Equation (3.7). Furthermore, we also saw how different experimental configurations of possible SD missions can be used to determine the shape of the branching ratios through a PCA analysis, and thus the observed SDs. We are now interested in seeing how well different cosmological scenarios can be constrained, given current and future SDs experiments. Thus, we want to address the question: *Assuming an experiment has measured a total SD  $\Delta I_{\text{tot}}$ , which cosmological parameters can we constrain?*

With this in mind, we have added a new family of likelihoods to the parameter extraction code MONTEPYTHON [179, 180] to deal with *any* SD mission, making use of the MCMC forecast method detailed in [187]: a future (or current) experiment is encoded as a mock likelihood, providing the probability that the generated mock data is true given the model assumed at each step of the MCMC parameter exploration. In more detail, for our likelihood

1. We choose a fiducial model (for example  $\Lambda$ CDM with cosmological parameters as measured by Planck [1]).
2. For this model, we use CLASS to compute the total SDs in each frequency bin of the experiment. This is stored as our *observed* SD.
3. For each step in the MCMC, we update the cosmological parameters of our model, and use CLASS to compute the *predicted* total SDs in each frequency bin of the experiment for this model.
4. For each step a new  $\chi^2$  is computed by comparing the *predicted* model with the *observed* one, taking into consideration the sensitivity of the experiment to the signal,

$$\chi^2 = \sum_{\nu_i} \left( \frac{\Delta I_{\text{predicted}}(\nu_i) - \Delta I_{\text{observed}}(\nu_i)}{\delta I_{\text{noise}}(\nu_i)} \right)^2, \quad (3.22)$$

where we have assumed the noise in different bins  $i$  to be uncorrelated.

With this family of likelihoods, in order to define a new detector, we simply need to provide the code with either the free parameters  $\{\nu_{\text{min}}, \nu_{\text{max}}, \Delta\nu_c, \delta I_{\text{noise}}\}$  (assuming constant noise and equal binning), or the full binned frequency array  $\nu_i$  together with the corresponding sensitivities  $\delta I_{\text{noise}}(\nu_i)$ .

Our method to compute the distortions assumes that temperature shifts vanish at the earliest time (or maximal redshift  $z_{\text{max}}$ ) included in the integral of Equation (2.33). This is implicitly equivalent to a normalization of the reference temperature  $T_0$  such that  $T_z = T_0(1+z)$  coincides with the true  $T_\gamma(z)$  at  $z = z_{\text{max}}$ . In reality, the measurement of  $T_\gamma(0)$  by experiments like FIRAS aims at minimizing temperature shifts, which is equivalent to fixing  $T_0 = T_\gamma(0)$  (up to an experimental error). Thus, in our mock likelihood, we do not need to take into account the value of  $g$  coming from Equation (2.33): we can simply fix  $g$  to zero. However, to be consistent, we must still take into account the experimental uncertainty on  $T_\gamma(0)$ . For this purpose, we marginalize over a temperature shift distortion to second order, i.e., we marginalize over the parameter  $\Delta_T$  which affects the final spectrum as

$$\Delta I_{\text{marg}}(x) = \Delta_T(1 + \Delta_T)\mathcal{G}(x) + \Delta_T^2/2\mathcal{Y}(x). \quad (3.23)$$

For the nuisance parameter  $\Delta_T$ , we choose a Gaussian prior with a standard deviation matching the current experimental resolution of the CMB BB temperature, which has a relative uncertainty of about  $\sigma(T_\gamma(0))/T_\gamma(0) = 0.00022$  [70, 71]. Since experiments like PIXIE or PRISM are designed for a differential measurement of the CMB frequency spectrum, it is not clear that they will significantly reduce this error. To be conservative, we keep the same  $\sigma(T_\gamma(0))$  even in our PIXIE and PRISM mock likelihoods. Together with the set of experimental errors  $\delta I_{\text{noise}}(\nu_i)$ , this marginalization over  $\Delta_T$  contributes to the final uncertainty on the extracted  $y$  distortions. Note that the typical temperature shift coming from Equation (2.33) is of order  $10^{-8} - 10^{-9}$ , thus several orders of magnitude smaller than  $\sigma(T_\gamma(0))$ . Therefore, in practice, setting  $g = 0$  in the likelihood or keeping the value inferred from Equation (2.33) makes no difference.

Similarly to what was done in [76], we could also single out the contributions from reionization, and marginalize over the corresponding  $y$  parameter as well as the galaxy-dependent quantities described in Section 2.4.3. However, here we assume that every contribution from the epoch of reionization can be modeled and calculated with better precision than present and future measurement errors, and subtracted from the data. As a consequence, we set it to zero in the fiducial and fitted models, and we do not marginalize over  $y_{\text{reio}}$ . Note that neglecting all late time effects (such as the SZ effect) is an optimistic approximation since in reality, uncertainties in the modeling of reionization could leave residuals at the level of  $\delta y \approx 10^{-8} - 10^{-7}$ .

With this framework we have developed likelihoods for three detectors: the existing FIRAS [70], and the proposed future missions PIXIE [72] and PRISM [188]. For the latter two we assume idealized scenarios, in which the foreground removal is almost optimal within a certain range of frequencies. This frequency range is discussed and motivated in [30, 125]. A more realistic treatment of the foregrounds, as in [189], is left for future work. Such a treatment could degrade the sensitivity to  $\mu$  distortions in particular, due to degeneracies with low-frequency foregrounds [189]. However, modifications of future instruments and combination with external datasets can improve the foreground-removal capabilities [73]. Thus our estimates provide at least a useful benchmark.

For FIRAS we have used the binned frequency array provided in Table 4 of [70]. For PIXIE we have made the same assumptions as in [39, 76], which are based on the more extensive calculation conducted in [72]: we have assumed equidistant, independent frequency channels in the range [30 GHz – 1 THz], with a bin width of  $\Delta\nu = 15$  GHz. Furthermore, we have assumed that the measurement is only limited by uncorrelated instrumental noise, and all foregrounds can be removed with higher frequency channels. This gives us an overall constant noise of  $\delta I_{\text{noise}}(\nu_i) \approx 5 \times 10^{-26} \text{ W m}^2 \text{ s}^{-1} \text{ Hz}^{-1} \text{ sr}^{-1}$  for each frequency bin (see Appendix E.1 for a detailed calculation). Finally, for PRISM we assumed the same frequency channel characteristics as PIXIE, but with a sensitivity improved by one order of magnitude, i.e.  $\delta I_{\text{noise}}(\nu_i) \approx 5 \times 10^{-27} \text{ W m}^2 \text{ s}^{-1} \text{ Hz}^{-1} \text{ sr}^{-1}$ . This choice is compatible with (although slightly more optimistic than) the forecasted PRISM performance proposed in Table 2 of [188].

The detector FIRAS has a corresponding sensitivity to the  $\mu$  parameter of  $\delta\mu = 3 \times 10^{-5}$ , PIXIE of  $\delta\mu = 9 \times 10^{-9}$ , and PRISM of  $\delta\mu = 9 \times 10^{-10}$  (at  $2\sigma$  level). These levels of precision are optimistic compared to those found respectively in references [70, 72, 188], as we do not marginalize over the  $y$ -contribution from reionization. It is thus more instructive to compare

these sensitivities to the  $\mu$  distortion parameter, since the spectral sensitivity  $\delta I_{\text{noise}}(\nu)$  is usually affected significantly by the precise design of an experiment and the final difficulty of foreground subtraction. The given bounds for the  $\mu$  parameter identify the detector sensitivity in a less experiment-dependent way. Any other experiment with a similar bound on  $\mu$  can still expect similar exclusion regions, even if their  $\delta I_{\text{noise}}(\nu)$  is not the same.

The fact that our code can accept arbitrary experimental setups as an input has a crucial advantage: it allows to analyze the influence of different choices for the frequency array (see the difference between FIRAS and PIXIE), which may affect the ability to disambiguate  $\mu$  and  $y$  distortions, as well as the role of the sensitivity (see the difference between PIXIE and PRISM), which determines the overall constraining power. This method can also be applied to optimize the characteristics of a planned SD mission for a given physics-motivated target.

## 4 Results

In the following section we are going to apply the theoretical framework described in Section 2 to different cosmological models, using the numerical implementation defined in Section 3. In particular, the main goal is to show many different aspects of the synergy between CMB SDs and anisotropies, extending and complementing the analysis of [39, 76].

As a first application of our setup, in Section 4.1 we will explore the constraining power provided by the combination of SDs and CMB anisotropies on a minimal extension of the  $\Lambda$ CDM model with a running of the spectral index of the primordial power spectrum,  $n_{\text{run}}$ . Then, in Sections 4.2, 4.3, and 4.4, we will consider extensions of  $\Lambda$ CDM which include exotic energy injection mechanisms like DM annihilation, DM decay, and the evaporation of PBHs respectively. For each of these models we will single out the role of new physical parameters and investigate how strongly the constraints are affected by the inclusion of SD.

To cover a large spectrum of physical effects and detector sensitivities, we will base our analysis on completed missions like Planck [85] and FIRAS [70], which we will then compare to future experiments or proposed projects with improved characteristics such as Lite-BIRD [6, 7], CMB-S4 [3–5], PIXIE [72], and PRISM [188] (considered both separately and/or in combination with one another). For all these experiments, we employ mock likelihoods<sup>15</sup>, making use of the method described in Section 3.3, and following the prescriptions of [190].

For all following examples, the fiducial models mentioned in Section 3.3 for all likelihoods have been created assuming  $\Lambda$ CDM, with the parameter basis  $\{h, \omega_b, \omega_{\text{cdm}}, n_s, A_s, z_{\text{reio}}\}$  and fiducial values close to the Planck 2018 best-fit values [1].

For the particular case of the SD likelihoods, on top of exotic energy injection rates from DM or PBHs, we only considered the contributions to the heating rate from adiabatic cooling of electrons and baryons, and dissipation of acoustic waves. The additional  $y$  parameters caused by the CMB multipoles and by reionization are implemented in our code but deactivated in this analysis, as we treat them as perfectly distinguishable contributions, so that it is always possible to subtract them from an eventual observation.

---

<sup>15</sup>As long as we are only interested in the sensitivity to cosmological parameters, we can use mock likelihoods even when we account for completed experiments like FIRAS and Planck. This means that we do not include real data, but use a likelihood with the same sensitivity as the actual one, leading to the same error bars. This approach offers several technical and numerical advantages over using the actual likelihoods [190].

**Table 1.** Expected  $1\sigma$  sensitivity to the parameters of the  $\Lambda$ CDM model extended with the running of the spectral index, of different combinations of CMB anisotropy and SD experiments. We also report the 95% CL upper bounds on the derived  $y$  and  $\mu$  parameters.

Parameter	Planck	Planck+FIRAS	Planck+PIXIE	LiteBIRD+CMB-S4	LiteBIRD+CMB-S4+PRISM
$\sigma(10^2\omega_b)$	0.016	0.017	0.016	0.0038	0.0031
$\sigma(\omega_{\text{cdm}})$	0.0013	0.0013	0.0012	0.00029	0.00027
$\sigma(h)$	0.0058	0.0057	0.0057	0.0012	0.0011
$\sigma(z_{\text{reio}})$	0.46	0.46	0.45	0.20	0.20
$\sigma(10^9 A_s)$	0.021	0.021	0.020	0.0083	0.0079
$\sigma(n_s)$	0.0038	0.0037	0.0036	0.0017	0.0016
$\sigma(10^3 n_{\text{run}})$	6.4	6.3	3.5	2.6	0.60
$10^9 y$	-	< 3.79	< 3.70	-	< 3.54
$10^8 \mu$	-	< 3.36	< 2.46	-	< 2.01

Furthermore we also neglect the presence of galactic and extra-galactic observational foregrounds, which are expected to have a large impact at frequencies above 1 THz, as discussed e.g. in [30, 125, 189] (see Figure 2 of [125] and Figure 1 of [30]). Our current approach consists in considering only frequencies  $\nu \leq 1$  THz in the mock likelihoods. We leave a more accurate implementation of these foregrounds for future work.

#### 4.1 Running spectral index

Since the main dependence of the heating rate predicted by  $\Lambda$ CDM is on the primordial power spectrum, the first cosmological model to which we apply our joint CMB anisotropy and SD pipeline is a minimal extension of the standard  $\Lambda$ CDM model including the running of the spectral index  $n_{\text{run}}$ . This additional parameter is predicted to be very small in single-field slow-roll models [191], and constraining its value could help distinguish between several inflationary scenarios (see e.g., [192–194]).

In this case, although the constraining power of CMB anisotropy measurements has already provided remarkably good results, the inclusion of SDs could not only improve the current bounds, but also extend their validity up to much smaller scales than those considered by any previous or future CMB anisotropy mission [195, 196] (see e.g. in Figure 4 of [195] and Figure 9 of [196]). In fact, the power-law scale-dependence of the primordial power spectrum  $P_R(k)$  at Fourier modes higher than  $1 \text{ Mpc}^{-1}$  is still poorly constrained, and considering PIXIE-like experiments would help us achieve tighter bounds up to scales in the order of  $10^4 \text{ Mpc}^{-1}$ . The distortions are furthermore determined by small-scale perturbations while they still are in the linear regime. This is a different situation than with future 21cm and LSS surveys, in which the effects of a running spectral index and of non-linear structure formation could be difficult to discriminate at  $k > 1 \text{ Mpc}^{-1}$  due to non-linear effects.

We fitted the fiducial model with our mock likelihood and flat priors on the parameters  $\{h, \omega_b, \omega_{\text{cdm}}, n_s, A_s, z_{\text{reio}}, n_{\text{run}}\}$ . The amplitude and spectral index are defined at the pivot scale  $k = 0.05 \text{ Mpc}^{-1}$ . In Figure 7 we show the resulting two-dimensional posterior distributions of the three primordial power spectrum parameters, as well as the derived  $y$  and  $\mu$  parameters for Planck, Planck+FIRAS, Planck+PIXIE, LiteBIRD+CMB-S4, and LiteBIRD+CMB-S4+PRISM. A summary of the bounds obtained is given in Table 4.1.

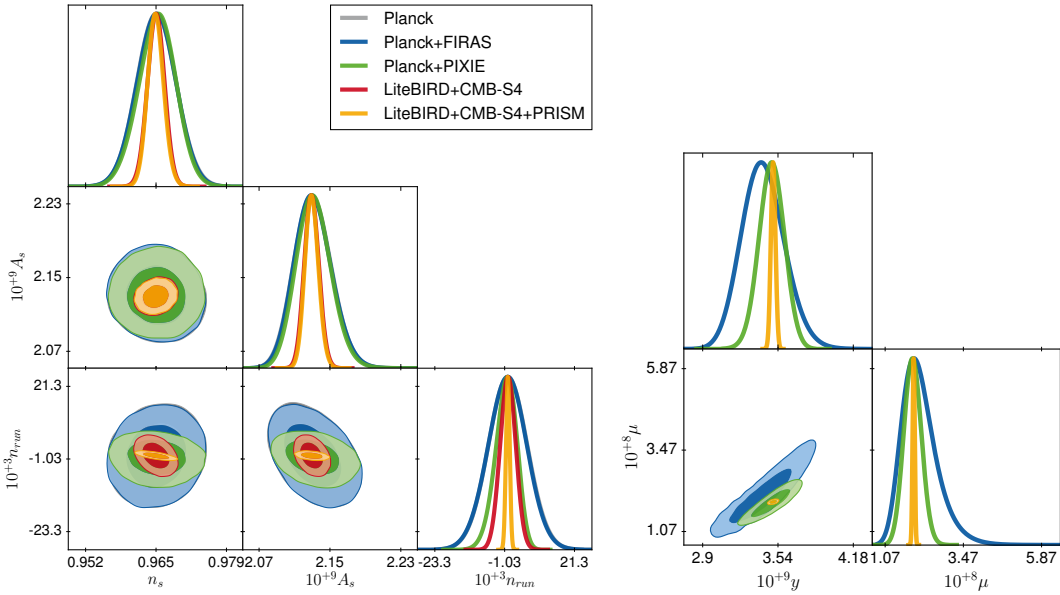


**Figure 7.** One-dimensional posteriors and two-dimensional contours (68% and 95% CL) for the parameters mostly affected by SDs, i.e. the spectral amplitude  $A_s$ , the spectral index  $n_s$  and its running  $n_{\text{run}}$ , and the derived SD parameters  $y$  and  $\mu$ .

As expected, the addition of FIRAS to the Planck likelihood does not provide any additional information. With the addition of PIXIE, while the bounds on  $A_s$  and  $n_s$  do not change with respect to the Planck ones, a substantial improvement on  $n_{\text{run}}$  bounds is present, which shows that SDs have the potential to improve the current CMB bounds on the running of the spectral index [51, 76, 197, 198]. This improvement of the error bars, driven by the presence of the PIXIE, also suggests that SD missions would indeed be able to extend the validity of the bounds up to  $10^4 \text{ Mpc}^{-1}$ , as mentioned before. Similarly, the addition of PRISM to the LiteBIRD+CMB-S4 case significantly improves the bounds by a factor 4.5. It is interesting to note that in the particular case of the running of the spectral index, the addition of PIXIE to the Planck likelihood provides nearly the same constraints as the combination of LiteBIRD and CMB-S4.

Note that in Figure 7, there is a vertical offset between the best-fit values of the  $y$  and  $\mu$  parameters in the different forecasts, while one would expect all contours to be centered around some fixed fiducial values. Still, this is consistent. Indeed, Section 3.2 show that the choice of the frequency array for a given detector strongly influences the Gram-Schmidt decomposition into  $y$  and  $\mu$  distortions. This also affects the shape of the branching ratios. As a consequence, the position of the  $y$  and  $\mu$  contour in Figure 7 is affected by the frequency array. This can be interpreted as the detector disambiguating  $\mu$  and  $y$  distortions differently. Our bounds on other parameters are derived from the full distortion shape, and are not affected by this disambiguation effect. On the other side, the width of the contour is set by the sensitivity of the mission, as clear from the comparison of the PIXIE and PRISM cases.

Finally, note that there are several other modifications of the standard primordial power spectrum that could be tested with SDs. Some particularly interesting examples are, for instance, given in Section 5 of [52], [39], and references therein.

These include the specific cases of steps in the amplitude or slope of the primordial power spectrum. Additional extensions of the standard power spectrum could include the running of the running or even higher derivative parameters, to stay within this framework of slow-roll inflation (see e.g. [199]). In order to constrain this class of models, SDs might be particularly well suited. In fact, to avoid the tight CMB anisotropy constraints, many models predict deviations from the standard primordial power spectrum only at scales larger than  $1 \text{ Mpc}^{-1}$ . As already mentioned before, in this region of parameter space, SDs are a more powerful constraining tool than CMB anisotropies.

## 4.2 Dark matter annihilation

We performed a similar analysis for a  $\Lambda$ CDM model including s-wave DM annihilation, parametrized with the annihilation efficiency parameter  $p_{\text{ann}}$  presented in 2.4.4 (under the simplified and optimistic assumption  $f_{\text{eff}}(z) = 1$ ). We do not show our results for that case, because they simply confirm earlier works [39] in that SD experiments will not improve bounds on  $p_{\text{ann}}$  with respect to CMB anisotropy observations.

We should note, however, that if DM annihilation was detected, the combination of CMB anisotropy and SD data would be very useful for discriminating between different models, since the spectral distortion spectrum and the angular polarization spectrum would be sensitive to different assumptions on the branching ratios and on the energy spectrum of the annihilation products.

## 4.3 Dark matter decay

In the third case we are going to focus on, which is the decay of DM into electromagnetic particles, the importance of SDs is particularly striking. Indeed, in this scenario, the energy injection history directly depends on the lifetime and abundance of the decaying DM particle [26, 39, 76]. Consequently, constraints from CMB anisotropies and SDs are complementary and apply to two separate regions of the parameter space. On the one hand, DM particles with lifetimes between  $10^5$  s and  $10^{12}$  s mainly affect the thermal history of the universe before recombination, thus almost exclusively causing SDs. On the other hand, lifetimes between  $10^{12}$  s and  $10^{25}$  s are strongly constrained by CMB observations (see e.g., Figure 11 of [76] and Figure 5 of [160] for a graphical representation).

In this analysis we consider a simplified model with  $f_{\text{eff}} = 1$ , i.e., we adopt the on-the-spot approximation (which is normally very accurate for energy injection prior to recombination) and we assume that all decay products interact electromagnetically.

In order to derive bounds on the fraction  $f_{\text{frac}}$  of DM that decays and its lifetime  $\tau_{\text{dec}} = 1/\Gamma_{\text{dec}}$ , we consider a 6+2 extension of the standard  $\Lambda$ CDM model with flat priors on  $\{h, \omega_b, \omega_{\text{cdm}}, n_s, A_s, z_{\text{reio}}\} + \{\log_{10} f_{\text{frac}}, \log_{10} \tau_{\text{dec}}\}$ , and we scan the parameter space with an MCMC sampler. However, because of the non-convex topology of the parameter space spanned by  $\log_{10} f_{\text{frac}}$  and  $\log_{10} \tau_{\text{dec}}$ , a single MCMC would be extremely slow to converge.

In order to avoid this issue, we slice the parameter space along  $\tau_{\text{dec}}$  at several values in the range between  $10^4$  s and  $10^{27}$  s, and we sample the remaining 6+1 dimensional parameter space with separate MCMC runs. As a result, we obtain an array of values for  $f_{\text{frac}}$  that we can interpolate along the  $\tau_{\text{dec}}$  slices. For each slice we adopt a top-hat prior on  $\log_{10} f_{\text{frac}}$  in the range from  $-13$  to  $0$ .

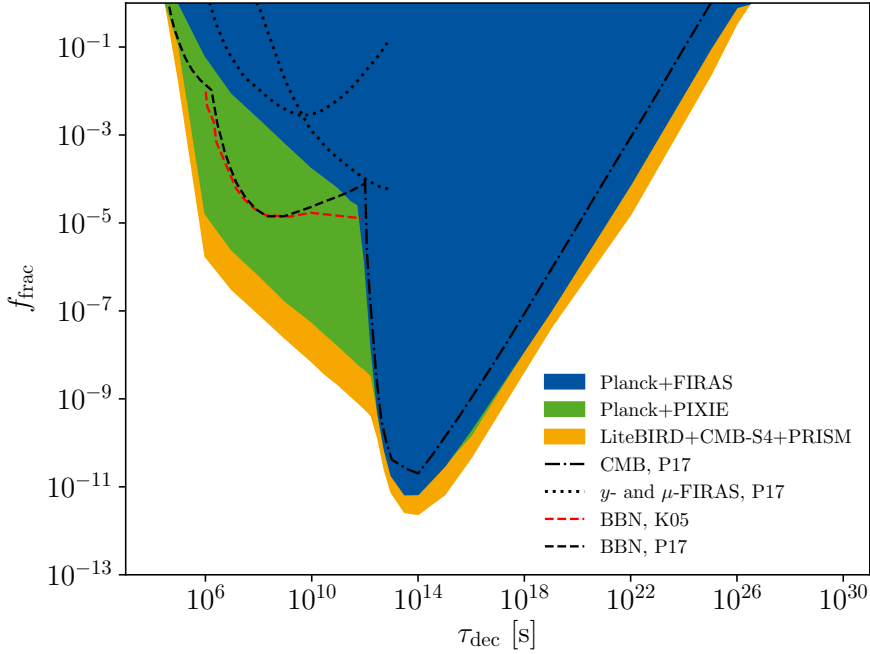


**Figure 8.** 95% CL bounds on the decaying DM fraction as function of the particle lifetime. The black lines correspond to the bounds displayed in Figure 5 of [160] (labeled P17 for brevity), while the red dashed line corresponds to the BBN constraints from [161] (adapted from [76] and labeled K05).

The results are displayed in Figure 8. The colored regions represent regions of parameter space *excluded* by the condition  $\chi^2 > \chi_{\min}^2 + 4$ . We also show the contours calculated in [160] (dotted line for SDs and dashed-dotted line for CMB anisotropy constraints). These are to be compared with the case of Planck+FIRAS (blue region) and several details are worth noticing. First of all, for the exclusion bounds in the range  $10^5 \text{ s} < \tau_{\text{dec}} < 10^{13} \text{ s}$ , which are dominated by SDs, the authors of [160] derived some separate bounds from  $y$  and  $\mu$  distortions based on [70]. Thus our contours are smoother and in principle more reliable, especially in the region where  $y$  and  $\mu$  distortions are produced in similar proportions.

When moving to higher values of the DM lifetime, for which the bounds are dominated by CMB anisotropies, we also notice that we have slightly tighter bounds than in [160]. This can be attributed mainly to different assumptions on  $f_{\text{eff}}$  (we take  $f_{\text{eff}} = 1$ , while [160] assumes two specific values  $f_{\text{eff}} < 1$  motivated by particular decay channels), as well as minor differences in the MCMC analysis: the choice of lower prior boundary for  $\ln f_{\text{frac}}$  and the slightly different likelihood for Planck – full Planck 2015 likelihood in [160], mock likelihood approximating Planck 2018 in this work.

Finally, in Figure 8, we compare the limits on the decaying DM fraction set by SDs with the BBN bounds derived in [161] and [200]. At the moment, BBN bounds are nearly two orders of magnitude better than FIRAS bounds. However this situation is likely to change in the future. On the one hand, we only expect marginal improvements on the BBN side (and the comparison of [161] and [200] only shows a very small improvement over one decade). On the other hand, a PIXIE-like mission would improve over FIRAS bounds by up to two orders of magnitude, and PRISM by almost three orders, leading to much stronger bounds than BBN.

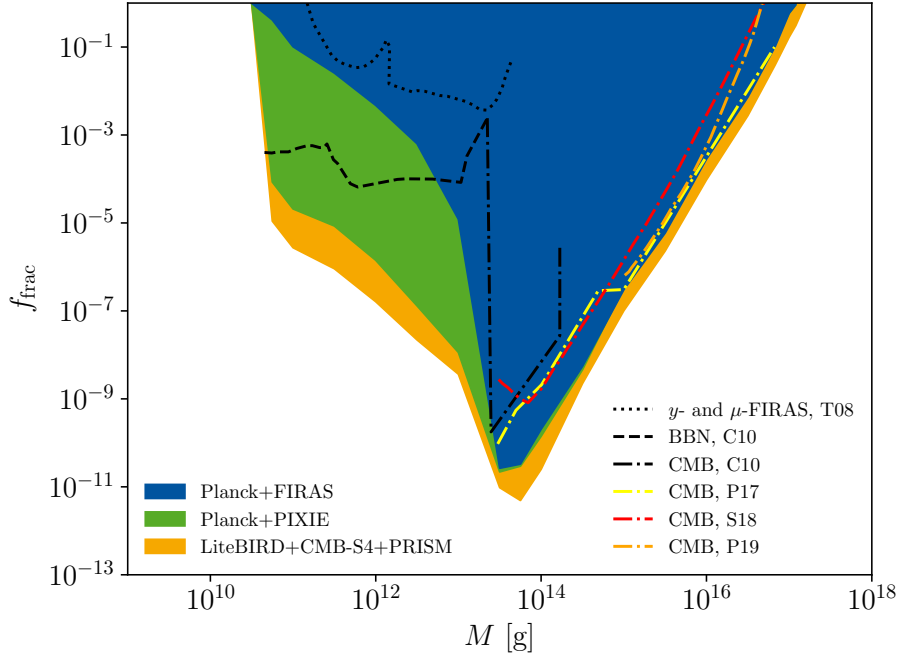


**Figure 9.** 95% CL bounds on the PBHs fraction as function of their mass. The black dashed-dotted line corresponds to the bounds from [45] (here labeled C10 for brevity), the red one to the bounds from [160] (P17), the orange one to the bounds from [99] (S18) and yellow one to the bounds from [201] (P19). The dotted black line represents the SDs constraints and is taken from [44], while the BBN constraints are the same as in [45].

#### 4.4 Primordial Black Hole evaporation

As already seen in Section 2.4.4, the heating rate caused by the evaporation of PBHs has very similar characteristics to that of decaying DM. However, PBHs are generated through primordial overdensities that are directly related to the shape of the inflationary curvature perturbations, and can thus be used to constrain the inflationary period itself, in addition to the many other effects already mentioned in Section 2.4.4 (and references therein). Additionally, PBHs allow for a possible explanation of DM which does not involve modifications of the standard model of particle physics.

It is thus very important to test this model at all scales. As in the case of DM decay, SD constraints lay in a region of the parameter space where bounds from CMB anisotropies are absent, and can, therefore, play a crucial and complementary role. For this purpose, the authors of [44] already computed semi-analytical SD bounds on the PBH mass using FIRAS, while CMB anisotropy bounds were estimated by [45, 99, 160, 201]. Moreover, in [45], the FIRAS bounds have been compared to BBN constraints.

In comparison, the current analysis brings several improvements, such as the calculation of the full SD shape, a joint fit to current and future CMB anisotropy and SD data, and the development of a new approximation to calculate the heating rate caused by PBHs at early times, especially when QCD effects are important. The latter can be found in Appendix C.2.

We consider an extension of  $\Lambda$ CDM featuring the fraction of DM in the form of PBHs,  $f_{\text{frac}}$ , and the individual black hole mass  $M$ . For each value of  $M$  in the interval  $[10^{10} - 10^{18}]$  g, we scan the remaining 6+1 dimensional parameter space with an MCMC sampler, assuming a top-hat prior on  $-15 < \log_{10} f_{\text{frac}} \leq 0$ .

Our results are shown in Figure 9. The blue region corresponds to the Planck+ FIRAS case, and can be compared with the dashed-dotted lines for previous CMB anisotropy bounds (black for [45], red for [160], orange for [99], and yellow for [201]), with the dotted line for previous SDs constrains, and finally with dashed lines for previous BBN constraints.

For PBH masses bigger than approximately  $10^{13.5}$  g, the constraints are dominated by CMB anisotropies. Comparing with previous bounds, we observe that for PBH masses larger than  $10^{15}$  g the agreement is very good, in particular with respect to the more recent calculations performed in [201]. However, in the mass range between  $10^{13.5}$  g and  $10^{15}$  g our results disagree with other references by up to one order of magnitude. This is mostly due to our treatment of the QCD-confinement scales. Indeed, all references but [99] do not account for the effects of QCD confinement. However, the public version of ExoCLASS used in [99] appears to have a small typo in the calculation of the factor  $Q_{\text{QCD}}$ , which can be identified by comparing with Equation (C.5). As a consequence, in all previous references, the value of  $\mathcal{F}(M)$  was larger than in the current analysis (to appreciate the impact of the  $Q_{\text{QCD}}$  factor, one can compare Figure 4 and Figure 5 of [99]). With our updated modeling of  $\mathcal{F}(M)$ , the energy injection rate is smaller for each given value of the mass  $M$ , but evaporation and energy injection take place over a considerably longer span of time, leading to stronger CMB anisotropy bounds.

For PBH masses smaller than approximately  $10^{13.5}$  g, the constraints from CMB SDs become dominant, and our results can be compared with those of [44]. However, this pioneering analysis is more than a decade old, and has several limitations. First, it relies on WMAP best-fits values, with differences up to 10% with respect to our fiducial values. Second, their approximation of the branching ratios is relatively strong (see the second approximation mentioned in Appendix B.3), and neglects the gradual transition between the  $\mu$  and  $y$  eras. Third, the computation of  $\mathcal{F}(M)$  in [44] omits several of the particles listed in Table 2, as well as QCD confinement effects, which could explain the relatively strong deviation from our predictions at mass scales between  $10^{12}$  g and  $10^{13.5}$  g. Finally, as already discussed in the case of decaying DM, employing the FIRAS bounds on the  $y$  and  $\mu$  parameters computed in [70] can introduce a difference by a factor 2 to 10 with respect to our 95% CL limits, that are derived from the full distortion  $\Delta I_{\text{tot}}(\nu)$  (our bounds are however slightly optimistic since we neglect foreground contamination).

Finally, we find that PIXIE-like missions would significantly improve the bounds for PBH masses between  $10^{10}$  g and  $10^{13.5}$  g. Like in the case of decaying DM, the gain with respect to BBN bounds is between 1 and 3 orders of magnitude for PIXIE, while the limits from PRISM show an even larger margin for improvement.

Note that all the aforementioned bounds originate only from the thermal effects that the PBH evaporation has on the CMB photons. This means that, for instance, we currently neglect the additional constraints caused by the transfer of energy density from DM (in form of PBHs) to baryonic matter or radiation. These additional contributions, depending on the injection time, would further affect BBN and the different CMB power spectra, thus increas-

ing the deviations from  $\Lambda$ CDM. In this respect, our bounds can be considered conservative. It is, however, important to underline that such effects would only affect the results presented in this section for PBH fractions lower than roughly  $10^{-3} - 10^{-2}$ , which corresponds to the current observational precision of the different energy densities. In our case, this would correspond to PBH masses below  $10^{11} - 10^{12}$  g. Since a precise implementation of the additional constraints presents several challenges such as a proper modeling of the secondary cascades, the inclusion of these additional contributions is left for future work.

## 5 Conclusions

Within this work we have presented a detailed and pedagogical introduction to the topics of SDs and energy injection throughout the thermal history of the universe. We have described the origin of SDs, shown how to calculate them, and discussed their significance to our understanding of the universe. We have also touched upon the complexity of the various energy injection mechanisms in the early and late universe.

We have subsequently presented the numerical implementation of SDs and several energy injection mechanisms in the Boltzmann solver CLASS. Although the actual content of our extensions are largely based on some modules of two previously published codes, COSMOTHERM and ExoCLASS, we have developed a unified numerical framework with improved structure, homogeneous conventions, and several new features. For example, it is now possible to compute SDs for arbitrary heating histories and any detector setup, specifying the precise detector sensitivity per frequency bin.

The inclusion of SDs in the more general framework of CLASS allows for a parallel computation of CMB SDs, CMB anisotropies, the matter power spectrum, and many other cosmological quantities. This synergy is particularly well suited for models such as decaying DM and evaporating PBHs, whose free parameters can span several orders of magnitude, influencing the whole thermal history of the universe at all scales. We have shown the substantial benefit that SDs can bring to the other more conventional probes, either providing complementary bounds, such as in the case of CMB anisotropies, or even surpassing current constraints by 2-3 orders of magnitude, as in the case of BBN.

Although the current implementation already considers a large variety of physical effects and can be applied to several models, there is still much work to be done. First of all, our calculation of SDs in the  $\Lambda$ CDM model does not yet include CRR. This could be achieved implementing the work already done in the framework of COSMOSPEC into our new version of CLASS, which would then include all effects of  $\Lambda$ CDM. Furthermore, an investigation of the frequency dependence of energy injection mechanisms and its observable effects is left for future work, following the lines of [64]. Additionally, to make our forecast more realistic, we should incorporate a precise treatment of observational foregrounds in the SD likelihoods.

Aside from these limitations, with one single code exploiting the synergy between CMB SDs and anisotropies, it is now possible to constrain many cosmological quantities over a range of values spanning up to 25 orders of magnitude, as we have seen in the case of decaying DM. This opens the door to the analysis of several other interesting models, including for instance non-standard inflationary scenarios, or models with interactions between particles in the visible and dark sectors. In this work we have shown the far-reaching possibilities of combining CMB anisotropies and SDs, and with the framework we have developed, we are now prepared to fully make use of this synergy.

## Acknowledgements

We thank Patrick Stöcker, Yacine Ali-Haïmoud, and Chris Byrnes for very useful exchanges. We especially want to thank the referee for the constructive suggestions that have led to more clarity in our paper. ML is supported by the “Probing dark matter with neutrinos” ULB-ARC convention. NS acknowledges support from the DFG grant LE 3742/4-1. JL acknowledges support for this project from the DFG. DH was supported by the DFG grant LE 3742/3-1, and during the last stages of this work, by the FNRS research grant number F.4520.19. This work has received funding from the European Research Council (ERC) under the European Union’s Horizon 2020 research and innovation program (grant agreement No 725456, CMBSPEC) as well as the Royal Society (grant UF130435). Simulations for this work were performed with computing resources granted by JARA-HPC from RWTH Aachen University under the project jara0184.

## A Further details on the photon Boltzmann equation

### A.1 A note on partial derivatives and the photon Boltzmann equation

It is a well known fact that a partial derivative depends on the chosen coordinate system, in such a sense that it depends on which quantities are held constant while taking the derivative. This especially applies to the choice of holding  $x$  or  $p$  constant while taking the partial time derivative of the photon phase-space distribution.

To appreciate this fact, note that we have explicitly defined  $x = p/T_z \propto a \cdot p$  so that  $dx/dt = 0$ . This implies that the derivative holding  $p$  constant has to keep track of the the phase-space distribution redshifting through the decreasing photon momentum, while the term holding  $x$  constant already accounts for that fact.

Let us denote the quantity we hold constant during the partial derivative as an index to the brackets of the derivative, i.e.  $(\partial y/\partial x)_a$  will hold the quantity  $a$  constant while taking the partial derivative of  $y$  with respect to  $x$ .

We then find explicitly for the general photon Boltzmann equation

$$C[f] = \frac{df(q^\mu, p^\mu)}{dt} = \left( \frac{\partial f}{\partial q^\mu} \right)_{p^\mu} \frac{dq^\mu}{dt} + \left( \frac{\partial f}{\partial p^\mu} \right)_{q^\mu} \frac{dp^\mu}{dt}. \quad (\text{A.1})$$

We now split the dependencies into time and space components as  $q^\mu = (t, \mathbf{q})$  and  $p^\mu = (E, \mathbf{p}\mathbf{n})$ . Note that since non-virtual particles obey  $E^2 = p^2 + m^2$  with constant mass  $m$ , the dependence on  $E$  is equivalent to the dependence on  $p$ . We could choose either variable to obtain

$$C[f] = \frac{df(t, p)}{dt} = \left( \frac{\partial f}{\partial t} \right)_p \frac{dt}{dt} + \left( \frac{\partial f}{\partial \mathbf{q}} \right)_p \frac{d\mathbf{q}}{dt} + \left( \frac{\partial f}{\partial \mathbf{n}} \right)_t \frac{d\mathbf{n}}{dt} + \left( \frac{\partial f}{\partial p} \right)_t \frac{dp}{dt}. \quad (\text{A.2})$$

Using the fact, that  $\partial f/\partial \mathbf{q} = 0$  and  $\partial f/\partial \mathbf{n} = 0$  for the homogeneous background solution, we find additionally that

$$C[f] = \frac{df(t, p)}{dt} = \left( \frac{\partial f}{\partial t} \right)_p + \left( \frac{\partial f}{\partial p} \right)_t \frac{dp}{dt}. \quad (\text{A.3})$$

Finally, using  $dp/dt = -Hp$  from Equation (2.1), we find

$$C[f] = \frac{df(t, p)}{dt} = \left( \frac{\partial f}{\partial t} \right)_p - Hp \left( \frac{\partial f}{\partial p} \right)_t. \quad (\text{A.4})$$

Substituting now  $p \rightarrow x(t, p)$ , we obtain instead also

$$C[f] = \frac{df(t, x)}{dt} = \left( \frac{\partial f}{\partial t} \right)_x + \frac{dx}{dt} \left( \frac{\partial f}{\partial x} \right)_t = \left( \frac{\partial f}{\partial t} \right)_x, \quad (\text{A.5})$$

which is equivalent to saying

$$\left( \frac{\partial f}{\partial t} \right)_p - Hp \left( \frac{\partial f}{\partial p} \right)_t = \left( \frac{\partial f}{\partial t} \right)_x. \quad (\text{A.6})$$

Holding  $x = p/T_z$  constant while calculating the partial derivative with respect to time is thus fundamentally different to holding the momentum  $p$  constant. The difference between these two approaches is exactly subtracting the momentum shift  $p \propto a^{-1} \propto T_z$ .

Note that the conclusion of Equation (2.3) can be similarly obtained using Equation (A.4). For a non-interacting ( $C[f] = 0$ ) photon bath, one easily finds (using  $da = aHdt$ )

$$\left( \frac{\partial f}{\partial \ln a} \right)_p = \left( \frac{\partial f}{\partial \ln p} \right)_a. \quad (\text{A.7})$$

This is fulfilled for any solution of the kind  $f(a \cdot p)$ . Since, however,  $p \propto 1/a$  for any individual photon, their total distribution is conserved independently of its precise shape.

## A.2 Evolution of the chemical potential $\mu$

The evolution of the effective chemical potential  $\mu$  of the photons is a difficult problem, which has been extensively discussed in the literature (e.g., [20, 23, 77, 77, 80, 82, 96, 202]). Here, we simply want to recap the most important results.

The general solution of the photon Boltzmann equation including CS, DC, and BR permits a  $\mu$  distortion, which is a function of both frequency and time.<sup>16</sup> Its dependence can usually be written as

$$\mu(x, t) \approx \mu_0(t) e^{-x_c(t)/x}, \quad (\text{A.8})$$

where  $x_c(t)$  is the critical frequency of the DC and BR processes (see [23, 24, 77, 96]), and  $\mu_0(t)$  obeys the differential equation

$$\frac{d\mu_0}{d\tau} = C_\mu \frac{\dot{Q}}{\rho_\gamma} - \gamma_N \frac{T_\gamma x_c \mu_0}{m_e}, \quad (\text{A.9})$$

with  $\dot{Q}$  being the effective heating rate, and  $\gamma_N = (4/3)(C_\mu/G_2)$ , where  $C_\mu$  and  $G_2$  are the same as in Equations (2.24) and (2.16), respectively. This represents an exponentially decaying effective chemical potential with decay time of approximately

$$\tau_\mu(z) \approx \gamma_N \int \frac{T_\gamma x_c}{m_e} d\tau. \quad (\text{A.10})$$

This defines then the distortion visibility function as  $\exp(-\tau_\mu(z))$ , which can subsequently be approximated as  $\exp(-(z/z_{\text{th}})^{5/2})$ , where  $z_{\text{th}}$  is defined as in Equation (2.35).

## B Further details on the spectral distortions

### B.1 Second order temperature shift

The second order contribution to the temperature shift is very easy to calculate (assuming  $\epsilon = \Delta T/T_z \ll 1$ ):

$$B\left(\frac{x}{1+\epsilon}\right) \approx B\left(\frac{x}{1+\epsilon}\right)\Big|_{\epsilon=0} + (\partial_\epsilon B)\left(\frac{x}{1+\epsilon}\right)\Big|_{\epsilon=0} \epsilon + (\partial_\epsilon^2 B)\left(\frac{x}{1+\epsilon}\right)\Big|_{\epsilon=0} \epsilon^2/2 + \mathcal{O}(\epsilon^3). \quad (\text{B.1})$$

Using now  $y = x/(1+\epsilon)$ ,  $\partial_\epsilon = -x/(1+\epsilon)^2 \partial_y$  and  $B'(x) \equiv \partial_x B(x)$ , we find immediately

$$\begin{aligned} B(y) &\approx B(x) - \frac{xB'(y)}{(1+\epsilon)^2}\Big|_{\epsilon=0} \epsilon + \left(\partial_\epsilon \left(-\frac{xB'(y)}{(1+\epsilon)^2}\right)\right)\Big|_{\epsilon=0} \epsilon^2/2 + \mathcal{O}(\epsilon^3) \\ &= B(x) - xB'(x)\epsilon + \left(\left(2\frac{xB'(y)}{(1+\epsilon)^3}\right) + \frac{x^2}{(1+\epsilon)^4} \partial_y B'(y)\right)\Big|_{\epsilon=0} \epsilon^2/2 + \mathcal{O}(\epsilon^3) \\ &= B(x) - xB'(x)\epsilon + (2xB'(x) + x^2 B''(x))\epsilon^2/2 + \mathcal{O}(\epsilon^3). \end{aligned} \quad (\text{B.2})$$

By the definitions of  $G(x) = -xB'(x)$  and  $Y(x) = -1/x^2 \partial_x(x^3 G(x)) = 4xB'(x) + x^2 B''(x)$ , we then obtain

$$B(y) \approx B(x) + G(x)\epsilon + (2G(x) + Y(x))\epsilon^2/2 + \mathcal{O}(\epsilon^3). \quad (\text{B.3})$$

Converting  $\epsilon \rightarrow g$ , we find the created temperature shift as [127, 128]

$$\Delta f(x) \approx G(x)g(1+g) + Y(x)g^2/2 + \mathcal{O}(g^3). \quad (\text{B.4})$$

Adding now the normalization, and keeping only terms up to second order directly translates into  $\tilde{g}(1 + \tilde{g}/4)\mathcal{G}(x) + \tilde{g}^2/8\mathcal{Y}(x)$ , as stated in Section 2.3.

---

<sup>16</sup>In Section 2.1 we described it as a constant. Note that this was true at any single time  $t$ , allowing for different  $C$  at different times, i.e., a function  $C(t)$ . The  $\mu$  distortion is only large and independent of frequency for  $x \gg x_c$ , while it is suppressed due to DC and BR for  $x \ll x_c$  as argued in [96].

The reason to include the second order in  $g$  is to avoid misattributing the  $\tilde{g}^2/8$  term to the  $y$  distortion. Since  $g$  can vary within the error bars of the  $T_0$  determination, which is up to around  $2 \cdot 10^{-4}$ , it adds a term of up to around  $2 \cdot 10^{-8}$  to the  $y$  distortion. Thus, the error made by neglecting the term is small, but possibly measurable. We chose to include it in accordance with [76]. Terms of order  $g^3$  are of order  $10^{-12}$  [128], and are thus far below sensitivity and also less important than better modeling of other effects. We will neglect the third order effects here.

## B.2 Heating and Distortions

The idea of this short derivation is to point out explicitly that the redshifting term of the PPSD directly translates into a redshifting term for the energy density of the photons. This has to be taken into account when calculating the total SDs, since it gives a slightly surprising relation in the end.

Integrating the photon Boltzmann equation (A.1) gives

$$\begin{aligned}\dot{Q} &= \int C[f] E d^3 p = \int \frac{df}{dt} E d^3 p = \int \frac{df}{dt} 4\pi p^3 dp \\ &= \int \left[ \left( \frac{\partial f}{\partial t} \right)_p - H p \left( \frac{\partial f}{\partial p} \right)_t \right] 4\pi p^3 dp = \frac{\partial \rho}{\partial t} - 4\pi H \int p^4 \left( \frac{\partial f}{\partial p} \right)_t dp \\ &= \frac{\partial \rho}{\partial t} - 4\pi H [p^4 f] \Big|_0^\infty + 4 \cdot 4\pi H \int p^3 f dp = \frac{\partial \rho}{\partial t} + 4H\rho ,\end{aligned}\quad (\text{B.5})$$

where we have *defined* the heating rate as the change in energy density due to the collision operator  $C[f]$ . We simply find

$$\frac{\partial \rho_\gamma}{\partial t} + 4H\rho_\gamma = \dot{Q} \quad \implies \quad \frac{\partial(a^4 \rho_\gamma)}{\partial t} = a^4 \dot{Q} . \quad (\text{B.6})$$

The solution to this differential equation can be written as  $\rho_\gamma(t) = \rho_z(t) + \Delta\rho(t)$  with homogeneous solution  $\rho_z(t)$  and particular solution  $\Delta\rho(t)$ .

Since the homogeneous solution is the one where the right hand side vanishes, it corresponds to the background solution without any heating, thus evolving exactly as  $\rho_z(t) \propto a^{-4}$ . On the other hand, the particular solution can be found by simple integration, giving us

$$\Delta\rho(t) = \frac{1}{a^4} \int_0^t a^4 \dot{Q} dt' = \rho_z(t) \int_0^t \frac{\dot{Q}}{\rho_z(t')} dt' . \quad (\text{B.7})$$

We thus find for the total change in energy density

$$\frac{\Delta\rho_\gamma}{\rho_\gamma} \Big|_{\text{tot}} = \frac{\Delta\rho(t_0)}{\rho_z(t_0)} = \int_0^\infty \frac{\dot{Q}}{(1+z)H\rho_z} dz = \int_0^\infty \frac{dQ/dz}{\rho_z} dz . \quad (\text{B.8})$$

Here we have used  $dz = -(1+z)Hdt$ .

Note furthermore that in several work present in the literature [31, 39, 63, 76], a different definition of the heating has been adopted with respect to the one used within this work. There, instead of defining  $Q$  in relation to the collision operator, the heating function has been defined as the total change in the photon energy density, i.e.  $Q_{\Delta\rho} = \Delta\rho(t)$ . One can easily show using Equation (B.6) that

$$\frac{\dot{Q}}{\rho_z} = \frac{\partial(\rho_\gamma/\rho_z)}{\partial t} = \frac{\partial(1 + \Delta\rho(t)/\rho_z)}{\partial t} = \frac{\partial(\Delta\rho(t)/\rho_z)}{\partial t} , \quad (\text{B.9})$$

where we used again the fact that  $\rho_z(t) \propto a^{-4}$  and  $\rho_\gamma(t) = \rho_z(t) + \Delta\rho(t)$ .

From Equation (B.9) it then follows that

$$\frac{\partial(\Delta\rho(t)/\rho_z)}{\partial z} = \frac{d(Q_{\Delta\rho}/\rho_z)}{dz} = \frac{1}{\rho_z} \frac{dQ}{dz} , \quad (\text{B.10})$$

where, for the sake of clarity, we referred to  $\dot{Q}$  as the heating rate following directly from the collision term and to  $\dot{Q}_{\Delta\rho}$  as the one defined according to the other convention occurring in the literature, proving the equivalence of the two definitions.<sup>17</sup>

### B.3 Branching ratios

In order to determine the shape of the branching ratios  $\mathcal{J}_a(z)$ , there are different approaches and, correspondingly, different levels of approximation. A possible classification has been proposed in [31] and in the next paragraphs we are going to review the main characteristics.

In a first very crude simplification, one could assume that the transitions between BB and  $\mu$  eras and between  $\mu$  and  $y$  eras occur sharply at a given redshift. Historically, these values are assumed to be  $z_{\text{th}} \approx 2 \times 10^6$  and  $z_{\mu y} \approx 5 \times 10^4$  [24, 96], approximately. Furthermore, in this first simplification, we are going to neglect the presence of residuals. In this case we have  $\mathcal{J}_T(z) = 1$  for  $z \geq z_{\text{th}}$ ,  $\mathcal{J}_\mu(z) = 1$  for  $z_{\mu y} \leq z \leq z_{\text{th}}$  and  $\mathcal{J}_y(z) = 1$  for  $z \leq z_{\mu y}$ . Otherwise, all functions are equal to zero.

This approximation can be relaxed by introducing a so-called visibility function for spectral distortions, i.e. a quantity determining how efficient the thermalization of SDs is. As first defined in [20] and resulting from Appendix A.2, this function takes form

$$f(z) \approx e^{-(z/z_{\text{th}})^{5/2}} , \quad (\text{B.11})$$

where  $z_{\text{th}} \approx 1.98 \times 10^6$  defines the "surface of the blackbody photosphere". In this approximation, the effect of DC emission was included [23]. Using the SDs visibility function, it is possible to see that even at redshift larger than  $z_{\text{th}}$  small  $\mu$  distortion can be created, while most of the released energy produces a change of the BB temperature. This leads to  $\mathcal{J}_\mu(z) = f(z)$  and  $\mathcal{J}_T(z) = 1 - f(z)$  for  $z \geq z_{\mu y}$  and leaves the other conditions unchanged.

A further improvement of the previous approximation can be achieved by considering that also the transition between  $\mu$  and  $y$  distortions does not take place exactly at  $z \approx z_{\mu y}$  but is rather gradual. It is therefore necessary to introduce a region where a sum of  $y$  and  $\mu$  distortions is present. In this case, the shape of these weighting functions has been studied in [63] with the resulting form

$$\mathcal{J}_y(z) = \left[ 1 + \left( \frac{1+z}{6.0 \times 10^4} \right)^{2.58} \right]^{-1} , \quad (\text{B.12})$$

$$\mathcal{J}_\mu(z) = \left\{ 1 - \exp \left[ - \left( \frac{1+z}{5.8 \times 10^4} \right)^{1.88} \right] \right\} f(z) , \quad (\text{B.13})$$

$$\mathcal{J}_T(z) = 1 - f(z) . \quad (\text{B.14})$$

Note however that, neglecting the presence of residuals as done in [63], the branching ratios do not add up to unity and, consequently, energy is not exactly conserved. To solve this problem, it is possible to redefine  $\mathcal{J}_\mu(z)$  as  $[1 - \mathcal{J}_y(z)]f(z)$ , as suggested in [31].

Finally, an exact solution to the branching ratios problem exists and has been found by [76]. The details are discussed in depth in Section 3.2. The calculation of SDs with any of the branching ratio approximations mentioned above is possible using the new CLASS implementation. A direct comparison of the resulting amplitudes of the spectral distortions is performed in Table 1 of [31].

---

<sup>17</sup>Note that it is still important not to use the two conventions interchangeably. One has to consistently stick with either definition and pay attention to the corresponding factor of  $\rho_z$  inside or outside of the derivative.

## C Further details on the heating mechanisms

### C.1 Possible approximations for injection efficiency and deposition function

In the following paragraphs we are going to review three examples of how to model the dependence of the deposition fraction of each channel on redshift and/or free electron fraction, all of which are implemented in CLASS. However, the one used throughout this work is the GSVI2013 [103] approximation summarized below.

#### CK2004

Firstly, we are going to discuss the pioneering Monte Carlo simulations of [203] and the more recent approximation proposed by [101], both of which provide excellent leading order approximations. Regarding the interaction between primary electrons and the photon bath, the computation performed in the former work considered only two main effects: Coulomb collisions with thermal electrons and collisional ionization or excitation of HI, HeI, and HeII. Nearly 20 years later, [101] proposed then an analytical approximation of their results to split the fractional energy deposition as

$$\chi_{\text{ion}} = \frac{1 - x_e}{3}, \quad \chi_{\alpha} = \frac{1 - x_e}{3}, \quad \text{and} \quad \chi_h = \frac{1 + 2x_e}{3} \quad (\text{C.1})$$

into the various channels. Here  $\chi_{\text{ion}/\alpha/h}$  represents the deposition fraction into the ionization, Lyman- $\alpha$  excitation, or heating channels. Note this set of equations is also consistent with the expectation that in a fully ionized medium, all the injected energy is ultimately deposited in the form of heat. On the other side, when the medium is neutral, the energy budget is equally divided between the three channels. However, as  $x_e > 1$  the above approximation breaks down, and we have to set  $\chi_h = 1$ , while the other channels remain at  $\chi_{\text{ion}} = \chi_{\alpha} = 0$ .

#### PF2005

Several different extensions of the CK2004 approximation have been proposed in order to include helium recombination. Most notably, the approximation introduced in [102] and used within the COSMOTHERM code has expanded the equations as

$$\chi_{\text{ion}} = \frac{1}{3} - \frac{x_e}{3(1 + f_{\text{He}})}, \quad \chi_{\alpha} = \frac{1}{3} - \frac{x_e}{3(1 + f_{\text{He}})}, \quad \text{and} \quad \chi_h = \frac{2}{3} + \frac{x_e}{3(1 + f_{\text{He}})}. \quad (\text{C.2})$$

Here, the approximation begins to break down only at  $x_e > 1 + f_{\text{He}}$ , which is the ionization fraction including singly-ionized helium. The second helium recombination is then taken into account. However, the approximations remain linear and based on the original Monte Carlo Simulations of [203]. Furthermore, helium is still not treated with a separate branching channel.

#### GSVI2013

An additional step towards a more realistic description of the deposition fractions carried out by [204] and the updated version described in [103]. In this case, again extensive Monte Carlo simulations have been performed. However, many differences with respect to [203] are present, like e.g., a more advanced treatment of the cross-section calculations involving collisional ionization and excitation from electron-photon, electron-electron, and free-free interactions. Another improvement consists in a more accurate prediction of the radiation produced by the excitation processes, influencing the amount of energy deposited into low-energy photons not interacting with the gas, and the amount deposited to the Lyman- $\alpha$  background. In addition to that, H and He are also treated separately, splitting therefore  $\chi_{\text{ion}}$  into  $\chi_{\text{ion},\text{H}}$  and  $\chi_{\text{ion},\text{He}}$ . Note furthermore that [103] also introduced an extended analytical approximation taking into account helium (see their Equation (11)). The final results are summarized in Table V of [103], where the deposition fraction of the different channels is again given in dependence on the free electron fraction. Furthermore, a very illustrative comparison between the CK2005 and GSVI2013 approximations mentioned above is displayed in Figure 10 of [103].

Particles	$g_i$	$f_{s,q}$	$\beta_s$	$m_i$ [GeV]	$\beta_i \tilde{M}_i$ [g]
$\gamma$	2	0.060	6.04	0.00	$\infty$
$\nu$	6	0.147	4.53	0.00	$\infty$
$e$	4	0.142	4.53	$5.11 \times 10^{-4}$	$9.3969 \times 10^{16}$
$\mu$	4	0.142	4.53	0.104	$4.5429 \times 10^{14}$
$\tau$	4	0.142	4.53	1.77	$2.7022 \times 10^{13}$
$u$	12	0.142	4.53	$2.2 \times 10^{-3}$	$2.1826 \times 10^{16}$
$d$	12	0.142	4.53	$4.7 \times 10^{-3}$	$1.0217 \times 10^{16}$
$s$	12	0.142	4.53	$9.6 \times 10^{-3}$	$5.0019 \times 10^{14}$
$c$	12	0.142	4.53	1.28	$3.7514 \times 10^{13}$
$b$	12	0.142	4.53	4.18	$1.1488 \times 10^{13}$
$t$	12	0.142	4.53	173.1	$2.7740 \times 10^{11}$
$g$	16	0.060	6.04	0.6	$1.0671 \times 10^{14}$
$\pi^0$	1	0.267	2.66	0.1350	$2.0886 \times 10^{14}$
$\pi^\pm$	2	0.267	2.66	0.1396	$2.0198 \times 10^{14}$
$W$	6	0.060	6.04	80.39	$7.9642 \times 10^{11}$
$Z$	3	0.060	6.04	91.19	$7.0209 \times 10^{11}$
$h$	1	0.267	2.66	125.1	$2.2541 \times 10^{11}$

**Table 2.** Constants for the definition of  $\mathcal{F}(M)$  given in Equation (C.4). Note that several values for  $f_{s,q}$  has been updated compared to Table 1 of [99].

## Others

Other important works on the topic are [38, 97, 98, 159], all with varying levels of refinement and details in the physics. Their adaptation into the code is left for future work.

## C.2 PBH statistical factors

The PBH has a temperature given by the Hawking temperature,

$$T_{\text{BH}} = \frac{1}{8\pi GM} , \quad (\text{C.3})$$

which predominantly guides the particles that can be emitted from the PBH. In Equation (2.61) describing the evolution of the PBH mass, the function  $\mathcal{F}(M)$  [42, 43, 99],

$$\mathcal{F}(M) = \sum_{\text{species } i} g_i f_{s,q} e^{-M/(\beta_s \tilde{M}_i)} , \quad (\text{C.4})$$

represents the effective number of species emitted by the PBH and it is normalized to unity at  $M \gg 10^{17}$  g. At those PBH masses only massless particles (photons and neutrinos) are emitted due to the low PBH temperature. Here  $g_i$  is the numbers of internal degrees of freedom of the particle species  $i$ ,  $f_{s,q}$  is a statistical factor depending on particle spins  $s$  and charges  $q$ ,  $\tilde{M}_i$  is the BH mass that would satisfy  $(8\pi G \tilde{M}_i)^{-1} = m_i$ , and  $\beta_s$  is a spin dependent quantity which accounts for shifts between the peak of the BB distribution (which should be centered at the particle's mass) and the mean PBH temperature given through  $\tilde{M}_i$  [43]. The parameters of this approximation are given in Table 2.

The current form of Equation (C.4) assumes that a BH only emits fundamental particles kinematically available at the BH temperature scale. However, for a temperature below the QCD-confinement scale,  $T_{\text{QCD}} \approx 300$  MeV, quarks and gluons are not emitted singularly, but are instead released in form of pions, which will then subsequently decay into electrons and photons.

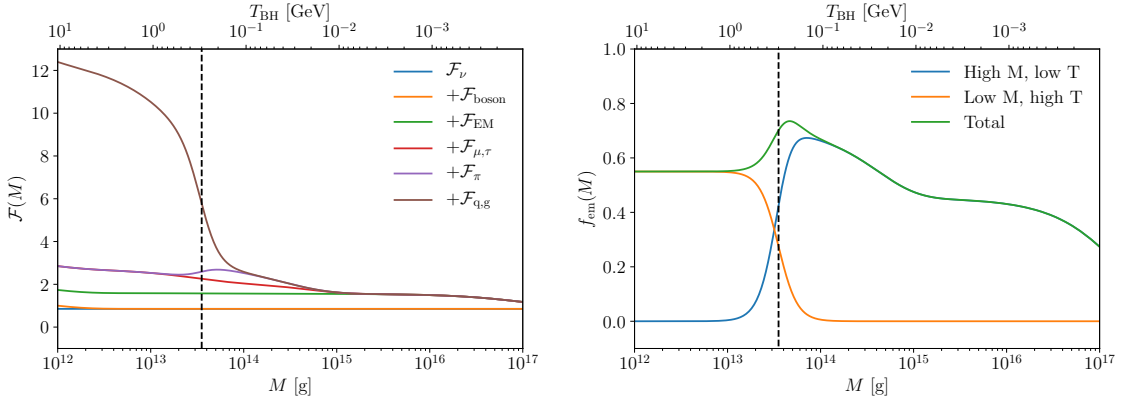


**Figure 10.** **Left panel:** Different contributions to the number of species emitted by the PBH. The quarks-gluon and pions contribution are multiplied with the exponential cut-offs as defined in Equation (C.6). **Right panel:** Fraction of energy going into EM contribution.

On the other hand, above  $T_{\text{QCD}}$  quarks and gluons can be radiated directly. This effect suppresses the quark production for PBHs with masses larger than  $\approx 10^{13.5}$  g, and replaces it with pion emission. Mathematically, this can be accounted for introducing the weighting factor

$$Q_{\text{QCD}}(T_{\text{BH}}) = \left[ 1 + \exp \left( -\frac{\log_{10}(T_{\text{BH}}/T_{\text{QCD}})}{\sigma} \right) \right]^{-1}, \quad (\text{C.5})$$

where  $\sigma$  defines the width of the exponential cut-off and has been set to 0.1. Then Equation (C.4) can be decomposed as

$$\mathcal{F} = \mathcal{F}_{\text{EM}} + \mathcal{F}_{\mu,\tau} + \mathcal{F}_\nu + \mathcal{F}_{\text{q,g}} Q_{\text{QCD}} + \mathcal{F}_\pi (1 - Q_{\text{QCD}}) + \mathcal{F}_{\text{bosons}}, \quad (\text{C.6})$$

where  $\mathcal{F}_{\text{EM}}$  represents the contribution from electrons and photons,  $\mathcal{F}_{\mu,\tau}$  from muons and taus,  $\mathcal{F}_\nu$  from neutrinos,  $\mathcal{F}_{\text{q,g}}$  from quarks and gluons,  $\mathcal{F}_\pi$  from pions, and  $\mathcal{F}_{\text{bosons}}$  from  $W$ ,  $Z$  and  $h$ . The different contributions are displayed in the left panel of Figure 10. The introduction of  $Q_{\text{QCD}}$  also allow us to underline the fact that protons are never directly emitted by the PBH. In fact, below the QCD threshold they are too heavy to be produced, and above the same threshold only the individual quark content is emitted.

As seen in Equation (C.6) and the left panel of Figure 10, it is possible for a PBH to produce particles not interacting electromagnetically, in particular for low PBH masses. These would then not contribute to the total deposited energy. For instance, for PBHs with temperatures above  $T_{\text{QCD}}$ , the contribution from particles like, e.g., quarks and pions, becomes dominant. The number of primary ejection species is described by Equation (C.4), while the secondary abundances can be computed only by taking into account the decay branching ratios of all non-stable particles. In the end, the secondary emission will only consist of protons (only created in secondary processes), electrons, photons and neutrinos.

However, as already mentioned at the beginning of Section 2.4, we are only interested in the electromagnetic contribution, and thus need to additionally isolate and remove the contribution from neutrinos. To accomplish this task, we rely on the calculations carried by [42] (in particular on the results summarized in their Table III). There, the authors show that, for BH temperatures above  $T_{\text{QCD}}$  up to 100 GeV, around 45% of the final emitted power in all secondaries is carried by neutrinos and would therefore not contribute to the deposited energy. This value of 45% is relatively constant, and thus allows us to simply introduce the fraction of energy contributing electromagnetically for relatively low PBH masses as

$$f_{\text{em}}^{\text{low M, high T}} = (1 - 0.45). \quad (\text{C.7})$$

On the other hand, for large PBH masses, the total contribution consists mostly of EM particles and neutrinos. To subtract these, we use the fraction of energy contributing electromagnetically for relatively high PBH masses as

$$f_{\text{em}}^{\text{high M, low T}} = \frac{\mathcal{F} - \mathcal{F}_\nu}{\mathcal{F}} , \quad (\text{C.8})$$

which removes most of the neutrino contribution.

Using the  $Q_{\text{QCD}}$  for a smooth transition from above to below the QCD confinement scale, the Equations (C.8) and (C.7) become

$$f_{\text{em}} = 0.55Q_{\text{QCD}} + (1 - Q_{\text{QCD}}) \frac{\mathcal{F} - \mathcal{F}_\nu}{\mathcal{F}} . \quad (\text{C.9})$$

The shape of the three functions is shown in the right panel of Figure 10.

Note that this approximation neglects the production of neutrinos from the decay of pions and unstable leptons. This approximation is justified considering that – as shown in the left panel of Figure 10 – the evaporation of the PBH into these particles is only allowed below masses of approximately  $10^{15}$  g and is subdominant with respect to  $\mathcal{F}_{\text{EM}}$  and  $\mathcal{F}_\nu$  down to masses in the order of  $10^{14}$  g, where this high-mass approximation for  $f_{\text{em}}$  anyway begins to be suppressed (see the right panel of the same figure). Moreover, only a fraction of the already subdominant contribution from pions and unstable leptons is going to decay into neutrinos, which further lowers the impact of our approximation. A more accurate analysis will only be possible with the help of tools like DARKAGES and DARKHISTORY, which will be subject of future work.

## D Further details on the Green’s function approximation

### D.1 Model independent Green’s functions

For linear differential equations of the type

$$\mathcal{D}y(x) = f(x) , \quad (\text{D.1})$$

with differential operator  $\mathcal{D}$ , one can always find solutions of the type

$$y(x) = \int G(x, x') f(x') dx' , \quad (\text{D.2})$$

where the Green’s function  $G(x, x')$  is a solution to

$$\mathcal{D}G(x, x') = \delta(x - x') . \quad (\text{D.3})$$

When inserting Equation (D.2) into Equation (D.1) and using Equation (D.3), we find

$$\mathcal{D}y(x) = \mathcal{D} \int G(x, x') f(x') dx' = \int \delta(x - x') f(x') dx' = f(x) . \quad (\text{D.4})$$

The advantage of using the Green’s function to solve the system is that the differential equation can be solved for an arbitrary right-hand side  $f(x)$ . Note, that the Green’s function can be found according to Equation (D.3) without knowing any particular  $f(x)$ .

For the case of SDs, this means that the problem can be solved for arbitrary heating histories<sup>18</sup>. All of the information about photon redistribution will be captured within the Green’s function, which can be found independently of the heating history. The heating term can then simply be convolved

---

<sup>18</sup> Assuming that the distortion problem is a linear differential equation, which is valid at first order in the distortions of the PPSD.

with the Green's function to immediately give the total distortion. One would write similarly to Equation (D.2) that

$$\Delta I(x, z) = \int dz' G_{\text{th}}(x, z, z') \frac{dQ(z')/dz'}{\rho_\gamma(z')} . \quad (\text{D.5})$$

where one has to find

$$\mathcal{D}G_{\text{th}}(x, z, z') = \delta(z - z') , \quad (\text{D.6})$$

with the differential operator  $\mathcal{D}$  here representing all interactions, including CS, DC, and BR. Comparing to equation Equation (2.33), we find the representation of the Green's function using the branching ratios and distortion shapes as

$$G_{\text{th}}(x, 0, z') = \mathcal{G}(x)J_g(z') + \mathcal{Y}(x)J_y(z') + \mathcal{M}(x)J_\mu(z') + R(x, z') . \quad (\text{D.7})$$

Solving the full Equation (D.6) thus allows us to find the residual term  $R(x, z)$  as well. Note in conclusion that this approximation is only possible as long as the distortions are very small, as we know to be the case.

## E Further details on the likelihood

### E.1 PIXIE detector sensitivity

According to [72] (and references therein), the PIXIE noise equivalent power (NEP) is defined as

$$\text{NEP}^2 = 2A\Omega T^5 \int \alpha\epsilon f \frac{x^4}{e^x - 1} \left(1 + \frac{\alpha\epsilon f}{e^x - 1}\right) dx , \quad (\text{E.1})$$

where  $A$ ,  $\Omega$  and  $\alpha$  are the detector area, solid angle and absorptivity, respectively, while  $T$  and  $\epsilon$  are the temperature and emissivity of the source. The parameter  $f$  corresponds to the power transmission through the optics. Thus, the noise can be defined as

$$\delta P = \frac{\text{NEP}}{\sqrt{\tau/2}} , \quad (\text{E.2})$$

where  $\tau$  is the integration time and the factor of 2 accounts for the conversion between the frequency and time domains.

The detector noise then reads approximately

$$\delta I_{\text{noise}} = 2 \frac{\delta P}{A\Omega\Delta\nu} \frac{1}{\alpha\epsilon f} , \quad (\text{E.3})$$

where  $\Delta\nu$  is the bandwidth. The presence of the factor 2 is due to the splitting of the sky signal among 4 detectors, which increases the noise by a factor 4, and, at the same time, the averaging of the signal over the 4 detectors lowers the noise by a factor  $1/\sqrt{4}$ . Inserting thus the optical parameters for the deployed calibrator ( $A\Omega = 4 \text{ cm}^2 \text{ sr}$ ,  $\alpha = 0.54$ ,  $f = 0.82$ , and  $\Delta\nu = 15 \text{ GHz}$  as given in Table 1 of [72], and  $\text{NEP} = 2.3 \text{ W/Hz}^{1/2}$ ) into Equation (E.3) and assuming  $\epsilon = 1$ , one obtains

$$\delta I_{\text{noise}} \approx \frac{2.4 \times 10^{-22}}{\sqrt{\tau/1s}} \frac{\text{W}}{\text{m}^2 \text{ Hz sr}} . \quad (\text{E.4})$$

Considering then the time interval of 1 s, one obtains the Stokes parameter  $\delta I_\nu^I$  given in Equation (3.4) of [72]. Additionally, as argued in Appendix B of [72], by multiplying  $\delta I_\nu^I$  by a factor  $\sqrt{2}$  accounting for the presence of polarization, one ends up with the second Stokes parameter  $\delta I_\nu^{QU}$  given in Equation (3.4). Finally, inserting a fiducial value of  $\tau = 2$  years for the total mission duration in Equation (E.4) and considering that the deployed configuration in only employed 25 - 35% of the observing time, one obtains a total sensitivity of  $\delta I_{\text{noise}} \approx 5 \times 10^{-26} \text{ W}/(\text{m}^2 \text{ Hz sr})$ . Note that this value is also the one employed in [76] but neglects penalties due to foreground separation [189]. Higher levels of sensitivity can be achieved by longer integration times or combining multiple copies of the telescope [73].

## References

- [1] PLANCK collaboration, N. Aghanim et al., *Planck 2018 results. VI. Cosmological parameters*, [1807.06209](#).
- [2] P. Ade, J. Aguirre, Z. Ahmed, S. Aiola, A. Ali, D. Alonso et al., *The Simons Observatory: science goals and forecasts*, [JCAP 2019 \(Feb, 2019\) 056](#), [[1808.07445](#)].
- [3] CMB-S4 collaboration, K. N. Abazajian et al., *CMB-S4 Science Book, First Edition*, [1610.02743](#).
- [4] M. H. Abitbol, Z. Ahmed, D. Barron, R. Basu Thakur, A. N. Bender, B. A. Benson et al., *CMB-S4 Technology Book, First Edition*, *arXiv e-prints* (Jun, 2017) arXiv:1706.02464, [[1706.02464](#)].
- [5] K. Abazajian et al., *CMB-S4 Science Case, Reference Design, and Project Plan*, [1907.04473](#).
- [6] T. Matsumura et al., *Mission design of LiteBIRD*, [1311.2847](#).
- [7] A. Suzuki, P. A. R. Ade, Y. Akiba, D. Alonso, K. Arnold, J. Aumont et al., *The LiteBIRD Satellite Mission: Sub-Kelvin Instrument*, [Journal of Low Temperature Physics 193 \(Dec, 2018\) 1048–1056](#), [[1801.06987](#)].
- [8] PLANCK collaboration, R. Adam et al., *Planck 2015 results. X. Diffuse component separation: Foreground maps*, [Astron. Astrophys. 594 \(2016\) A10](#), [[1502.01588](#)].
- [9] BICEP2 collaboration, P. A. R. Ade et al., *Detection of B-Mode Polarization at Degree Angular Scales by BICEP2*, [Phys. Rev. Lett. 112 \(2014\) 241101](#), [[1403.3985](#)].
- [10] POLARBEAR collaboration, P. A. R. Ade et al., *A Measurement of the Cosmic Microwave Background B-Mode Polarization Power Spectrum at Sub-Degree Scales with POLARBEAR*, [Astrophys. J. 794 \(2014\) 171](#), [[1403.2369](#)].
- [11] P. Creminelli, D. L. Lpez Nacir, M. Simonovi, G. Trevisan and M. Zaldarriaga, *Detecting Primordial B-Modes after Planck*, [JCAP 1511 \(2015\) 031](#), [[1502.01983](#)].
- [12] L. Wang and M. Kamionkowski, *Cosmic microwave background bispectrum and inflation*, [Phys. Rev. D 61 \(Feb, 2000\) 063504](#).
- [13] J. R. Fergusson, M. Liguori and E. P. S. Shellard, *General CMB and primordial bispectrum estimation: Mode expansion, map making, and measures of  $F_{NL}$* , [Phys. Rev. D 82 \(Jul, 2010\) 023502](#), [[0912.5516](#)].
- [14] M. Hindmarsh, C. Ringeval and T. Suyama, *CMB temperature trispectrum of cosmic strings*, [Phys. Rev. D 81 \(Mar, 2010\) 063505](#).
- [15] N. Aghanim, S. Majumdar and J. Silk, *Secondary anisotropies of the CMB*, [Reports on Progress in Physics 71 \(may, 2008\) 066902](#).
- [16] U. Seljak, *Gravitational lensing effect on cosmic microwave background anisotropies: A Power spectrum approach*, [Astrophys. J. 463 \(1996\) 1](#), [[astro-ph/9505109](#)].
- [17] M. Zaldarriaga and U. Seljak, *Gravitational lensing effect on cosmic microwave background polarization*, [Phys. Rev. D58 \(1998\) 023003](#), [[astro-ph/9803150](#)].
- [18] A. Challinor and A. Lewis, *Lensed CMB power spectra from all-sky correlation functions*, [Phys. Rev. D71 \(2005\) 103010](#), [[astro-ph/0502425](#)].
- [19] Y. B. Zeldovich and R. Sunyaev, *The interaction of matter and radiation in a hot-model universe*, *Astrophysics and Space Science* **4** (1969) 301–316.
- [20] R. A. Sunyaev and Y. B. Zeldovich, *The interaction of matter and radiation in the hot model of the Universe, II*, *Astrophysics and Space Science* **7** (Apr, 1970) 20–30.
- [21] Y. B. Zeldovich, A. F. Illarionov and R. A. Syunyaev, *Influence of Energy Release on the*

*Radiation Spectrum in the Hot Model of the Universe, Zhurnal Eksperimentalnoi i Teoreticheskoi Fiziki* **62** (1972) 1217.

- [22] A. F. Illarionov and R. A. Sunyaev, *Comptonization, characteristic radiation spectra, and thermal balance of low-density plasma*, *Soviet Astronomy* **18** (Feb., 1975) 413–419.
- [23] L. Danese and G. De Zotti, *Double compton process and the spectrum of the microwave background*, *Astronomy and Astrophysics* **107** (1982) 39–42.
- [24] C. Burigana, L. Danese and G. De Zotti, *Formation and evolution of early distortions of the microwave background spectrum-a numerical study*, *Astronomy and Astrophysics* **246** (1991) 49–58.
- [25] W. Hu and J. Silk, *Thermalization constraints and spectral distortions for massive unstable relic particles*, *Phys. Rev. Lett.* **70** (May, 1993) 2661–2664.
- [26] J. Chluba and R. A. Sunyaev, *The evolution of CMB spectral distortions in the early Universe*, *Mon. Not. Roy. Astron. Soc.* **419** (2012) 1294–1314, [[1109.6552](#)].
- [27] R. A. Sunyaev and J. Chluba, *Signals from the epoch of cosmological recombination - karl schwarzschild award lecture 2008*, *Astronomische Nachrichten* **330** (08, 2009) 657 – 674.
- [28] R. A. Sunyaev and R. Khatri, *Unavoidable CMB Spectral Features and Blackbody Photosphere of Our Universe*, *IJMPD* **22** (June, 2013) 30014, [[1302.6553](#)].
- [29] H. Tashiro, *CMB spectral distortions and energy release in the early universe*, *Prog. of Theo. and Exp. Physics* **2014** (June, 2014) 060000.
- [30] G. De Zotti, M. Negrello, G. Castex, A. Lapi and M. Bonato, *Another look at distortions of the Cosmic Microwave Background spectrum*, *JCAP* **1603** (2016) 047, [[1512.04816](#)].
- [31] J. Chluba, *Which spectral distortions does  $\Lambda$ CDM actually predict?*, *Mon. Not. Roy. Astron. Soc.* **460** (2016) 227–239, [[1603.02496](#)].
- [32] J. C. Hill, N. Battaglia, J. Chluba, S. Ferraro, E. Schaan and D. N. Spergel, *Taking the Universes Temperature with Spectral Distortions of the Cosmic Microwave Background*, *Phys. Rev. Lett.* **115** (2015) 261301, [[1507.01583](#)].
- [33] R. A. Sunyaev and Y. B. Zeldovich, *The Observations of Relic Radiation as a Test of the Nature of X-Ray Radiation from the Clusters of Galaxies*, *Comments on Astrophysics and Space Physics* **4** (Nov, 1972) 173.
- [34] M. Birkinshaw, *The sunyaev-zeldovich effect*, *Physics Reports* **310** (1999) 97 – 195.
- [35] J. E. Carlstrom, G. P. Holder and E. D. Reese, *Cosmology with the sunyaev-zeldovich effect*, *Annual Review of Astronomy and Astrophysics* **40** (2002) 643–680, [<https://doi.org/10.1146/annurev.astro.40.060401.093803>].
- [36] T. Mroczkowski, D. Nagai, K. Basu, J. Chluba, J. Sayers, R. Adam et al., *Astrophysics with the Spatially and Spectrally Resolved Sunyaev-Zeldovich Effects. A Millimetre/Submillimetre Probe of the Warm and Hot Universe*, *Space Science Reviews* **215** (Feb, 2019) 17, [[1811.02310](#)].
- [37] P. McDonald, R. J. Scherrer and T. P. Walker, *Cosmic microwave background constraint on residual annihilations of relic particles*, *Phys. Rev.* **D63** (Jan., 2001) .
- [38] J. Chluba, *Could the Cosmological Recombination Spectrum Help Us Understand Annihilating Dark Matter?*, *Mon. Not. Roy. Astron. Soc.* **402** (2010) 1195, [[0910.3663](#)].
- [39] J. Chluba, *Distinguishing different scenarios of early energy release with spectral distortions of the cosmic microwave background*, *Mon. Not. Roy. Astron. Soc.* **436** (2013) 2232–2243, [[1304.6121](#)].
- [40] Y. Ali-Haïmoud, J. Chluba and M. Kamionkowski, *Constraints on dark matter interactions*

with standard model particles from cosmic microwave background spectral distortions, *Phys. Rev. Lett.* **115** (Aug, 2015) 071304.

- [41] T. R. Slatyer and C.-L. Wu, *Early-universe constraints on dark matter-baryon scattering and their implications for a global 21 cm signal*, *Phys. Rev. D* **98** (Jul, 2018) 023013.
- [42] J. H. MacGibbon and B. Webber, *Quark-and gluon-jet emission from primordial black holes: The instantaneous spectra*, *Physical Review D* **41** (1990) 3052.
- [43] J. H. MacGibbon, *Quark-and gluon-jet emission from primordial black holes. II. The emission over the black-hole lifetime*, *Physical Review D* **44** (1991) 376.
- [44] H. Tashiro and N. Sugiyama, *Constraints on Primordial Black Holes by Distortions of Cosmic Microwave Background*, *Phys. Rev. D* **78** (2008) 023004, [[0801.3172](#)].
- [45] B. J. Carr, K. Kohri, Y. Sendouda and J. Yokoyama, *New cosmological constraints on primordial black holes*, *Phys. Rev. D* **81** (2010) 104019, [[0912.5297](#)].
- [46] T. Nakama, B. Carr and J. Silk, *Limits on primordial black holes from  $\mu$  distortions in cosmic microwave background*, *Phys. Rev. D* **D97** (2018) 043525, [[1710.06945](#)].
- [47] R. A. Sunyaev and Y. B. Zeldovich, *Small scale entropy and adiabatic density perturbations – Antimatter in the Universe*, *ApSS* **9** (Dec., 1970) 368–382.
- [48] R. Daly, *Spectral distortions of the microwave background radiation resulting from the damping of pressure waves*, *The Astrophysical Journal* **371** (1991) 14–28.
- [49] J. D. Barrow and P. Coles, *Primordial density fluctuations and the microwave background spectrum*, *Monthly Notices of the Royal Astronomical Society* **248** (01, 1991) 52–57.
- [50] W. Hu, D. Scott and J. Silk, *Power spectrum constraints from spectral distortions in the cosmic microwave background*, *ApJL* **430** (July, 1994) L5–L8, [[arXiv:astro-ph/9402045](#)].
- [51] J. Chluba, R. Khatri and R. A. Sunyaev, *CMB at  $2 \times 2$  order: The dissipation of primordial acoustic waves and the observable part of the associated energy release*, *Mon. Not. Roy. Astron. Soc.* **425** (2012) 1129–1169, [[1202.0057](#)].
- [52] J. Chluba, A. L. Erickcek and I. Ben-Dayan, *Probing the Inflaton: Small-scale Power Spectrum Constraints from Measurements of the Cosmic Microwave Background Energy Spectrum*, *ApJ* **758** (Oct., 2012) 76, [[1203.2681](#)].
- [53] T. Nakama, J. Chluba and M. Kamionkowski, *Shedding light on the small-scale crisis with CMB spectral distortions*, *Phys. Rev. D* **95** (Jun, 2017) 121302, [[1703.10559](#)].
- [54] J. A. D. Diacoumis and Y. Y. Y. Wong, *Using CMB spectral distortions to distinguish between dark matter solutions to the small-scale crisis*, *JCAP* **1709** (2017) 011, [[1707.07050](#)].
- [55] PLANCK collaboration, N. Aghanim et al., *Planck 2015 results. XXII. A map of the thermal Sunyaev-Zeldovich effect*, *Astron. Astrophys.* **594** (2016) A22, [[1502.01596](#)].
- [56] C. Pitrou, F. Bernardeau and J.-P. Uzan, *The  $y$ -sky: diffuse spectral distortions of the cosmic microwave background*, *JCAP* **1007** (2010) 019, [[0912.3655](#)].
- [57] S. Renaux-Petel, C. Fidler, C. Pitrou and G. W. Pettinari, *Spectral distortions in the cosmic microwave background polarization*, *JCAP* **1403** (2014) 033, [[1312.4448](#)].
- [58] C. Pitrou and A. Stebbins, *Parameterization of temperature and spectral distortions in future CMB experiments*, *Gen. Rel. Grav.* **46** (2014) 1806, [[1402.0968](#)].
- [59] A. Ota, *Statistical anisotropy in CMB spectral distortions*, *Phys. Lett. B* **790** (2019) 243–247, [[1810.03928](#)].
- [60] J. Chluba, A. Kogut, S. P. Patil, M. H. Abitbol, N. Aghanim, Y. Ali-Haïmoud et al., *Spectral Distortions of the CMB as a Probe of Inflation, Recombination, Structure Formation and Particle Physics*, *Bulletin of the AAS* **51** (May, 2019) 184, [[1903.04218](#)].

[61] A. F. Illarionov and R. A. Sunyaev, *Comptonization, the background-radiation spectrum, and the thermal history of the universe*, *Soviet Astronomy* **18** (June, 1975) 691–699.

[62] R. Khatri and R. A. Sunyaev, *Beyond  $y$  and  $\mu$ : the shape of the CMB spectral distortions in the intermediate epoch*,  $1.5 \times 10^4 < z < 2 \times 10^5$ , *JCAP* **9** (Sept., 2012) 16, [[1207.6654](#)].

[63] J. Chluba, *Green’s function of the cosmological thermalization problem*, *Mon. Not. Roy. Astron. Soc.* **434** (2013) 352, [[1304.6120](#)].

[64] J. Chluba, *Green’s function of the cosmological thermalization problem – II. Effect of photon injection and constraints*, *Mon. Not. Roy. Astron. Soc.* **454** (2015) 4182–4196, [[1506.06582](#)].

[65] Y. Ali-Haïmoud, *Effective conductance method for the primordial recombination spectrum*, *Phys. Rev. D* **87** (Jan., 2013) 023526, [[1211.4031](#)].

[66] J. Chluba and Y. Ali-Haimoud, *CosmoSpec: Fast and detailed computation of the cosmological recombination radiation from hydrogen and helium*, *Mon. Not. Roy. Astron. Soc.* **456** (2016) 3494–3508, [[1510.03877](#)].

[67] J. Chluba, D. Nagai, S. Sazonov and K. Nelson, *A fast and accurate method for computing the Sunyaev-Zeldovich signal of hot galaxy clusters*, *Mon. Not. Roy. Astron. Soc.* **426** (2012) 510, [[1205.5778](#)].

[68] J. Chluba, E. R. Switzer, D. Nagai and K. Nelson, *Sunyaev-Zeldovich signal processing and temperature-velocity moment method for individual clusters*, *Mon. Not. Roy. Astron. Soc.* **430** (2013) 3054, [[1211.3206](#)].

[69] J. C. Mather, E. S. Cheng, D. A. Cottingham, R. E. Eplee, Jr., D. J. Fixsen, T. Hewagama et al., *Measurement of the cosmic microwave background spectrum by the COBE FIRAS instrument*, *ApJ* **420** (Jan., 1994) 439–444.

[70] D. J. Fixsen, E. S. Cheng, J. M. Gales, J. C. Mather, R. A. Shafer and E. L. Wright, *The Cosmic Microwave Background spectrum from the full COBE FIRAS data set*, *Astrophys. J.* **473** (1996) 576, [[astro-ph/9605054](#)].

[71] D. J. Fixsen, *The Temperature of the Cosmic Microwave Background*, *Astrophys. J.* **707** (Dec, 2009) 916–920, [[0911.1955](#)].

[72] A. Kogut, D. J. Fixsen, D. T. Chuss, J. Dotson, E. Dwek, M. Halpern et al., *The Primordial Inflation Explorer (PIXIE): a nulling polarimeter for cosmic microwave background observations*, *Journal of Cosmology and Astro-Particle Physics* **2011** (Jul, 2011) 025, [[1105.2044](#)].

[73] A. Kogut, M. H. Abitbol, J. Chluba, J. Delabrouille, D. Fixsen, J. C. Hill et al., *CMB Spectral Distortions: Status and Prospects*, *arXiv e-prints* (Jul, 2019) arXiv:1907.13195, [[1907.13195](#)].

[74] J. Chluba, M. H. Abitbol, N. Aghanim, Y. Ali-Haimoud, M. Alvarez, K. Basu et al., *New Horizons in Cosmology with Spectral Distortions of the Cosmic Microwave Background*, *arXiv e-prints* (Sep, 2019) arXiv:1909.01593, [[1909.01593](#)].

[75] D. Blas, J. Lesgourgues and T. Tram, *The Cosmic Linear Anisotropy Solving System (CLASS) II: Approximation schemes*, *JCAP* **1107** (2011) 034, [[1104.2933](#)].

[76] J. Chluba and D. Jeong, *Teasing bits of information out of the CMB energy spectrum*, *Mon. Not. Roy. Astron. Soc.* **438** (2014) 2065–2082, [[1306.5751](#)].

[77] J. Chluba, *Refined approximations for the distortion visibility function and  $\mu$ -type spectral distortions*, May, 2014. 10.1093/mnras/stu414.

[78] J. Chluba, J. Hamann and S. P. Patil, *Features and new physical scales in primordial observables: Theory and observation*, *IJMP D* **24** (June, 2015) 1530023, [[1505.01834](#)].

[79] J. Chluba, *Future Steps in Cosmology using Spectral Distortions of the Cosmic Microwave Background*, *arXiv e-prints* (Jun, 2018) arXiv:1806.02915, [[1806.02915](#)].

[80] A. Kompaneets, *The establishment of thermal equilibrium between quanta and electrons*, *Soviet Physics JETP* **4** (1957) 730–737.

[81] A. Lightman, *Double compton emission in radiation dominated thermal plasmas*, *The Astrophysical Journal* **244** (1981) 392–405.

[82] J. Chluba, *Spectral distortions of the cosmic microwave background*. PhD thesis, lmu, 2005.

[83] J. Hamann and Y. Y. Y. Wong, *Effects of CMB temperature uncertainties on cosmological parameter estimation*, *JCAP* **0803** (2008) 025, [[0709.4423](#)].

[84] J. Chluba, *Tests of the CMB temperatureredshift relation, CMB spectral distortions and why adiabatic photon production is hard*, *Mon. Not. Roy. Astron. Soc.* **443** (2014) 1881–1888, [[1405.1277](#)].

[85] PLANCK collaboration, P. A. R. Ade et al., *Planck 2015 results. XIII. Cosmological parameters*, *Astron. Astrophys.* **594** (2016) A13, [[1502.01589](#)].

[86] G. Steigman, *Primordial Nucleosynthesis in the Precision Cosmology Era*, *Annual Review of Nuclear and Particle Science* **57** (Nov., 2007) 463–491, [[0712.1100](#)].

[87] Schöneberg, Nils and Lesgourgues, Julien and Hooper, Deanna C., *The BAO+BBN take on the Hubble tension*, [1907.11594](#).

[88] M. Pospelov, J. Pradler, J. T. Ruderman and A. Urbano, *Room for New Physics in the Rayleigh-Jeans Tail of the Cosmic Microwave Background*, Tech. Rep. 3, 2018. 10.1103/PhysRevLett.121.031103.

[89] Y. E. Lyubarsky and R. A. Sunyaev, *The spectral features in the microwave background spectrum due to energy release in the early universe*, *A&A* **123** (July, 1983) 171–183.

[90] J. Chluba and R. A. Sunyaev, *Pre-recombinational energy release and narrow features in the CMB spectrum*, *Astron. Astrophys.* **501** (2009) 29–47, [[0803.3584](#)].

[91] T. A. Enßlin and C. R. Kaiser, *Comptonization of the cosmic microwave background by relativistic plasma*, *A&A* **360** (Aug., 2000) 417–430, [[arXiv:astro-ph/0001429](#)].

[92] T. R. Slatyer, *Indirect dark matter signatures in the cosmic dark ages. II. Ionization, heating, and photon production from arbitrary energy injections*, *Phys. Rev.* **D93** (Jan., 2016) 023521, [[1506.03812](#)].

[93] S. K. Acharya and R. Khatri, *Rich structure of nonthermal relativistic CMB spectral distortions from high energy particle cascades at redshifts  $z \lesssim 2 \times 10^5$* , *Phys. Rev. D* **99** (Feb, 2019) 043520, [[1808.02897](#)].

[94] S. K. Acharya and R. Khatri, *New CMB spectral distortion constraints on decaying dark matter with full evolution of electromagnetic cascades before recombination*, *Phys. Rev.* **D99** (2019) 123510, [[1903.04503](#)].

[95] S. K. Acharya and R. Khatri, *CMB anisotropy and BBN constraints on pre-recombination decay of dark matter to visible particles*, [1910.06272](#).

[96] W. Hu and J. Silk, *Thermalization and spectral distortions of the cosmic background radiation*, *Phys. Rev.* **D48** (1993) 485–502.

[97] T. R. Slatyer, N. Padmanabhan and D. P. Finkbeiner, *CMB Constraints on WIMP Annihilation: Energy Absorption During the Recombination Epoch*, *Phys. Rev.* **D80** (2009) 043526, [[0906.1197](#)].

[98] T. R. Slatyer, *Energy Injection And Absorption In The Cosmic Dark Ages*, *Phys. Rev.* **D87** (2013) 123513, [[1211.0283](#)].

[99] Stöcker, P. and Krämer, M. and Lesgourgues, J. and Poulin, V., *Exotic energy injection with ExoCLASS: Application to the Higgs portal model and evaporating black holes*, *JCAP* **1803**

(2018) 018, [1801.01871].

- [100] H. Liu, G. W. Ridgway and T. R. Slatyer, *DarkHistory: A code package for calculating modified cosmic ionization and thermal histories with dark matter and other exotic energy injections*, [1904.09296](#).
- [101] X.-L. Chen and M. Kamionkowski, *Particle decays during the cosmic dark ages*, *Phys. Rev. D* **70** (2004) 043502, [[astro-ph/0310473](#)].
- [102] N. Padmanabhan and D. P. Finkbeiner, *Detecting dark matter annihilation with CMB polarization: Signatures and experimental prospects*, *Physical Review D* **72** (2005) 023508.
- [103] S. Galli, T. R. Slatyer, M. Valdes and F. Iocco, *Systematic Uncertainties In Constraining Dark Matter Annihilation From The Cosmic Microwave Background*, *Phys. Rev. D* **88** (2013) 063502, [[1306.0563](#)].
- [104] M. Roos, *Introduction to Cosmology*. Wiley, 2015.
- [105] D. Scott and A. Moss, *Matter temperature during cosmological recombination*, *MNRAS* **397** (Jul, 2009) 445–446, [[0902.3438](#)].
- [106] S. Seager, D. D. Sasselov and D. Scott, *How exactly did the universe become neutral?*, *The Astrophysical Journal Supplement Series* **128** (2000) 407.
- [107] J. Silk, *Cosmic black-body radiation and galaxy formation*, *The Astrophysical Journal* **151** (1968) 459.
- [108] R. Khatri, R. A. Sunyaev and J. Chluba, *Mixing of blackbodies: entropy production and dissipation of sound waves in the early Universe*, *Astron. Astrophys.* **543** (2012) A136, [[1205.2871](#)].
- [109] C.-P. Ma and E. Bertschinger, *Cosmological perturbation theory in the synchronous and conformal Newtonian gauges*, *Astrophys. J.* **455** (1995) 7–25, [[astro-ph/9506072](#)].
- [110] J. Chluba, L. Dai, D. Grin, M. A. Amin and M. Kamionkowski, *Spectral distortions from the dissipation of tensor perturbations*, *MNRAS* **446** (Jan., 2015) 2871–2886.
- [111] C. Pitrou, *Radiative transport of relativistic species in cosmology*, [1902.09456](#).
- [112] J. Chluba and D. Grin, *CMB spectral distortions from small-scale isocurvature fluctuations*, *Mon. Not. Roy. Astron. Soc.* **434** (2013) 1619–1635, [[1304.4596](#)].
- [113] W. T. Hu, *Wandering in the Background: A CMB Explorer*. PhD thesis, UC, Berkeley, 1995. [astro-ph/9508126](#).
- [114] A. Ota, T. Takahashi, H. Tashiro and M. Yamaguchi, *CMB  $\mu$  distortion from primordial gravitational waves*, *JCAP* **10** (Oct., 2014) 29, [[1406.0451](#)].
- [115] PLANCK collaboration, Y. Akrami et al., *Planck 2018 results. X. Constraints on inflation*, [1807.06211](#).
- [116] P. Peebles, *Recombination of the primeval plasma*, *The Astrophysical Journal* **153** (1968) 1.
- [117] V. K. Dubrovich, *Hydrogen recombination lines of cosmological origin*, *Soviet Astronomy Letters* **1** (Oct., 1975) 196.
- [118] S. C. O. Glover, J. Chluba, S. R. Furlanetto, J. R. Pritchard and D. W. Savin, *Chapter Three - Atomic, Molecular, and Optical Physics in the Early Universe: From Recombination to Reionization*, *Advances in Atomic Molecular and Optical Physics* **63** (Aug., 2014) 135–270.
- [119] J. Chluba and R. A. Sunyaev, *Free-bound emission from cosmological hydrogen recombination*, *Astron. Astrophys.* **458** (2006) L29–L32, [[astro-ph/0608120](#)].
- [120] J. A. Rubino-Martin, J. Chluba and R. A. Sunyaev, *Lines in the cosmic microwave background spectrum from the epoch of cosmological helium recombination*, *Astron. Astrophys.*

485 (2008) 377, [0711.0594].

- [121] J. Chluba and R. A. Sunyaev, *Cosmological recombination: feedback of helium photons and its effect on the recombination spectrum*, *MNRAS* **402** (Feb., 2010) 1221–1248, [0909.2378].
- [122] J. Chluba, J. Fung and E. R. Switzer, *Radiative transfer effects during primordial helium recombination*, *MNRAS* **423** (July, 2012) 3227–3242, [1110.0247].
- [123] J. Chluba and R. A. Sunyaev, *Is there need and another way to measure the Cosmic Microwave Background temperature more accurately?*, *Astron. Astrophys.* (2007) , [0707.0188].
- [124] J. Chluba and R. M. Thomas, *Towards a complete treatment of the cosmological recombination problem*, *Mon. Not. Roy. Astron. Soc.* **412** (2011) 748, [1010.3631].
- [125] V. Desjacques, J. Chluba, J. Silk, F. de Bernardis and O. Doré, *Detecting the cosmological recombination signal from space*, *MNRAS* **451** (Aug., 2015) 4460–4470.
- [126] M. Sathyana Rayana Rao, R. Subrahmanyam, N. Udaya Shankar and J. Chluba, *On the Detection of Spectral Ripples from the Recombination Epoch*, *ApJ* **810** (Sept., 2015) 3.
- [127] Y. B. Zeldovich, A. F. Illarionov and R. A. Sunyaev, *The Effect of Energy Release on the Emission Spectrum in a Hot Universe*, *Soviet Journal of Experimental and Theoretical Physics* **35** (Jan, 1972) 643.
- [128] J. Chluba and R. A. Sunyaev, *Superposition of blackbodies and the dipole anisotropy: A Possibility to calibrate CMB experiments*, *Astron. Astrophys.* **424** (2003) 389–408, [astro-ph/0404067].
- [129] A. Stebbins, *CMB Spectral Distortions from the Scattering of Temperature Anisotropies*, *arXiv e-prints* (Mar, 2007) astro-ph/0703541, [astro-ph/0703541].
- [130] J. Chluba, *Fast and accurate computation of the aberration kernel for the cosmic microwave background sky*, *MNRAS* **415** (Aug., 2011) 3227–3236.
- [131] WMAP collaboration, G. Hinshaw et al., *Five-Year Wilkinson Microwave Anisotropy Probe (WMAP) Observations: Data Processing, Sky Maps, and Basic Results*, *Astrophys. J. Suppl.* **180** (2009) 225–245, [0803.0732].
- [132] S. Y. Sazonov and R. A. Sunyaev, *Cosmic Microwave Background Radiation in the Direction of a Moving Cluster of Galaxies with Hot Gas: Relativistic Corrections*, *ApJ* **508** (Nov., 1998) 1–5.
- [133] A. Challinor and A. Lasenby, *Relativistic Corrections to the Sunyaev-Zeldovich Effect*, *ApJ* **499** (May, 1998) , [arXiv:astro-ph/9711161].
- [134] N. Itoh, Y. Kohyama and S. Nozawa, *Relativistic Corrections to the Sunyaev-Zeldovich Effect for Clusters of Galaxies*, *ApJ* **502** (July, 1998) , [arXiv:astro-ph/9712289].
- [135] A. Stebbins, *The cmbr spectrum*, *arXiv preprint astro-ph/9705178* (1997) .
- [136] J. P. Ostriker and E. T. Vishniac, *Generation of Microwave Background Fluctuations from Nonlinear Perturbations at the ERA of Galaxy Formation*, *ApJL* **306** (Jul, 1986) L51.
- [137] Y. Rephaeli and O. Lahav, *Peculiar Cluster Velocities from Measurements of the Kinematic Sunyaev-Zeldovich Effect*, *ApJ* **372** (May, 1991) 21.
- [138] S. Nozawa, N. Itoh, Y. Suda and Y. Ohhata, *An improved formula for the relativistic corrections to the kinematical Sunyaev-Zeldovich effect for clusters of galaxies*, *Nuovo Cim.* **B121** (2006) 487–500, [astro-ph/0507466].
- [139] E. Komatsu and T. Kitayama, *Sunyaev-Zeldovich Fluctuations from Spatial Correlations between Clusters of Galaxies*, *ApJL* **526** (Nov., 1999) L1–L4, [astro-ph/9908087].
- [140] M. Remazeilles, B. Bolliet, A. Rotti and J. Chluba, *Can we neglect relativistic temperature corrections in the Planck thermal SZ analysis?*, *MNRAS* **483** (Mar, 2019) 3459–3464,

[1809.09666].

- [141] Z. Staniszewski et al., *Galaxy clusters discovered with a Sunyaev-Zel'dovich effect survey*, *Astrophys. J.* **701** (2009) 32–41, [[0810.1578](#)].
- [142] M. Hasselfield et al., *The Atacama Cosmology Telescope: Sunyaev-Zel'dovich selected galaxyclusters at 148 GHz from three seasons of data*, *JCAP* **1307** (2013) 008, [[1301.0816](#)].
- [143] C. L. Reichardt, B. Stalder, L. E. Bleem, T. E. Montroy, K. A. Aird, K. Andersson et al., *Galaxy Clusters Discovered via the Sunyaev-Zel'dovich Effect in the First 720 Square Degrees of the South Pole Telescope Survey*, *Astrophys. J.* **763** (Feb, 2013) 127, [[1203.5775](#)].
- [144] K. T. Story, C. L. Reichardt, Z. Hou, R. Keisler, K. A. Aird, B. A. Benson et al., *A Measurement of the Cosmic Microwave Background Damping Tail from the 2500-Square-Degree SPT-SZ Survey*, *Astrophys. J.* **779** (Dec, 2013) 86, [[1210.7231](#)].
- [145] M. B. Gralla et al., *A measurement of the millimetre emission and the Sunyaev-Zel'dovich effect associated with low-frequency radio sources*, *Mon. Not. Roy. Astron. Soc.* **445** (2014) 460–478, [[1310.8281](#)].
- [146] PLANCK collaboration, P. A. R. Ade et al., *Planck 2013 results. XX. Cosmology from Sunyaev-Zeldovich cluster counts*, *Astron. Astrophys.* **571** (2014) A20, [[1303.5080](#)].
- [147] SPT collaboration, L. E. Bleem et al., *Galaxy Clusters Discovered via the Sunyaev-Zel'dovich effect in the 2500-square-degree SPT-SZ survey*, *Astrophys. J. Suppl.* **216** (2015) 27, [[1409.0850](#)].
- [148] L. Titarchuk and G. Lipunova, *The cosmic microwave background spectral modification due to thermal Comptonization in galaxy clusters. Analytical consideration*, [1906.07060](#).
- [149] R. A. Sunyaev and L. G. Titarchuk, *Comptonization of X-rays in plasma clouds - Typical radiation spectra*, *Astronomy and Astrophysics* **86** (June, 1980) 121–138.
- [150] L. Pozdnyakov, I. Sobol and R. A. Syunyaev, *Comptonization and the shaping of X-ray source spectra-Monte Carlo calculations*, *Astrophysics and Space Physics Reviews* **2** (1983) 189–331.
- [151] L. Titarchuk and Y. Lyubarskij, *Power-law spectra as a result of comptonization of the soft radiation in a plasma cloud*, *The Astrophysical Journal* **450** (1995) 876.
- [152] J. Chluba, L. Dai and M. Kamionkowski, *Multiple scattering Sunyaev-Zeldovich signal I: lowest order effect*, *Mon. Not. Roy. Astron. Soc.* **437** (2014) 67–76, [[1308.5969](#)].
- [153] J. Chluba and L. Dai, *Multiple scattering Sunyaev-Zeldovich signal II: relativistic effects*, *Mon. Not. Roy. Astron. Soc.* **438** (2014) 1324–1334, [[1309.3274](#)].
- [154] S. Galli, F. Iocco, G. Bertone and A. Melchiorri, *CMB constraints on Dark Matter models with large annihilation cross-section*, *Phys. Rev. D* **80** (2009) 023505, [[0905.0003](#)].
- [155] V. Poulin, P. D. Serpico and J. Lesgourgues, *Dark Matter annihilations in halos and high-redshift sources of reionization of the universe*, *JCAP* **1512** (2015) 041, [[1508.01370](#)].
- [156] P. McDonald, R. J. Scherrer and T. P. Walker, *Cosmic microwave background constraint on residual annihilations of relic particles*, *Phys. Rev. D* **63** (Dec, 2000) 023001.
- [157] C. M. Ho and R. J. Scherrer, *Sterile neutrinos and light dark matter save each other*, *Phys. Rev. D* **87** (Mar, 2013) 065016.
- [158] J. Chen and Y.-F. Zhou, *The 130 GeV gamma-ray line and sommerfeld enhancements*, *Journal of Cosmology and Astroparticle Physics* **2013** (apr, 2013) 017–017.
- [159] G. Huetsi, A. Hektor and M. Raidal, *Constraints on leptonically annihilating Dark Matter from reionization and extragalactic gamma background*, *Astron. Astrophys.* **505** (2009) 999–1005, [[0906.4550](#)].
- [160] V. Poulin, J. Lesgourgues and P. D. Serpico, *Cosmological constraints on exotic injection of*

*electromagnetic energy*, *JCAP* **1703** (2017) 043, [[1610.10051](#)].

[161] M. Kawasaki, K. Kohri and T. Moroi, *Big-Bang nucleosynthesis and hadronic decay of long-lived massive particles*, *Phys. Rev.* **D71** (2005) 083502, [[astro-ph/0408426](#)].

[162] K. Jedamzik, *Bounds on long-lived charged massive particles from Big Bang nucleosynthesis*, *JCAP* **0803** (2008) 008, [[0710.5153](#)].

[163] B. Carr, F. Kuhnel and M. Sandstad, *Primordial Black Holes as Dark Matter*, *Phys. Rev.* **D94** (2016) 083504, [[1607.06077](#)].

[164] A. S. Josan, A. M. Green and K. A. Malik, *Generalized constraints on the curvature perturbation from primordial black holes*, *Phys. Rev. D* **79** (May, 2009) 103520.

[165] P. H. Frampton, M. Kawasaki, F. Takahashi and T. T. Yanagida, *Primordial Black Holes as All Dark Matter*, *JCAP* **1004** (2010) 023, [[1001.2308](#)].

[166] S. Young and C. T. Byrnes, *Primordial black holes in non-Gaussian regimes*, *JCAP* **1308** (2013) 052, [[1307.4995](#)].

[167] E. V. Bugaev and P. A. Klimai, *Primordial black hole constraints for curvaton models with predicted large non-Gaussianity*, *Int. J. Mod. Phys. D* **22** (2013) 1350034, [[1303.3146](#)].

[168] B. C. Lacki and J. F. Beacom, *Primordial Black Holes as Dark Matter: Almost All or Almost Nothing*, *Astrophys. J.* **720** (2010) L67–L71, [[1003.3466](#)].

[169] K. Kohri, T. Nakama and T. Suyama, *Testing scenarios of primordial black holes being the seeds of supermassive black holes by ultracompact minihalos and cmb  $\mu$  distortions*, *Phys. Rev. D* **90** (Oct, 2014) 083514.

[170] Yu. N. Eroshenko, *Dark matter density spikes around primordial black holes*, *Astron. Lett.* **42** (2016) 347–356, [[1607.00612](#)].

[171] S. M. Boucenna, F. Khnel, T. Ohlsson and L. Visinelli, *Novel constraints on mixed dark-matter scenarios of primordial black holes and WIMPs*, *Journal of Cosmology and Astroparticle Physics* **2018** (jul, 2018) 003–003.

[172] J. Adamek, C. T. Byrnes, M. Gosenca and S. Hotchkiss, *WIMPs and stellar-mass primordial black holes are incompatible*, *Phys. Rev. D* **100** (2019) 023506, [[1901.08528](#)].

[173] G. Bertone, A. M. Coogan, D. Gaggero, B. J. Kavanagh and C. Weniger, *Primordial Black Holes as Silver Bullets for New Physics at the Weak Scale*, [1905.01238](#).

[174] S. W. Hawking, *Black hole explosions*, *Nature* **248** (1974) 30–31.

[175] M. Ricotti, J. P. Ostriker and K. J. Mack, *Effect of Primordial Black Holes on the Cosmic Microwave Background and Cosmological Parameter Estimates*, *Astrophys. J.* **680** (2008) 829, [[0709.0524](#)].

[176] Y. Ali-Hamoud and M. Kamionkowski, *Cosmic microwave background limits on accreting primordial black holes*, *Phys. Rev. D* **95** (2017) 043534, [[1612.05644](#)].

[177] V. Poulin, P. D. Serpico, F. Calore, S. Clesse and K. Kohri, *CMB bounds on disk-accreting massive primordial black holes*, *Phys. Rev. D* **96** (2017) 083524, [[1707.04206](#)].

[178] G. Giesen, J. Lesgourgues, B. Audren and Y. Ali-Hamoud, *CMB photons shedding light on dark matter*, *JCAP* **1212** (2012) 008, [[1209.0247](#)].

[179] B. Audren, J. Lesgourgues, K. Benabed and S. Prunet, *Conservative Constraints on Early Cosmology: an illustration of the Monte Python cosmological parameter inference code*, *JCAP* **1302** (2013) 001, [[1210.7183](#)].

[180] T. Brinckmann and J. Lesgourgues, *MontePython 3: boosted MCMC sampler and other features*, [1804.07261](#).

[181] W. Y. Wong, A. Moss and D. Scott, *How well do we understand cosmological recombination?*, *Mon. Not. Roy. Astron. Soc.* **386** (2008) 1023–1028, [[0711.1357](#)].

[182] Y. Ali-Haimoud and C. M. Hirata, *HyRec: A fast and highly accurate primordial hydrogen and helium recombination code*, *Phys. Rev.* **D83** (2011) 043513, [[1011.3758](#)].

[183] J. Chluba, D. Paoletti, F. Finelli and J.-A. Rubio-Martn, *Effect of primordial magnetic fields on the ionization history*, *Mon. Not. Roy. Astron. Soc.* **451** (2015) 2244–2250, [[1503.04827](#)].

[184] I. M. Oldengott, D. Boriero and D. J. Schwarz, *Reionization and dark matter decay*, *JCAP* **1608** (2016) 054, [[1605.03928](#)].

[185] L. F. Shampine and M. W. Reichelt, *The matlab ode suite*, *SIAM journal on scientific computing* **18** (1997) 1–22.

[186] J. Chluba, “Green’s function method.”   
<http://www.jb.man.ac.uk/~jchlu/Science/CosmoTherm/Greens.html>.

[187] L. Perotto, J. Lesgourgues, S. Hannestad, H. Tu and Y. Y. Y. Wong, *Probing cosmological parameters with the CMB: Forecasts from full Monte Carlo simulations*, *JCAP* **0610** (2006) 013, [[astro-ph/0606227](#)].

[188] PRISM collaboration, P. Andr et al., *PRISM (Polarized Radiation Imaging and Spectroscopy Mission): An Extended White Paper*, *JCAP* **1402** (2014) 006, [[1310.1554](#)].

[189] M. H. Abitbol, J. Chluba, J. C. Hill and B. R. Johnson, *Prospects for Measuring Cosmic Microwave Background Spectral Distortions in the Presence of Foregrounds*, *Mon. Not. Roy. Astron. Soc.* **471** (2017) 1126–1140, [[1705.01534](#)].

[190] T. Brinckmann, D. C. Hooper, M. Archidiacono, J. Lesgourgues and T. Sprenger, *The promising future of a robust cosmological neutrino mass measurement*, *JCAP* **1901** (2019) 059, [[1808.05955](#)].

[191] A. Kosowsky and M. S. Turner, *CBR anisotropy and the running of the scalar spectral index*, *Phys. Rev. D* **52** (Aug, 1995) R1739–R1743, [[astro-ph/9504071](#)].

[192] E. Silverstein and A. Westphal, *Monodromy in the CMB: Gravity waves and string inflation*, *Phys. Rev. D* **78** (Nov, 2008) 106003, [[0803.3085](#)].

[193] M. Czerny, T. Kobayashi and F. Takahashi, *Running spectral index from large-field inflation with modulations revisited*, *Physics Letters B* **735** (Jul, 2014) 176–180, [[1403.4589](#)].

[194] Q. E. Minor and M. Kaplinghat, *Inflation that runs naturally: Gravitational waves and suppression of power at large and small scales*, *Phys. Rev. D* **91** (Mar, 2015) 063504, [[1411.0689](#)].

[195] J. Chluba, *Science with CMB spectral distortions*, in *Proceedings, 49th Rencontres de Moriond on Cosmology: La Thuile, Italy, March 15-22, 2014*, pp. 327–334, 2014. [1405.6938](#).

[196] C. T. Byrnes, P. S. Cole and S. P. Patil, *Steepest growth of the power spectrum and primordial black holes*, *JCAP* **1906** (2019) 028, [[1811.11158](#)].

[197] R. Khatri and R. A. Sunyaev, *Forecasts for CMB  $\mu$  and  $i$ -type spectral distortion constraints on the primordial power spectrum on scales  $8jk;10^4 \text{ Mpc}^{-1}$  with the future Pixie-like experiments*, *JCAP* **6** (June, 2013) 26, [[1303.7212](#)].

[198] G. Cabass, A. Melchiorri and E. Pajer,  *$\mu$  distortions or running: A guaranteed discovery from CMB spectrometry*, *Phys. Rev. D* **93** (Apr., 2016) 083515, [[1602.05578](#)].

[199] G. Cabass, E. Di Valentino, A. Melchiorri, E. Pajer and J. Silk, *Constraints on the running of the running of the scalar tilt from CMB anisotropies and spectral distortions*, *Phys. Rev. D* **94** (July, 2016) 023523.

[200] V. Poulin and P. D. Serpico, *Nonuniversal BBN bounds on electromagnetically decaying*

particles, *Phys. Rev.* **D91** (2015) 103007, [[1503.04852](#)].

- [201] H. Poulter, Y. Ali-Hamoud, J. Hamann, M. White and A. G. Williams, *CMB constraints on ultra-light primordial black holes with extended mass distributions*, [1907.06485](#).
- [202] R. Khatri and R. A. Sunyaev, *Creation of the CMB spectrum: precise analytic solutions for the blackbody photosphere*, *JCAP* **2012** (Jun, 2012) 038, [[1203.2601](#)].
- [203] J. M. Shull and M. E. van Steenberg, *X-ray secondary heating and ionization in quasar emission-line clouds*, *Astrophys. J.* **298** (Nov., 1985) 268–274.
- [204] M. Valdes and A. Ferrara, *The Energy Cascade from Warm Dark Matter Decays*, *Mon. Not. Roy. Astron. Soc.* **387** (2008) 8, [[0803.0370](#)].